T2R2 東京科学大学 リサーチリポジトリ
Science Tokyo Research Repository

論文 / 著書情報
Article / Book Information

題目(和文)	電子-フォノン複合系における量子デコヒーレンスの超高速ダイナミクス
Title(English)	Ultrafast dynamics of quantum decoherence in an electron-phonon composite system
著者(和文)	髙木一旗
Author(English)	Itsuki Takagi
出典(和文)	学位:博士(理学), 学位授与機関:東京工業大学, 報告番号:甲第12653号, 授与年月日:2024年3月26日, 学位の種別:課程博士, 審査員:中村 一隆,笹川 崇男,川路 均,松田 晃史,三宮 工
Citation(English)	Degree:Doctor (Science), Conferring organization: Tokyo Institute of Technology, Report number:甲第12653号, Conferred date:2024/3/26, Degree Type:Course doctor, Examiner:,,,,
学位種別(和文)	博士論文
Type(English)	Doctoral Thesis

Powered by T2R2 (Science Tokyo Research Repository)

Doctoral thesis

Ultrafast dynamics of quantum decoherence in an electron-phonon composite system

Itsuki Takagi

Department of Materials Science and Engineering
Tokyo Institute of Technology, Japan

Supervisor Kazutaka Nakamura

March 2024

Abstract

Quantum coherence is a unique property of quantum mechanics that enables the superposition of quantum states and plays a pivotal role in advancing quantum technologies, notably quantum computers. Quantum coherence has been extensively studied in various fields, including atomic, molecular, biological, and solid-state materials. In solids, quantum coherence rapidly disappears due to interactions with the enormous quantum degrees of freedom. In particular, band-to-band electronic coherence is a remarkably rapid phenomenon occurring within attoseconds to a few femtoseconds, leading to a limited understanding of decoherence times and mechanisms.

In this thesis, I focus on the ultrafast dynamics of quantum decoherence in an electron–phonon composite system and aim to reveal electronic decoherence times and phenomena. We experimentally and theoretically investigate the ultrafast dynamics of electronic and phononic coherence. We formulate a quantum mechanical model of the electron–phonon composite system and study the influence of polarization and excitation intensity of ultrashort optical pulses, initial phonon state, and dissipation on quantum coherence.

Furthermore, we measure the electronic coherence in n-type gallium arsenide single crystal as a test sample, using the attosecond precision relative phase-locked double femtosecond pulse excitation method. By varying the degree of decoherence with temperature, we observe the temperature dependence of the quantum interference fringes. These experimentally observed interference fringes are in agreement with theoretical calcu-

lations, allowing the quantitative determination of electronic decoherence times at different temperatures: 27.8 fs at 10 K, 23.0 fs at 90 K, and 12.9 fs at 290 K. We discuss the decoherence phenomenon of electronic states associated with the phonon system. The electronic decoherence phenomenon is well explained by major scattering between photo-excited and surrounding carriers in the conduction bands.

List of Published Articles

Parts of this thesis have been published in the following journal articles:

[1] **Itsuki Takagi**, Yosuke Kayanuma, and Kazutaka G. Nakamura, "Theory for coherent control of longitudinal optical phonons in GaAs using polarized optical pulses with relative phase locking", Physical Review B **104**, 134301 (2021).

[2] **Itsuki Takagi**, Yosuke Kayanuma, and Kazutaka G. Nakamura, "Ultrafast quantum path interferometry to determine the electronic decoherence time of the electron–phonon coupled system in n-type gallium arsenide", Physical Review B **107**, 184305 (2023).

[3] **Itsuki Takagi**, and Kazutaka G. Nakamura, "The influence of initial phonon states on the generation of coherent optical phonons", Solid State Communications **360**, 115053 (2023).

[4] **Itsuki Takagi**, Yosuke Kayanuma, and Kazutaka G. Nakamura, "Stimulated Raman blockade in coherent phonon generation", Solid State Communications **373-374**, 115316 (2023).

Acknowledgments

This research was conducted at the Department of Materials Science and Engineering, School of Materials and Chemical Technology, Tokyo Institute of Technology, under the auspices of the Nakamura Laboratory. I am grateful to all those who contributed to the completion of this thesis.

I would like to express my sincere gratitude to my supervisor, Prof. Kazutaka Nakamura, for his invaluable guidance and support. He also provided advice and assistance in all aspects of my research, including discussions, presentations, and writing scientific papers. His unwavering support enabled me to complete this thesis.

I would like to express my gratitude to Prof. Takao Sasagawa, Prof. Hitoshi Kawaji, Prof. Akifumi Matsuda, and Prof. Takumi Sannomiya for their willingness to serve as examiners for this thesis.

I sincerely thank Prof. Yosuke Kayanuma for his guidance and assistance in the theoretical aspects, presentations, and writing of the scientific papers. I also sincerely thank Prof. Fujio Minami for his invaluable help in adjusting the experimental femtosecond laser pulse apparatus.

I would also like to thank my undergraduate lab supervisor, Prof. Hirohisa Taguchi, who inspired me to pursue a Master's and Ph.D student. Under his guidance, I gained valuable experience as an undergraduate student, including writing a scientific paper and participating in domestic/international conferences.

I would also like to thank the members of the Nakamura Laboratory for their kindness and support. Mr. Yuya Furusho, Mr. Hiroyuki Tanabe, Mr. Tsukasa Maruhashi, Ms. Ryoko Yagi, and Mr. Masaki Suda provided

invaluable support on various aspects of the research work. I am grateful to Dr. Tetsuya Kimata for his insightful and fruitful guidance on the research. I am also grateful to my junior colleagues for their encouragement and warm hospitality; Mr. Taichi Kato, Mr. Ryota Takai, Mr. Shogo Oyama, Mr. Yuma Konno, Mr. Mitsunari Hirose, Mr. Shin'ichi Kakuta, Mr. Itsuki Kasai, Mr. Taichi Nishimura, Ms. Yuka Yamaya, and Mr. Yuto Tokuyama. I am very happy and fortunate to be a research group member.

I would also like to thank my friends who have encouraged me, especially Mr. Masahiro Noda, Mr. Kiwamu Suzuki, and Mr. Hiroki Kishi, among others. Their continued association provided a good break during the research activities.

I am grateful to the Japan Society for the Promotion of Science (JSPS). I firmly believe that this support has enabled me to conduct my research in a relaxed manner.

Finally, I am indescribably grateful to my family for their unwavering support and encouragement throughout my Ph.D. life.

Itsuki Takagi

Contents

Chapter 1
Introduction

In this chapter, I review several studies on the quantum coherence of electron-phonon composite systems in solids and present the main issues and aims of this study.

1.1 Background

1.1.1 Quantum coherence

Quantum properties, phenomena, and related ultrafast dynamics have recently attracted worldwide attention, as evidenced by the Nobel Prize in Physics for quantum entanglement (2022) [1] and attosecond pulses (2023) [2]. Quantum coherence is also a unique property of quantum mechanics that allows the superposition of quantum states. It is a fundamental property of quantum physics and plays a key role in many quantum technologies, such as quantum computing, communication, and sensing. The identification of coherent quantum behavior and properties has emerged as a critical issue for the realization of these techniques and has been observed, discussed and published in the past in many quantum systems [3–12].

Quantum coherence has been extensively studied in solid state, atomic, molecular, and biological systems [13–19]. It persists for longer lifetimes in isolated systems such as atoms and molecules [11, 20, 21]. However, there are numerous quantum degrees of freedom in solids. Any system other than the quantum system of interest (or observation) acts as an

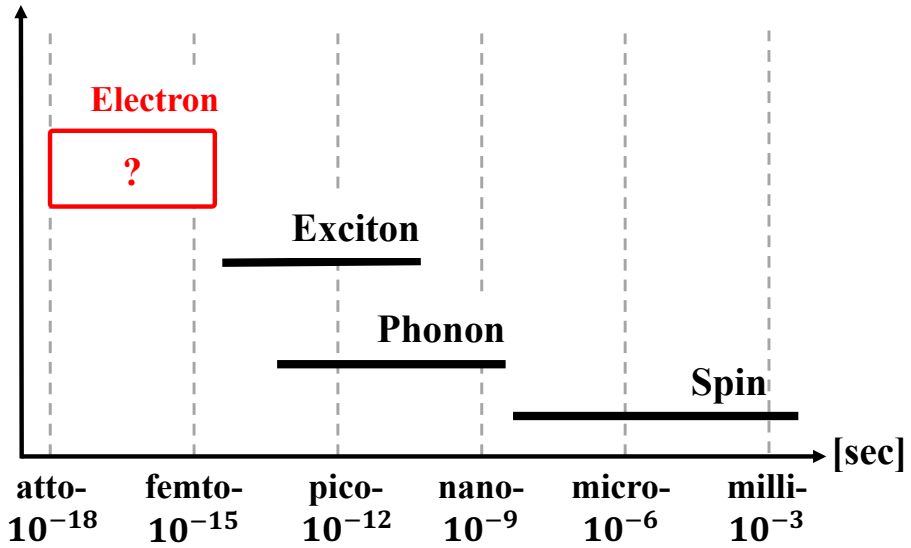

Figure 1.1: A diagram of typical quantum systems and their coherence retention times in solids.

enormous number of environmental systems. Thus, quantum coherence rapidly disappears in macroscopic systems, especially in condensed matter or solids, due to interactions with the environment.

There are many quanta of interest in quantum coherence studies in solids. The coherence of quantum systems such as electron spin [9, 10, 22–24], phonons [3, 4, 25–28], and excitons [5, 29–33] have been reported in many studies, whereas the coherence of (band-to-band) free electrons has been reported in extremely few studies [34–36]. The spin coherence is in the nanosecond to millisecond range. In addition, the coherences of phonons and excitons are in the hundreds of femtoseconds to picoseconds range, whereas the coherence of free electrons is a few tens of femtoseconds at best and disappears very quickly.

Therefore, the precise duration of electronic coherence persistence and the mechanisms governing its collapse in condensed matter systems remains to be definitively determined. The investigation of the persistence and dissipation of quantum coherence is essential not only for the next generation of quantum technologies but also as a fundamental problem in

quantum physics, which seeks to understand the quantum-classical boundary, including the transition between the quantum and classical realms.

1.1.2 Electron–phonon composite system

The physical properties of semiconductors have been studied using a multifaceted approach that includes electrical, optical, and structural studies. Gallium arsenide (GaAs) is a highly representative semiconductor material in diverse applications ranging from high-speed and high-frequency devices to electronic and optical technologies [37–39]. In addition, GaAs serves as an archetypal material for the study of quasiparticle interactions because of its direct bandgap, which is closely aligned with the energy of a typical femtosecond laser (~ 800 nm).

Quasiparticle interactions in solid-state materials play an important role in various physical phenomena, such as non-equilibrium dynamics and electron transport. Electron–phonon interactions also play an important role in condensed matter physics, influencing key parameters such as electron mobility and superconductivity [40–45]. The electron–phonon composite system is one of the prominent coherence systems, and enables the observation of phonon coherence (referred to as coherent phonons) and electronic coherence.

i) Phonon coherence

Upon irradiation with ultrashort optical pulses, characterized by a temporal width shorter than the oscillation period of the phonons, the optical phonons induce in-phase oscillations. These phonons induced by femtosecond optical pulses are called coherent optical phonons (or vibrational wave packets) [46]. Coherent phonons can be generated by irradiating a single optical pulse, and the decoherence time of single-mode phonons can

be evaluated by curve-fit analysis using a damped harmonic oscillator [46, 47].

Coherent phonons are interpreted as the coherence of phonon states [48]. The generation mechanisms of coherent phonons can be classified into two types according to the electronic transition: impulsive stimulated Raman scattering (ISRS) [46, 49–52] and impulsive absorption (IA), the latter often denoted as displacive excitation of coherent phonons (DECP) [46, 53–55]. The theoretical initial phases of phonon oscillations by each mechanism are different, with ISRS indicating a sine-like oscillation [46, 48–50, 52] and IA indicating a cosine-like oscillation [46, 48, 53, 55]. In the transparent region, the main mechanism generates coherent optical phonons is the ISRS mechanism [46, 49, 50]. In the opaque region, both mechanisms can contribute to generating coherent phonons. It is difficult to investigate the contribution of each mechanism in the opaque region, because it depends on several factors, such as the optical pulse width and the excitation energy.

ii) Electronic coherence

Interference techniques, in particular coherent spectroscopy and four-wave mixing (FWM), are well-known methods for assessing the coherence of electronic systems. FWM experiments to investigate the electronic coherence time in GaAs have been reported by the research groups of Shank [34, 35, 56] and Wegener [36, 57–59]. They evaluated the decay time of band-to-band excited electrons using the photon-echo technique and sub-10 femtosecond pulses at room temperature. For instance, Wegener et al. reported that they used optical pulses with a pulse width of 11 fs and a time resolution of about 5 fs to evaluate the decay time of electrons that dissipate in a few-femtoseconds [36]. Subsequently, Cundiff reviews the free electron relaxation time and briefly describes the pulse bandwidth and

time resolution concerns of several FWM experiments [32].

These coherent spectroscopy and photon-echo techniques are extremely useful for evaluating the phase relaxation time. However, further details of electronic coherence, such as the temporal evolution of oscillation behavior, cannot be investigated because of measurement techniques, time resolution, and other factors. Therefore, it is imperative to develop measurement techniques that achieve attosecond precision with short pulse bandwidths to probe the detailed behavior of electronic coherence.

1.1.3 Quantum path interferometry

Our research group has introduced quantum path interferometry for these problems, especially for the time resolution on the order of attoseconds with short pulse bandwidth and for the determination of the generation mechanism of coherent phonons. This approach is a relative phase-locked double-pulse excitation technique with attosecond precision. In this scheme, we observe the coherence of the electronic state via the coherence of the phonon states (i.e., coherent phonons), which differs from the conventional FWM method. By precisely controlling the relative phase of the double pulses, it is possible to read the quantum interference information with attosecond precision. Therefore, it is possible to directly observe the time evolution of the decoherence behavior, i.e., the disappearance of the interference of the electronic coherence.

The great advantage of this technique is that it allows attosecond time control, which is a time region shorter than the femtosecond pulse width. It also allows us to measure the electronic coherence (oscillation) behavior with attosecond precision, which could not be observed with FWM. Moreover, the obtained quantum interference is a powerful information source, revealing the quantum path taken by the observed state within the quantum

system [60, 61]. This is useful for investigating coherent phonon mechanisms.

Previously, our efforts led to the observation of quantum coherence in GaAs using quantum path interferometry [60, 62]. Notably, the electronic interference exhibited a longer time duration than the optical interference of the double excitation pulses. This observation implies the persistence of electronic coherence in the material, thus confirming our success in detecting its presence [60]. However, the observed shape of quantum interference in GaAs exhibits specific features such as collapse and revival behavior. It cannot be evaluated by simple curve fitting, as in the case of coherent phonons. Therefore, the major problem remained to evaluate the electronic decoherence time from the interference shape.

The elucidation of the electronic decoherence time, a phenomenon in the ultrafast regime ranging from attoseconds to femtoseconds, will significantly enhance our understanding of decoherence phenomena in macroscopic systems, especially those involving solid-state materials.

1.2 Objective

This doctoral thesis focuses on the ultrafast dynamics of quantum coherence in an electron-phonon composite system and aims to reveal electronic decoherence times and decoherence phenomena.

The two main objectives of this thesis are as follows.

I. To quantitatively determine the electronic decoherence time at which dissipation occurs in the ultrafast regime of attoseconds to few-femtoseconds.
II. To reveal the decoherence mechanism of the electronic coherence phenomena.

The crux of this thesis lies in determining how to evaluate the electronic coherence time by elucidating the coherence properties of electron-phonon systems and their dependence on quantum path interference. These issues are complex. We investigate several problems to establish a quantitative method for determining the electronic decoherence time, e.g., the influence of the polarization and excitation intensity of the ultrashort optical pulse and the initial phonon state.

1.3 Outline

This thesis consists of six chapters.

Chapter 1 describes the research background and the objective of this thesis.

Chapter 2 describes the newly developed theoretical framework elucidating the coherent control of an electron-phonon composite system facilitated by the optical pulse's polarization effects. The microscopic foundation of the electron-phonon interaction within the Raman scattering process is integrated into coherent phonon theory by including two terms corresponding to the Raman tensor. The theoretical results obtained under different polarization conditions are discussed.

Chapter 3 describes the quantitative evaluation of the quantum decoherence time of an electron-phonon composite system in GaAs as a test sample using ultrafast quantum path interferometry. Theoretical studies of coherent phonons and coherent control revealed the profound influence of the relative polarization angle of the double pump pulses and the electronic decoherence time on the quantum interference shapes. In particular, the quantum interference shape obtained at a relative polarization angle of $\pi/4$ for the pump pulses is expected to allow easy visualization of shape variations due to changes in the electronic decoherence time. Therefore, in

this chapter, the intricate relationship between the quantum path interference shape and decoherence in terms of the relative polarization angle of the double pump pulse is studied in detail.

Chapter 4 presents a theoretical evaluation of coherent phonon generation in an arbitrary initial state. The purpose of this study is to explore whether temperature and other factors affect the results of quantum path interference. We define a mixed state as the system's initial state, considering the phonon distribution determined by the thermal equilibrium distribution, and investigate the coherent phonon generation process under finite temperatures.

Chapter 5 presents a theoretical evaluation of the influence of the optical intensity of the excitation pulse. The quantum path interference experiments involve the optical interference of double pulses. Therefore, it is essential to examine how pulse intensity affects quantum interference and coherent phonon generation. In addition, we attempt to reformulate our previous theoretical models within the framework of open quantum theory, with a further focus on the decoherence phenomenon.

Finally, Chapter 6 presents the conclusions of this thesis. We discuss the remaining questions based on the research in the previous chapters. The overall findings of the research for this thesis's objectives are presented.

References

[1] NobelPrize.org, *The Nobel Prize in Physics 2022*, (2022)

[2] NobelPrize.org, *The Nobel Prize in Physics 2023*, (2023)

[3] G. C. Cho, W. Kütt, and H. Kurz, Phys. Rev. Lett. **65**, 764 (1990).

[4] A. V. Kuznetsov and C. J. Stanton, Phys. Rev. B **51**, 7555 (1995).

[5] E. O. Göbel, K. Leo, T. C. Damen, J. Shah, S. Schmitt-Rink, W. Schäfer, J. F. Müller, and K. Köhler, Phys. Rev. Lett. **64**, 1801 (1990).

[6] D. F. Walls and G. J. Milburn, Phys. Rev. A **31**, 2403 (1985).

[7] G. B. Serapiglia, E. Paspalakis, C. Sirtori, K. L. Vodopyanov, and C. C. Phillips, Phys. Rev. Lett. **84**, 1019 (2000).

[8] M. Dantus and V. V. Lozovoy, Chem. Rev. **104**, 1813 (2004).

[9] J. Du, X. Rong, N. Zhao, Y. Wang, J. Yang, and R. B. Liu, Nature **461**, 1265 (2009).

[10] N. Bar-Gill, L. M. Pham, A. Jarmola, D. Budker, and R. L. Walsworth, Nat. Commun. **4**, 1743 (2013).

[11] I. Bloch, Nature **453**, 1016 (2008).

[12] A. Streltsov, G. Adesso, and M. B. Plenio, Rev. Mod. Phys. **89**, 041003 (2017).

[13] E. Romero, R. Augulis, V. I. Novoderezhkin, M. Ferretti, J. Thieme, D. Zigmantas, and R. van Grondelle, Nat. Phys. **10**, 676 (2014).

[14] J.-L. Brédas, E. H. Sargent, and G. D. Scholes, Nat. Mater. **16**, 35 (2017).

[15] D. Madrid-Úsuga, C. E. Susa, and J. H. Reina, Phys. Chem. Chem. Phys. **21**, 12640 (2019).

[16] G. D. Scholes, G. R. Fleming, L. X. Chen, A. Aspuru-Guzik, A. Buchleitner, D. F. Coker, G. S. Engel, R. van Grondelle, A. Ishizaki, D. M. Jonas, J. S. Lundeen, J. K. McCusker, S. Mukamel, J. P. Ogilvie, A. Olaya-Castro, M. A. Ratner, F. C. Spano, K. B. Whaley, and X. Zhu, Nature **543**, 647 (2017).

[17] J. W. Park, Z. Z. Yan, H. Loh, S. A. Will, and M. W. Zwierlein, Science **357**, 372 (2017).

[18] I. Khmelinskii and V. I. Makarov, Chem. Phys. **532**, 110671 (2020).

[19] S. Welinski, P. J. T. Woodburn, N. Lauk, R. L. Cone, C. Simon, P. Goldner, and C. W. Thiel, Phys. Rev. Lett. **122**, 247401 (2019).

[20] J. M. Zadrozny, J. Niklas, O. G. Poluektov, and D. E. Freedman, ACS Cent. Sci. **1**, 488 (2015).

[21] K. Bader, D. Dengler, S. Lenz, B. Endeward, S.-D. Jiang, P. Neugebauer, and J. van Slageren, Nat. Commun. **5**, 5304 (2014).

[22] J. R. Petta, A. C. Johnson, J. M. Taylor, E. A. Laird, A. Yacoby, M. D. Lukin, C. M. Marcus, M. P. Hanson, and A. C. Gossard, Science **309**, 2180 (2005).

[23] F. H. L. Koppens, K. C. Nowack, and L. M. K. Vandersypen, Phys. Rev. Lett. **100**, 236802 (2008).

[24] D. D. Awschalom, L. C. Bassett, A. S. Dzurak, E. L. Hu, and J. R. Petta, Science **339**, 1174 (2013).

[25] F. Vallée and F. Bogani, Phys. Rev. B **43**, 12049 (1991).

[26] T. Dekorsy, G. C. Cho, and H. Kurz, "Coherent phonons in condensed media", in *Light scattering in solids viii: fullerenes, semiconductor surfaces, coherent phonons*, edited by M. Cardona and G. Güntherodt (Springer Berlin Heidelberg, Berlin, Heidelberg, 2000), pp. 169–209.

[27] R. Merlin, Solid State Commun **102**, 207 (1997).

[28] M. Kozák, F. Trojánek, P. Galář, M. Varga, A. Kromka, and P. Malý, Opt. Express **21**, 31521 (2013).

[29] L. Schultheis, J. Kuhl, A. Honold, and C. W. Tu, Phys. Rev. Lett. **57**, 1635 (1986).

[30] K. Leo, T. C. Damen, J. Shah, E. O. Göbel, and K. Köhler, Appl. Phys. Lett. **57**, 19 (1990).

[31] K. Leo, E. O. Göbel, T. C. Damen, J. Shah, S. Schmitt-Rink, W. Schäfer, J. F. Müller, K. Köhler, and P. Ganser, Phys. Rev. B **44**, 5726 (1991).

[32] S. T. Cundiff, Opt. Express **16**, 4639 (2008).

[33] K. Mizoguchi, O. Kojima, T. Furuichi, M. Nakayama, K. Akahane, N. Yamamoto, and N. Ohtani, Phys. Rev. B **69**, 233302 (2004).

[34] P. C. Becker, H. L. Fragnito, C. H. B. Cruz, R. L. Fork, J. E. Cunningham, J. E. Henry, and C. V. Shank, Phys. Rev. Lett. **61**, 1647 (1988).

[35] M. T. Portella, J.-Y. Bigot, R. W. Schoenlein, J. E. Cunningham, and C. V. Shank, Appl. Phys. Lett. **60**, 2123 (1992).

[36] W. A. Hügel, M. F. Heinrich, M. Wegener, Q. T. Vu, L. Bányai, and H. Haug, Phys. Rev. Lett. **83**, 3313 (1999).

[37] J. V. Dilorenzo and D. D. Khandelwal, *GaAs FET principles and technology* (1982).

[38] S. M. Sze and M. K. Lee, *Semiconductor devices: physics and technology*, Semiconductor Devices, Physics and Technology (Wiley, 2012).

[39] S. M. Sze, Y. Li, and K. K. Ng, *Physics of semiconductor devices* (Wiley, 2021).

[40] J. M. Ziman, *Electrons and phonons: the theory of transport phenomena in solids*, International series of monographs on physics (Clarendon Press, 1960).

[41] G. D. Mahan, *Many-particle physics*, Physics of Solids and Liquids (Springer US, 2013).

[42] P. Y. Yu and M. Cardona, *Fundamentals of semiconductors: physics and materials properties*, 3rd ed. (Springer Berlin, 2001).

[43] R. D. Mattuck, *A guide to feynman diagrams in the many-body problem: second edition*, Dover Books on Physics (Dover Publications, 2012).

[44] J. Bardeen, L. N. Cooper, and J. R. Schrieffer, Phys. Rev. **108**, 1175 (1957).

[45] A. Lanzara, P. V. Bogdanov, X. J. Zhou, S. A. Kellar, D. L. Feng, E. D. Lu, T. Yoshida, H. Eisaki, A. Fujimori, K. Kishio, J.-I. Shimoyama, T. Noda, S. Uchida, Z. Hussain, and Z.-X. Shen, Nature **412**, 510 (2001).

[46] G. Lanzani, G. Cerullo, and S. De Silvestri, *Coherent vibrational dynamics*, Practical Spectroscopy (CRC Press, 2007).

[47] M. Hase and M. Kitajima, J. Phys. Condens. Matter **22**, 073201 (2010).

[48] K. G. Nakamura, Y. Shikano, and Y. Kayanuma, Phys. Rev. B **92**, 144304 (2015).

[49] Y.-X. Yan and K. A. Nelson, J. Chem. Phys. **87**, 6240 (1987).

[50] Y.-X. Yan and K. A. Nelson, J. Chem. Phys. **87**, 6257 (1987).

[51] L. Dhar, J. A. Rogers, and K. A. Nelson, Chem. Rev. **94**, 157 (1994).

[52] T. E. Stevens, J. Kuhl, and R. Merlin, Phys. Rev. B **65**, 144304 (2002).

[53] T. K. Cheng, J. Vidal, H. J. Zeiger, G. Dresselhaus, M. S. Dresselhaus, and E. P. Ippen, Appl. Phys. Lett. **59**, 1923 (1991).

[54] A. V. Kuznetsov and C. J. Stanton, Phys. Rev. Lett. **73**, 3243 (1994).

[55] H. J. Zeiger, J. Vidal, T. K. Cheng, E. P. Ippen, G. Dresselhaus, and M. S. Dresselhaus, Phys. Rev. B **45**, 768 (1992).

[56] C. Shank and B. Zakharchenya, *Spectroscopy of nonequilibrium electrons and phonons*, Modern Problems in Condensed Matter Sciences (Elsevier, Amsterdam, 1992).

[57] M. Wegener, J. Lumin. **87-89**, 20 (2000).

[58] H. Haug and A. P. Jauho, *Quantum kinetics in transport and optics of semiconductors*, Springer Series in Solid-State Sciences (Springer Berlin Heidelberg, 2008).

[59] W. Schäfer and M. Wegener, *Semiconductor optics and transport phenomena*, Advanced Texts in Physics (Springer, 2002).

[60] K. G. Nakamura, K. Yokota, Y. Okuda, R. Kase, T. Kitashima, Y. Mishima, Y. Shikano, and Y. Kayanuma, Phys. Rev. B **99**, 180301 (R) (2019).

[61] Y. Furusho, R. Yagi, M. Suda, T. Maruhashi, I. Takagi, Y. Kayanuma, F. Minami, and K. G. Nakamura, Solid State Commun **360**, 115056 (2023).

[62] H. Matsumoto, T. Kitashima, T. Maruhashi, I. Takagi, Y. Kayanuma, and K. G. Nakamura, Solid State Commun **327**, 114215 (2021).

Chapter 2
Theory for coherent control of longitudinal optical phonons in GaAs using polarized optical pulses with relative phase locking

In this chapter, we derive a theoretical model for the coherent control of longitudinal optical phonons in GaAs as test sample, by double-pulse excitation using a simplified band model and the allowed and forbidden Raman scattering. The influence of the polarization of the double pulse and the electronic decoherence time on the quantum interference fringe is discussed. This work is published in Physical Review B [1].

2.1 Introduction

Coherent control is the technique of manipulating quantum states in materials using optical pulses [2–4]. This is widely used to manipulate electronic, vibrational, and rotational states of atoms and molecules [5–9], and excitons, spins, and phonons in the solid state [10–16]. Optical phonons can be coherently excited and monitored using ultrashort optical pulses via transient reflectivity or transmissivity using a pump–probe technique [17–22]. In this technique, the amplitude of the phonons is controlled using a train of optical pulses or a pulse-shaping technique [23–27] via constructive or destructive interference between the induced phonons. Furthermore, by applying a relative phase of the optical pulses to solid materials, not only phonon interference but also electronic interference can be observed via a quantum-path interference [28].

In our previous works, we investigated the coherent control of longitudinal optical (LO) phonons in an n-type GaAs single crystal with a (001) surface using relative phase-locked femtosecond double pulses under parallel and perpendicular polarization [28, 29]. Using parallel-polarized pump pulses, we observed fine interference fringes of electronic coherence with fast oscillations as well as phonon interference for a longer time than for the optical interference between pump pulses [28]. The generation paths were distinguished from the interference fringe patterns. By contrast, for perpendicularly polarized pump pulses, only phonon interference was observed [29].

Coherent phonons in GaAs have been widely studied [18, 20, 24, 30, 31]. There are two processes that contribute to the generation of LO phonons in GaAs in the opaque regime. The main process for generating LO phonons in GaAs (especially for n-doped and p-doped samples) is considered to be the transient depletion field screening [30], which is a type of space charge field-induced process. The initial field distribution is suppressed by the opposite drift of the optically induced electrons and holes, and the accompanying depolarization field acts as the nonlinear driving term for the coherent phonons [18]. A stimulated Raman process is another generation mechanism which is different from the transient depletion field screening process and is also discussed to contribute for non-doped GaAs [31].

The stimulated Raman process also includes two interactions. One is a short-range interaction, which is induced by the deformation-potential interaction, and the other is a long-range interaction, such as the Fröhlich interaction [30, 31]. The creation and annihilation of phonons by light scattering via the short-range interaction is expressed with dipole-allowed components in a Raman tensor. An ultrashort optical pulse can induce impulsive stimulated Raman scattering (ISRS) to generate optical phonons. Furthermore, the long-range interaction can be treated as the dipole-

forbidden components in the Raman tensor [31, 32]. The dipole-allowed Raman tensor for LO phonon scattering in a zinc-blende crystal with the (001) surface is an off-diagonal tensor. Then, the electronic polarization rotates with an angle of $\pi/2$ during phonon generation. This suggests an interesting possibility that the electronic states interact with light pulses differently depending on the polarization direction. It would be possible to detect this Raman-induced rotation of the electronic polarization through the ultrafast interferometric pump-probe measurements with polarization- and delay-controlled double pulses. On the other hand, for the transient depletion field screening process, the field is perpendicular to the surface, and an isotropic polarization dependence for generation of the LO phonons is reported [18, 30].

Theoretical calculations for the generation and detection of coherent phonons have been performed using several models, in which the lattice oscillation is treated classically or quantum mechanically [17, 19, 20, 33–39]. Recently, we developed a quantum mechanical model with classical optical fields for the coherent control of the amplitude of optical phonons induced by two pulses and applied this model to GaAs and diamond crystals [28, 29, 40]. In these previous works, the effects of polarization correlation between the two pump pulses were not studied in sufficient detail. Thus, in the present work, we focus our attention on the problem of the polarization effects of relative-phase-locked double pulses. As a first step in this direction, we study theoretically the quantum mechanical aspects of the interference fringes for the polarization- and delay-controlled double-pulse excitation of coherent phonons. For the sake of concreteness, we study the coherent control of LO phonons in a GaAs crystal with the (001) surface, using a simplified band model and a total Raman tensor that includes the allowed and forbidden components. The allowed and forbidden Raman components coexist in GaAs, and their relative contribution can be

controlled by the doping rate. This makes GaAs an interesting test material to evaluate the effects of quantum-path interference. We calculate the amplitude of the LO phonons and quantitatively discuss the phonon and electronic interference behaviors depending on the polarization angles of the pump pulses.

2.2 Model

2.2.1 Hamiltonian

We consider the generation of the LO phonons, which propagate along the z axis in a GaAs crystal with a (001) surface upon irradiation of two pump pulses that also propagate along the z axis; we identify the [001] axis as the z axis. The electronic states are assumed to be the electronic ground state ($|g\rangle$) and the two-excited-state bands ($|e_x, k\rangle$, and $|e_y, k\rangle$), which are polarized along the x and y axes, respectively, with the wave number k and are degenerate in energy. We set the x axis along the [100] crystal axis and the y axis along the [010] axis. We use a single-electron approximation in the model. The Hamiltonian of the electron-phonon composite states is given by

$$H = H_{\mathrm{e}} + H_{\mathrm{L}} + H_{\mathrm{eL}}, \tag{2.1}$$

$$H_{\mathrm{e}} = \varepsilon_g |g\rangle \langle g| + \sum_k \varepsilon_k \left(|e_x, k\rangle \langle e_x, k| + |e_y, k\rangle \langle e_y, k| \right), \tag{2.2}$$

$$H_{\mathrm{L}} = \hbar\omega b^\dagger b, \tag{2.3}$$

$$\begin{aligned} H_{\mathrm{eL}} = {} & \alpha\hbar\omega \sum_k \left(|e_x, k\rangle \langle e_y, k| + |e_y, k\rangle \langle e_x, k| \right) \left(b^\dagger + b \right) \\ & + \beta\hbar\omega \sum_k \left(|e_x, k\rangle \langle e_x, k| + |e_y, k\rangle \langle e_y, k| \right) \left(b^\dagger + b \right), \end{aligned} \tag{2.4}$$

where ω is the phonon frequency, and ε_g, ε_e are the energies of the ground and excited levels, respectively [28]. The operators $b^\dagger$, b are the creation and annihilation operators for LO phonons at the $\Gamma-$ point, respectively. In the electron-phonon interaction Hamiltonian H_{eL}, the terms proportional to α and β represent the respective interactions for allowed and forbidden Raman scattering, and the total Raman tensor for LO phonons in GaAs is given by

$$R = \begin{pmatrix} R_\beta & R_\alpha & 0 \\ R_\alpha & R_\beta & 0 \\ 0 & 0 & R_\beta \end{pmatrix}, \tag{2.5}$$

where R_α and R_β are the polarization rates of the allowed and forbidden Raman scattering, respectively [32, 41]. When the light propagates along the z axis, only the $xx, yy, xy,$ and yx planes are relevant. The allowed Raman scattering is due to the deformation-potential interaction, and the forbidden Raman scattering is due to the intraband Fröhlich and Franz-Keldysh [31]. The values α and β are proportional to R_α and R_β, respectively.

Within the rotating-wave approximation, the interaction Hamiltonian between light and electrons is expressed by

$$\begin{aligned} H_I = E_1(t) \sum_k \left(\mu_k \left| e_1, k \right\rangle \left\langle g \right| e^{-i\Omega_0 t} + H.c. \right) \\ + E_2(t) \sum_k \left(\mu_k \left| e_2, k \right\rangle \left\langle g \right| e^{-i\Omega_0 (t - t_{12})} + H.c. \right), \end{aligned} \tag{2.6}$$

in which μ_k is the transition dipole moment, Ω_0 is the frequency of the pump pulse, and t_{12} is the delay between pump pulses 1 and 2. Here, H.c. represents the Hermitian conjugate terms, and $|e_1, k\rangle$ and $|e_2, k\rangle$ represent the excited state determined by the polarization of pump pulses 1 and 2,

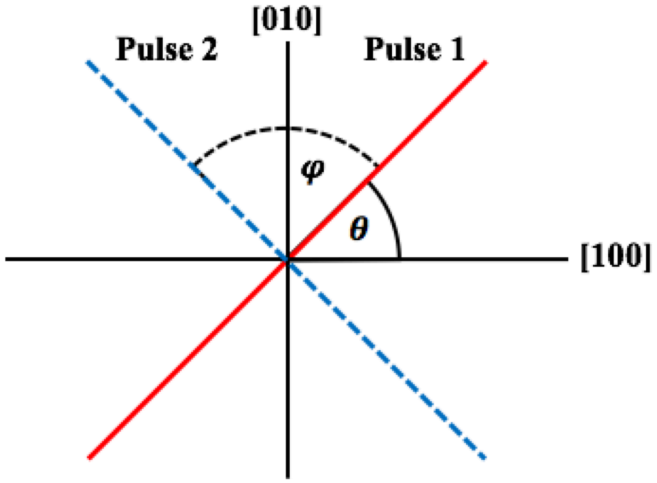

Figure 2.1: Electric polarization of pulses 1 and 2 and the crystalline axes, [100] and [010], which designate the x- and y-directions, respectively. θ is the angle between the polarization of pulse 1 and the [100] axis, and φ is the angle between the polarization of pulses 1 and 2. This figure is obtained from Ref. [1].

respectively:

$$|e_1, k\rangle = \cos\theta\,|e_x, k\rangle + \sin\theta\,|e_y, k\rangle\,, \tag{2.7}$$

$$|e_2, k\rangle = \cos(\theta+\varphi)\,|e_x, k\rangle + \sin(\theta+\varphi)\,|e_y, k\rangle\,, \tag{2.8}$$

where θ is the angle between pump pulse 1 and the x axis, and φ is the relative angle between pump pulses 1 and 2, as shown in Fig. 2.1. $E_1(t)$ and $E_2(t)$ are the optical electric field of pump pulses 1 and 2, respectively, and are expressed by $E_1(t) = E_0 f(t)$ and $E_2(t) = E_0 f(t - t_{12})$. The function $f(t)$ is the Gaussian pulse envelope, which is defined by

$$f(t) = \frac{1}{\sqrt{\pi}\sigma\Omega_0}\exp\left(-\frac{t^2}{\sigma^2}\right), \tag{2.9}$$

where, E_0 is the amplitude of the electric field and σ is the pulse width.

In this model, we consider the process by which coherent phonons are generated under resonant excitation to slightly above the band edge of

GaAs. It should be noted that the band gap depends on the temperature [42] as well as on the doping rate [43]. We introduce the effective response function $F(t)$ phenomenologically, which describes the electronic transition rate to the energy region relevant to the resonant Raman scattering. Formally, $F(t)$ is written as

$$F(t) = \sum_k |\mu_k|^2 e^{-\frac{i}{\hbar}(\varepsilon_k - \varepsilon_g)t - \eta|t|/\hbar}, \quad (\eta = 0_+), \tag{2.10}$$

in which μ_k is the effective transition dipole moment from the ground state to $|e_x, k\rangle$ and $|e_y, k\rangle$ in the excited states. In actual calculations, we adopt a simple form,

$$F(t) \propto |\mu|^2 \exp\left(-i\Omega_c t - \Gamma|t|\right), \tag{2.11}$$

where Ω_c is the central frequency and Γ is the electronic phase relaxation rate in the conduction band. The main origin of the phase relaxation is the inhomogeneous width in the conduction band as described by the summation in Eq. (2.10). The Fourier transformation of Eq. (2.11) is a Lorentzian function $I_{\text{eff}}(\Omega) = I_0(\Gamma/\pi)/((\Omega - \Omega_c)^2 + \Gamma^2)$, which corresponds to an effective density of states relevant to ISRS with a center energy of $\hbar\Omega_c$ and a bandwidth of $\hbar\Gamma$.

2.2.2 Transition paths for generating phonons via ISRS process

We adopt the density-matrix formalism to derive the generation amplitude of coherent phonons by solving the time-dependent Schrödinger equation with the second-order perturbation. The change of the amplitude, ΔR, of the reflectivity is proportional to the expectation value of the LO phonon

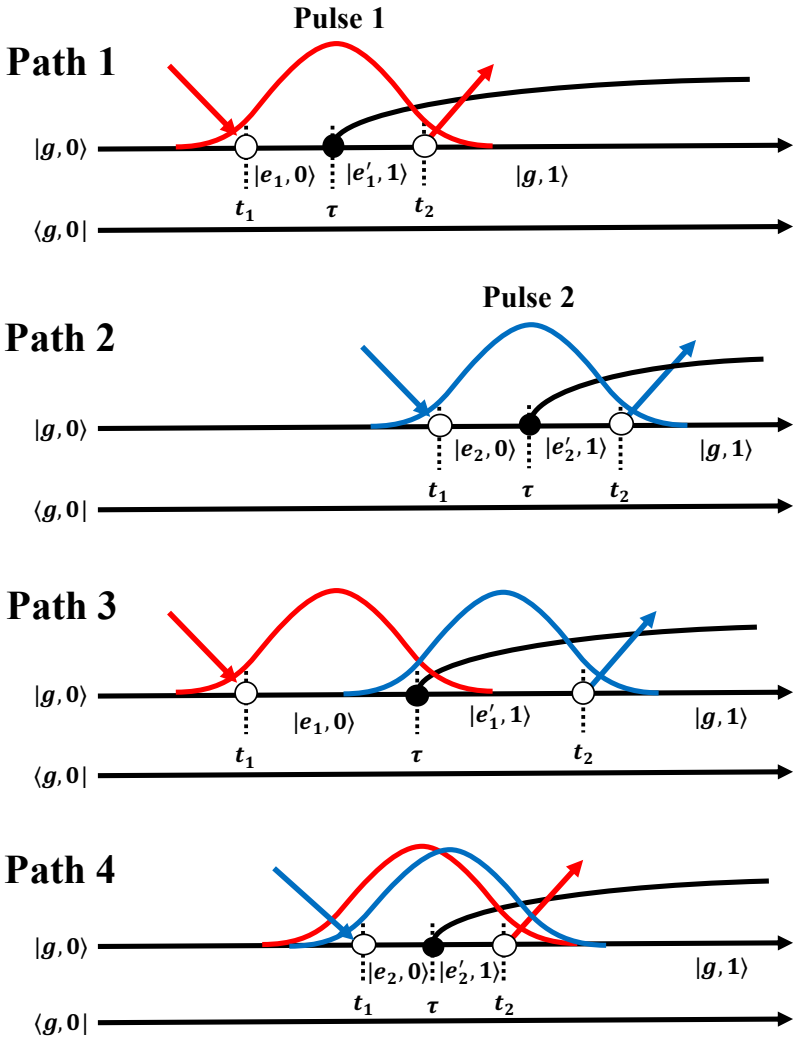

Figure 2.2: Double-sided Feynman diagrams for generating LO phonons by pulses 1 and 2. The red and blue curves illustrate the Gaussian shapes of pulses 1 and 2, respectively. The open circles mark the time when electronic excitation and de-excitation are induced by the optical electric field. The solid circle marks the moment when a phonon is generated. This figure is obtained from Ref. [1].

coordinate, $Q = \sqrt{\hbar/2\omega}(b + b^{\dagger})$.

Figure 2.2 presents double-sided Feynman diagrams for the generation of LO phonons by ISRS with two pump pulses. The initial state in the ket vector is assumed to be the electronic ground state with the zero-phonon state, $|g, 0\rangle = |g\rangle \otimes |0\rangle$, and the final state is $|g, 1\rangle = |g\rangle \otimes |1\rangle$. The kets $|e_1, 0\rangle$, $|e'_1, 1\rangle$, $|e_2, 0\rangle$, $|e'_2, 1\rangle$ denote the electronic excited states induced

by pulses 1 and 2 with zero- and one-phonon states, respectively. In Fig. 2.2, t_1 and t_2 denote the times at which the system interacts with the electric field of the pump pulse, and τ denotes the time at which the phonon is created. Photo-excitation and de-excitation processes occur at t_1 and t_2, respectively. Phonon creation is assumed to occur at an arbitrary time in the electronic excited states ($t_1 \leq \tau \leq t_2$). Electronic excitation and de-excitation occur within a pulse in paths 1 and 2, and occur in different pulses in paths 3 and 4. For the ISRS, after interacting with the pump pulses, the final electron–phonon state is $|g,1\rangle\langle g,0|$ or $|g,0\rangle\langle g,1|$. In the phonon-creation process, the polarization of the electronic state changes via the allowed Raman components ($|e_x\rangle \rightarrow |e_y\rangle$ or $|e_y\rangle \rightarrow |e_x\rangle$) but does not change via the forbidden Raman components ($|e_x\rangle \rightarrow |e_x\rangle$ or $|e_y\rangle \rightarrow |e_y\rangle$). When the polarizations of the pulses are taken into account, the amplitude of the LO phonons is expressed by a coherent superposition of the contributions from the allowed and forbidden Raman scattering processes.

The time evolution of the density operator, $\rho^{op}(t)$, is given by the second-order perturbation calculation, and the expectation value of the LO phonon amplitude is expressed by $\mathrm{Tr}[Q\rho^{op}(t)]$. The relevant part of the density operator $\rho^{op}(t)$ is written as $\rho^{op}(t) = \rho(t)|g,1\rangle\langle g,0|$ where $\rho(t)$ is expressed by the sum for each transition path $\rho_i(t)$ as

$$\rho(t) = \sum_{i=1}^{4} \rho_i(t),$$

as shown in Fig 2.2. For each path i ($i = 1, 2, 3, 4$), $\rho_i(t)$ is given by

$$\rho_1(t) = (\alpha \sin 2\theta + \beta)\, P_{11}(t), \tag{2.12}$$

$$\rho_2(t) = \{\alpha \sin 2\,(\theta + \varphi) + \beta\}\, P_{22}(t), \tag{2.13}$$

$$\rho_3(t) = \{\alpha \sin\,(2\theta + \varphi) + \beta \cos\varphi\}\, P_{12}(t), \tag{2.14}$$

$$\rho_4(t) = \{\alpha \sin\,(2\theta + \varphi) + \beta \cos\varphi\}\, P_{21}(t), \tag{2.15}$$

in which

$$P_{ij}(t) = \left(\frac{E_0}{\hbar}\right)^2 e^{-i\omega t} \sum_k |\mu_k|^2 \int_{-\infty}^{t} dt_2 \int_{-\infty}^{t_2} dt_1 \\ \times\ f_i(t_1) f_j^*(t_2) e^{-\frac{i}{\hbar}(\varepsilon_k - \hbar\Omega_0)(t_2 - t_1)} e^{-\frac{\eta}{\hbar}|t_2 - t_1|} \left(e^{i\omega t_2} - e^{i\omega t_1}\right), \tag{2.16}$$

where ($i, j = 1$ or 2), and the envelope functions are $f_1(t) = f(t)$ and $f_2(t) = f(t - t_{12})e^{i\Omega_0 t_{12}}$. In Eq. (2.16), t is the observation time, which is much later than the time at which the double pulses are irradiated. Therefore, the upper limit of the integral can be replaced by ∞. Furthermore, introducing a pair of variables, (s, u), which are defined as $s = (t_1 + t_2)/2$, $u = t_2 - t_1$, the integration over s can be carried out. (Details of the calculation are shown in Appendix A.) Thus, we find that $P_{ij}(t)$ is given as a function of the pump–pump delay t_{12} as

$$P_{11}(t) = e^{-i\omega t} L(0), \tag{2.17}$$

$$P_{22}(t) = e^{-i\omega(t - t_{12})} L(0), \tag{2.18}$$

$$P_{12}(t) = e^{-i\omega(t - t_{12}/2)} e^{-i\Omega_0 t_{12}} L(t_{12}), \tag{2.19}$$

$$P_{21}(t) = e^{-i\omega(t - t_{12}/2)} e^{i\Omega_0 t_{12}} L(-t_{12}), \tag{2.20}$$

except for a common constant factor, and

$$L(x) = 2i \int_0^\infty du\, e^{-\frac{(u-x)^2}{2\sigma^2}} \sin\left(\frac{\omega u}{2}\right) e^{i\Omega_0 u} F(u). \tag{2.21}$$

The above formulas are the central results of the present work. They predict that the t_{12} dependence of the phonon amplitude will be composed of two types of quantum-path interference. One is the temporal interference expressed by $P_{ij}(t)$, and the other is the geometrical interference given by the θ and φ dependence in the prefactors of $P_{ij}(t)$. Note that the amplitudes of the ISRS using relative-phase-locked double pulses carry the memory of the phases of the pump pulse by which the electron is excited and de-excited. This is explicitly exhibited in the phase factors in P_{ij} shown in Eqs. (2.17)–(2.20). The amplitudes due to paths 1 and 2 do not depend on the phase factor, $\Omega_0 t_{12}$, whereas those from paths 3 and 4 carry the factor $\Omega_0 t_{12}$, which is imprinted on the electronic coherence. Path 4 may be called an anomalous path, because this term represents the process in which the electron is excited by the *delayed pulse* and de-excited by the *advanced pulse*. Therefore, the contribution from path 4 is limited to the small time-delay region at which the two pulses overlap in the time domain.

2.2.3 Transition paths for generating phonons via space-charge field

A vibronic Raman interaction and a surface space-charge field have been discussed as a driving force for coherent phonons in semiconductors. In particular, suppression of a surface space-charge field is the decisive source term for driving the coherent phonons in III-V semiconductors [18]. The initial field distribution is suppressed by the opposite drift

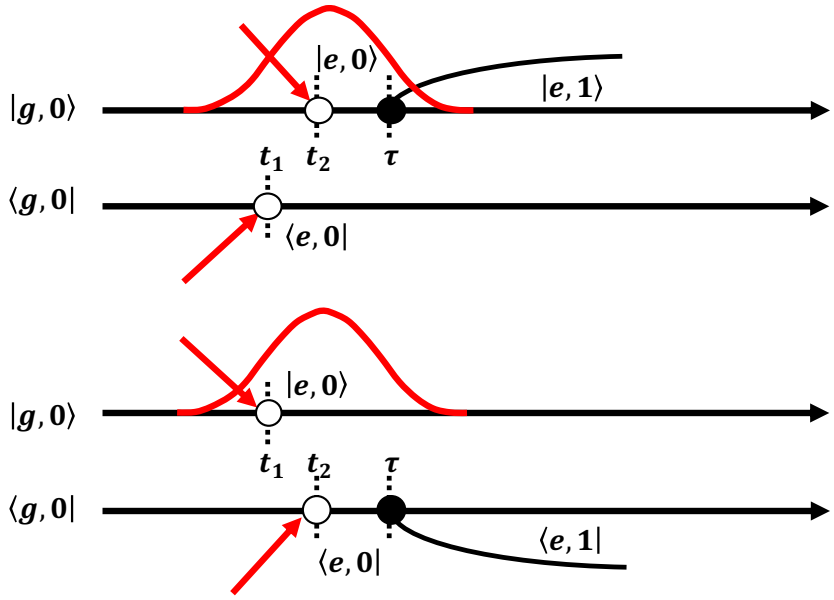

Figure 2.3: Double-sided Feynman diagrams for generation of coherent phonons via suppression of the surface space-charge field. This figure is obtained from Ref. [1].

of the optically induced electrons and holes, and the accompanying depolarization field acts as the nonlinear driving term for the coherent phonons [18]. According to this mechanism, the driving term depends on an optically induced carrier density $\bar{n}$, which is obtained by populations in the electronic excited state ($|e\rangle\langle e|$) in the present model. The density operators for the population in the electronic excited state with phonon polarization ($|e,1\rangle\langle e,0|$ and $|e,0\rangle\langle e,1|$) can be expressed as: $|e,1\rangle\langle e,0| = (\gamma E_{sc}\hbar\omega\mu_k E_0 f(t)e^{-i\Omega_0 t}|e,1\rangle\langle g,0|) \times |g,0\rangle\langle e,0|$, where γ is a strength of interaction and E_{sc} is the space-charge field strength.

Figure 2.3 shows double-sided Feynman diagrams of this interaction, in which $t_2 > t_1$. The phonon is created at time t_2, at which the electronic transition occurs via the dipole interaction, and the population in the electronic excited state is created. The phonon can not be created by the first interaction at t_1, which is different from the impulsive absorption case.

The density matrix with the second-order perturbation is obtained as

$$\rho_{ij}(t) = \gamma E_{sc} \left(\frac{E_0}{\hbar}\right)^2 e^{-i\omega t} \sum_k |\mu_k|^2 \int_{-\infty}^{t} dt_2 \int_{-\infty}^{t_2} dt_1 \; f_i^*(t_1) f_j(t_2) \\ \times e^{\frac{i}{\hbar}(\epsilon_k - \hbar\Omega_0)(t_2 - t_1)} e^{-\frac{\eta}{\hbar}|t_2 - t_1|} \; e^{i\omega t_2} \; |e,1\rangle \langle e,0| + H.c., \tag{2.22}$$

where $f_1(t) = f(t)$ and $f_2(t) = f(t - t_{12})e^{i\Omega_0 t_{12}}$. The upper limit ($t$) of the integral for t_1 and t_2 can be approximately replaced by ∞ for $t \gg t_2$.

2.3 Coherent control calculation with polarized pulses

In the actual calculations, we considered a pair of relative-phase-locked femtosecond pulses (pulses 1 and 2) directed along the z-axis of the (001) surface of a GaAs crystal. The width of each pulse was σ = 30 fs, and the center energy of each pulse was $\hbar\Omega_0$ =1.55 eV, which is above the band gap (1.52 eV). The frequency of the LO phonons was set to 8.8 THz ($\hbar\omega$ =0.036 eV). The energy of the electronic ground state ε_g was set to zero. For the effective response function $F(t)$, we assumed $\Omega_c = \Omega_0$ and $\Gamma = 0.0455$ (fs)$^{-1}$. This decay constant value corresponds to an energy of 0.03 eV ($\hbar\Gamma = 0.03$ eV). The lifetime corresponding to the decay constant is approximately 22 fs. This may be shorter than the population lifetimes which are measured by using angle-resolved-photoelectron spectroscopy (ARPES) experiments [44, 45] (e.g., population lifetime of 165 fs at pump-photon-energy of 1.7 eV for p-type GaAs (110) [44]). The previous ARPERS experiments were not actually measuring the same lifetimes as what is in the present model. This choice of parameter values also reproduced the experimental line shape of the fringe pattern in n-GaAs at 90 K for the double-pulse pumping by parallel polarization case [28]. The electronic coherence in the excited state decays with the decay constant Γ (see details in Appendix B). We could not find a significant shift in an initial coherent-phonon phase due to the lifetime in the previous single-

pulse-excitation experiments [28], although the lifetime dependence [46] is predicted for very short pulse excitation. We neglected the decay of phonons in this work.

The values of α and β depend on the doping rate in GaAs. In intrinsic GaAs, a ratio of $\beta/\alpha = 6$ was used as an example. For n-doped GaAs, the allowed Raman scattering is negligible.

In the following parts of this section, we show the general features of the interference fringes in the coherent LO phonon generated by the allowed and forbidden ISRS processes as a function of the angles θ and φ, and the delay, t_{12}. The amplitude of the LO phonons was obtained by calculating $\mathrm{Tr}[Q\rho(t_{12})]$ with equations (2.12)–(2.15) and taking the absolute values. The electronic and phononic interferences were evaluated from a plot of the phonon amplitude as a function of the delay t_{12} between pulses. The calculations show that the interference pattern changes depending on the polarization angle (i.e., θ or φ). The results for the typical polarization conditions are shown in the following subsections.

2.3.1 Parallel-polarized pulses ($\varphi = 0$)

Figure 2.4 shows the calculated amplitude of LO phonons with $\beta/\alpha = 6$ for parallel-polarized pulses with $\varphi = 0$ and $\theta = 0$ as a function of the pulse delay, t_{12}. There is a slow oscillation ($\sim$ 115-fs period) owing to phonon interference and a fast oscillation ($\sim$ 2.7-fs period) owing to electronic interference. Under the parallel-polarized condition ($\varphi = 0$), all transition paths have the same factor ($\alpha \sin 2\theta + \beta$) of the effect of the Raman tensor according to Eqs. (2.12)–(2.15). Then, the interference pattern is independent of the values α and β. This means that the interference patterns for intrinsic and n-type GaAs are the same. In fact, the interference fringes in Fig. 2.4 agree well with our previously reported experimental

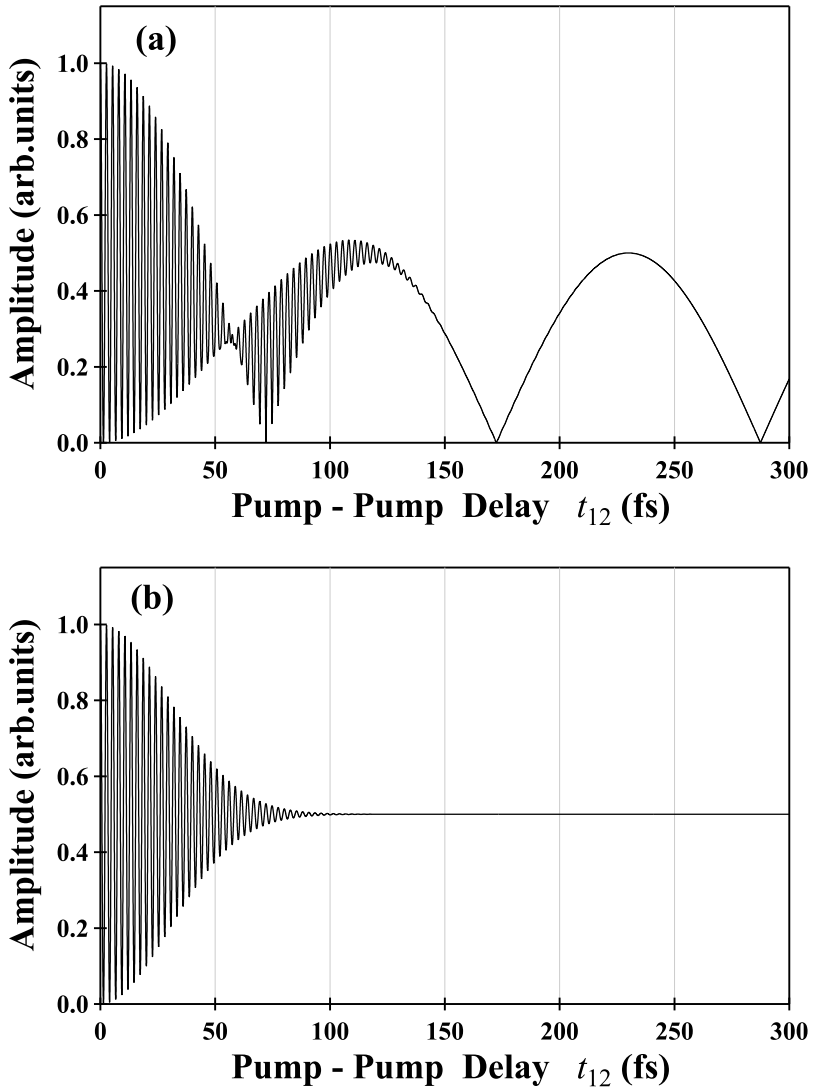

Figure 2.4: (a) Amplitude of LO phonons induced by the parallel-polarized pulses ($\theta = 0$) as a function of the pump–pump delay, t_{12}. (b) Intensity of optical pulses 1 and 2. The vertical axis is normalized such that the maximum value is 1. This figure is obtained from Ref. [1].

results for n-type GaAs (001) [28]. In addition, a change of the angle θ, while keeping the relative angle at 0 degrees, does not change the interference pattern.

The amplitude of the interference fringes with fast oscillations, which indicate electronic coherence, decreased until approximately 50 fs and thereafter increased (i.e., collapse and revival). Electronic coherence is caused by paths 3 and 4. However, path 4 may contribute only at $t_{12} \approx 0$, where

the two pulses overlap. At longer time delays, only path 3 contributes to the electronic interference. Then, the amplitude of the phonon oscillation is given by the absolute value of $P_{11}(t)+P_{22}(t)+P_{12}(t)$, which is approximately proportional to $|1+\exp[i\omega_0 t_{12}]+\exp[-i\Omega_0 t_{12}]|$, as can be seen from Eqs. (2.16) – (2.20). Note that the rapid oscillation due to the electronic interference appears only through the cross term with the slow component $1+\exp[i\omega_0 t_{12}]$ of the phonon interference. Therefore, we attribute the collapse and revival of the electronic interference at about $t_{12} \approx 50$ fs as the result of the destructive phonon interference at a half period.

2.3.2 Orthogonally polarized pulses ($\varphi = \pi/2$)

The interference of the LO phonons generated by the orthogonally polarized pulses with $\varphi = \pi/2$ depends on the angle θ.

At the $\theta = \pi/4$ orientation

Setting $\varphi = \pi/2$ and $\theta = \pi/4$ in Eqs. (2.12)–(2.15), we find

$$\rho_1(t) = (\alpha + \beta)P_{11}(t), \tag{2.23}$$

$$\rho_2(t) = (-\alpha + \beta)P_{22}(t), \tag{2.24}$$

$$\rho_3(t) = 0, \tag{2.25}$$

$$\rho_4(t) = 0. \tag{2.26}$$

Therefore, only the slow oscillation due to the phonon interference is observed in this geometry. Then, LO phonons are generated via only paths 1 and 2, and those generated by pulses 1 and 2 interfere constructively for the forbidden Raman term, and destructively for the allowed component at

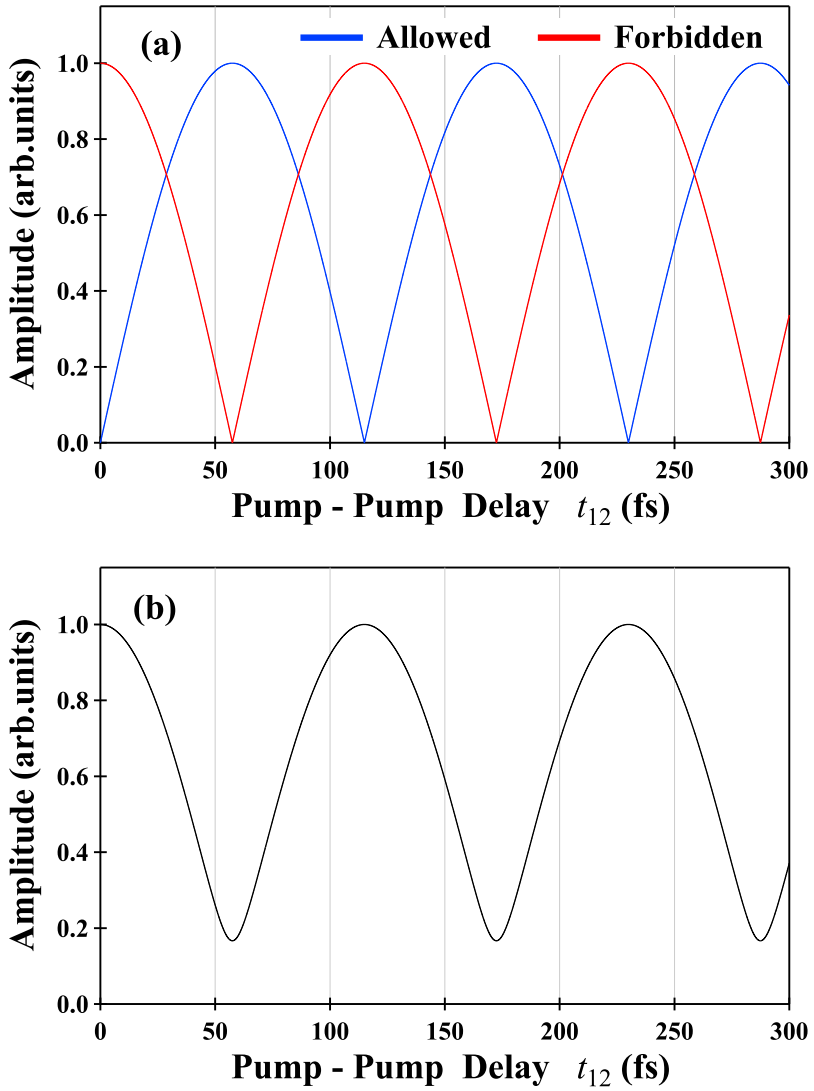

Figure 2.5: Amplitude of the LO phonons induced by the orthogonally polarized pulses ($\varphi = \pi/2$ and $\theta = \pi/4$) as a function of the delay, t_{12}. (a) The red and blue curves show the amplitude of phonons induced by the allowed and forbidden Raman scattering, respectively. (b) Phonons induced via the total Raman tensor with $\beta/\alpha = 6$. The vertical axis is normalized such that the maximum value is 1. This figure is obtained from Ref. [1].

each period of the delay, t_{12}, as shown in Fig. 2.5(a). These features are explained as below.

From Eqs. (2.23)–(2.26), the density matrix, $\rho(t)$, is obtained as $\rho(t) = \alpha(P_{11}(t) - P_{22}(t)) + \beta(P_{11}(t) + P_{22}(t))$. Therefore, in the allowed and forbidden Raman scattering, phonons are added and subtracted by pulses 1 and 2, respectively. Thus, the LO phonons induced by the allowed Ra-

man components by pulses 1 and 2 have opposite phases, such that they interfere destructively at each half cycle. By contrast, those induced by the forbidden components have the same phase, such that they interfere constructively.

Figure 2.5(b) shows the LO phonons induced via the total Raman scattering with $\beta/\alpha = 6$. Only the slow oscillation due to the phonon interference is found. An interesting feature is found at $t_{12} = 60$ fs, which corresponds to $t_{12} \cong \pi/\omega$. The phonon amplitude does not decrease to zero in the destructive interference of phonons. This is because of the contribution of the allowed Raman scattering.

At the $\theta = 0$ orientation

For $\varphi = \pi/2$ and $\theta = 0$, we find

$$\rho_1(t) = \beta P_{11}(t), \tag{2.27}$$

$$\rho_2(t) = \beta P_{22}(t), \tag{2.28}$$

$$\rho_3(t) = \alpha P_{12}, \tag{2.29}$$

$$\rho_4(t) = \alpha P_{21}. \tag{2.30}$$

In this geometry, only phonon interference is induced by the forbidden Raman scattering, and electronic interference is induced by the allowed scattering on paths 3 and 4, as shown in Fig. 2.6(a). The amplitude of the LO phonons induced via forbidden Raman scattering at $\theta = 0$ is the same as that at $\theta = \pi/4$. By contrast, the amplitude of the LO phonons induced via the allowed Raman scattering shows interference fringes with fast oscillation at a frequency of $2\Omega_0$ owing to electronic interference during the overlap between pulses. Figure 2.6(b) shows the amplitude of the

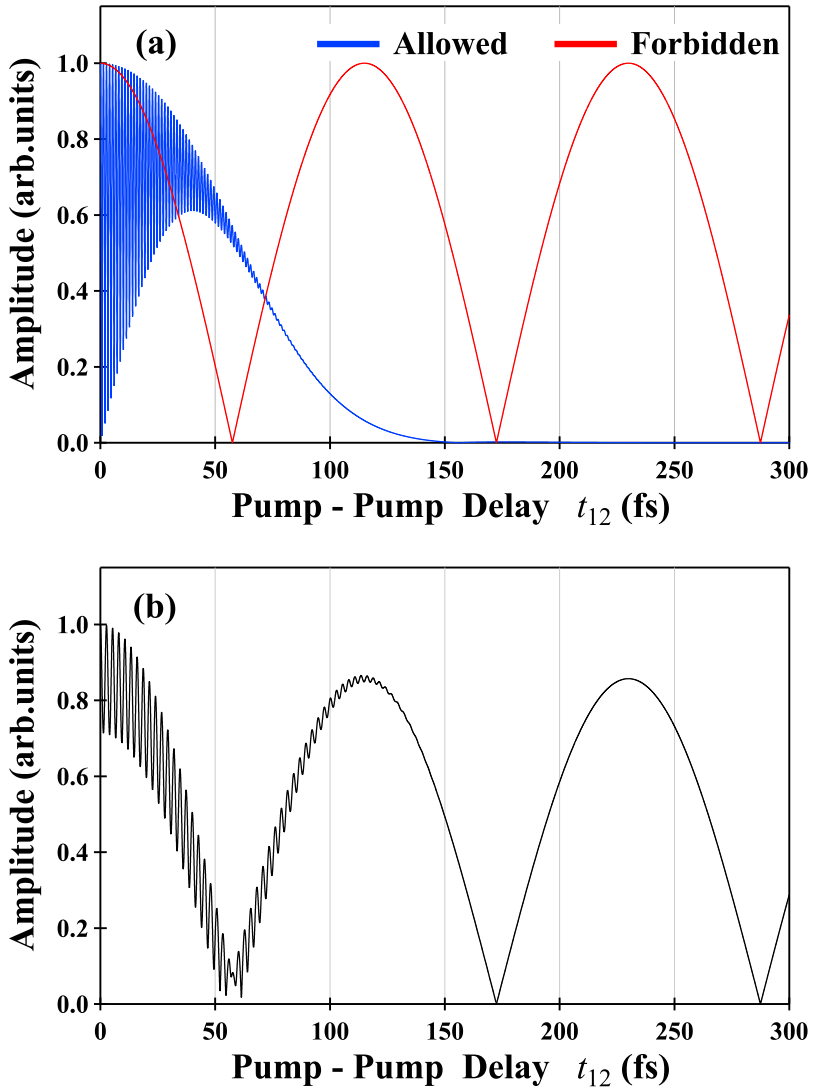

Figure 2.6: Amplitude of the LO phonons induced by the orthogonally polarized pulses ($\varphi = \pi/2$ and $\theta = 0$) as a function of the delay, t_{12}. (a) The red and blue curves show the amplitude of phonons induced by the allowed and forbidden Raman scattering, respectively. (b) Phonons induced via the total Raman tensor with $\beta/\alpha = 6$. The vertical axis is normalized such that the maximum value is 1. This figure is obtained from Ref. [1].

LO phonons induced via both the allowed and forbidden Raman scattering with $\beta/\alpha = 6$. The interference fringes have a fast oscillation with a frequency of Ω_0. However, the superposition of the results from each Raman tensor is different from the interference fringes in Fig. 2.6(b), because there is no contribution from the cross-terms due to the quantum-path interference. Furthermore, Fig. 2.6(a) and (b) show the difference of the

rapidly oscillating electronic interference fringes. These oscillate at $2\Omega_0$ for allowed Raman scattering only (Fig. 2.6(a)) and at Ω_0 for both allowed and forbidden scattering (Fig. 2.6(b)). These features can be explained as below.

In the condition ($\varphi = \pi/2, \theta = 0$), the allowed Raman scattering (Fig. 2.6(a)) generates LO phonons via paths 3 and 4. Paths 3 and 4 induce factors of $\exp(-i\Omega_0 t_{12})$ and $\exp(i\Omega_0 t_{12})$, respectively. When the double pulses overlap at $t_{12} \sim 0$, the phonon amplitude is roughly proportional to $|\exp(-i\Omega_0 t_{12}) + \exp(i\Omega_0 t_{12})|$, resulting in the $2\Omega_0$ oscillation. As the delay time increases, the contribution of path 4 decreases rapidly, so that the rapid oscillation disappears. By contrast, the coexistence of allowed and forbidden Raman scattering induces phonon interference via paths 1 and 2. The contribution for the slow oscillation is treated as a constant (e.g., denoted as A). The absolute value of the sum $|A + \exp(-i\Omega_0 t_{12}) + \exp(i\Omega_0 t_{12})|$ causes the dominant Ω_0 oscillation because the value of A (the contribution of the β term) is much larger than unity by assumption.

2.3.3 Pulses with a relative polarization angle of $\pi/4$

Figure 2.7 shows the calculated amplitude of LO phonons with β/α =6 for pulses with a relative polarization angle of $\pi/4$ as a function of the pulse delay t_{12}. The electronic and phonon interference fringes are found at $\theta = 0$ and $\theta = \pi/2$. In contrast with the parallel-polarized pulses, the fringe pattern is slightly dependent on θ. For example, the amplitude of the electronic interference at $t_{12} \approx 50$ fs for $\theta = \pi/2$ is larger than that at $\theta = 0$. The interference fringes in this polarization condition can be understood as the superposition of interference by the parallel- and orthogonally polarized pulses.

In the model, we used the single-electron approximation. This might be

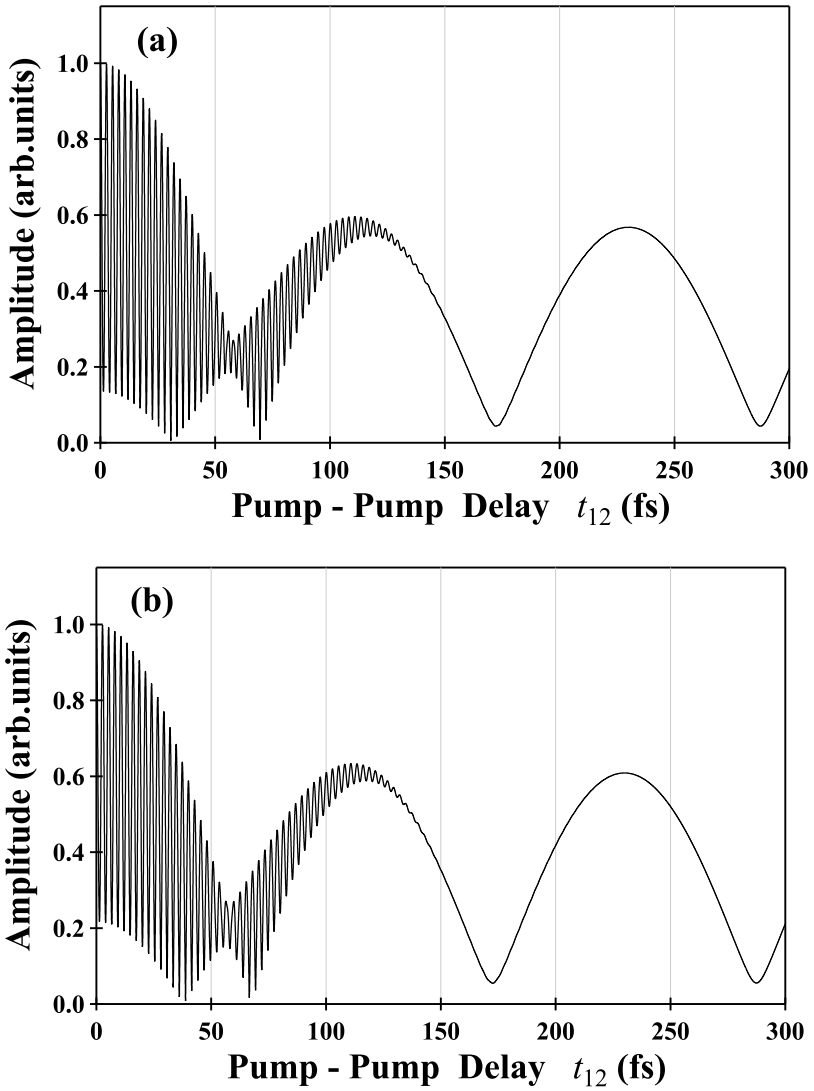

Figure 2.7: Amplitude of LO phonons induced by pulses with a relative polarization angle of $\pi/4$ with (a) $\theta = 0$, and (b) $\theta = \pi/2$. The vertical axis is normalized such that the maximum value is 1. This figure is obtained from Ref. [1].

reasonable for the ISRS process, and the calculated results well represent the experimental results for the parallel condition [28]. The multi-electron effects, for example, the relaxation by electron-electron interactions, might be considered for an absorption process.

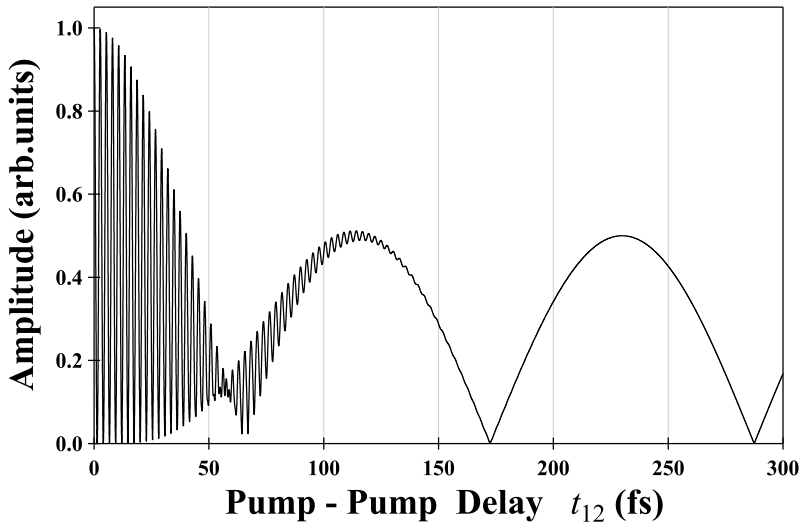

Figure 2.8: Phonon amplitude as a function of t_{12} for the space-charge model. The dephasing rate Γ is set to be 0.03 eV. The vertical axis is normalized such that the maximum value is 1. This figure is obtained from Ref. [1].

2.3.4 Case of the mechanism with space-charge field

Figure 2.8 shows the amplitude of the coherent phonons generated by the double pulse with parallelly polarized-pulse-excitation via the suppression of the space-charge field as a function of the pump-pump delay (t_{12}). The dephasing rate Γ was set to be 0.03 eV. The interference fringe with a period of 2.7 fs also shows a collapse and revival feature as that via the ISRS process with a large β. However, the amplitude of the phonons at timing when the electronic interference collapse (approximately 60 fs) is smaller than that via the ISRS process. The interference fringes obtained for the space-charge fields with $\Gamma = 0.03$ eV are similar to that for the ISRS with $\Gamma = 0.06$ eV (shown in Appendix B). The polarization dependence of the amplitude of LO phonons are same as that for the large β-case for the ISRS process because the electron-phonon interaction is isotropic.

2.4 Summary

We derived a theoretic model for the coherent control of LO phonons in GaAs (001) by relative-phase locked and polarization-controlled double-pulse excitation. By considering the impulsive stimulated Raman scattering processes both for the allowed and forbidden transitions, a variety of the interference fringe patterns in the delay-time dependence of the LO phonon amplitude were predicted theoretically. These features are the results of the quantum-path interference in the time domain working together with the additional degrees of freedom of the polarization of photons.

In the present work, we adopted a model of GaAs as the simplest test material in this subject. Since the Raman scattering in solids is directly related to the microscopic origin of the interactions between the local deformations of solids and the electronic structures, the effect of the optical polarization plays a quite important role in the generation and detection processes of the coherent phonons. This is especially true in the case of coherent phonons in materials with asymmetric interaction modes, for example, bismuth, which has more than two optical phonon modes and electronic states and includes Jahn-Teller interactions [47]. The experimental and theoretical studies of the coherent phonons will be further extended by taking account of the polarization correlation working with the phase-locked double pulse excitation method.

Appendix A: The perturbative solution of density operator

We show details of the perturbation calculation of the density operator in ISRS process and derivation of Eqs. (2.16)-(2.20). In the interaction picture, the time evolution of the electron-phonon composite state $|\psi(t)\rangle$

is given by:

$$i\hbar\frac{d}{dt}\left|\tilde{\psi}(t)\right\rangle = \tilde{H}_I(t)\left|\tilde{\psi}(t)\right\rangle, \tag{A.2.1}$$

in which $\left|\tilde{\psi}(t)\right\rangle \equiv \exp[iHt/\hbar]\left|\psi(t)\right\rangle$ and $\tilde{H}_I(t) = e^{iHt/\hbar}H_I(t)e^{-iHt/\hbar}$ with a wave function $\left|\psi(t)\right\rangle$ in the Schrödinger picture. The equation in Eq.(A.2.1) is formally solved as

$$\left|\tilde{\psi}(t)\right\rangle = \exp_+\left[-\frac{i}{\hbar}\int_{-\infty}^{t}\tilde{H}_I(\tau)d\tau\right]\left|\tilde{\psi}(-\infty)\right\rangle. \tag{A.2.2}$$

The initial state is assumed as $\left|\tilde{\psi}(-\infty)\right\rangle = |g,0\rangle$. We calculated the integral with the second-order perturbative expansion.

The time evolution of the density operator by ISRS is expressed by the double-sided Feynman diagrams (Fig. 2.2). Here, we describe the calculation for the path 1 as an example. For convenience, the excited electronic states are denoted as $|e_1,k\rangle \rightarrow |e_1\rangle$ and $|e_2,k\rangle \rightarrow |e_2\rangle$. In the case of path 1, the photo-excitation and de-excitation processes of the electronic states are caused by pulse 1.

At time t_1, the dipole interaction with pulse 1 induces photo-excitation process ($|g,0\rangle \rightarrow |e_1,0\rangle$), and at time τ, the phonon is created ($|e_1,0\rangle \rightarrow |e_1^{'},1\rangle$) due to electron-phonon interaction. By the interaction, polarization of the electronic state is changed by the terms ($|e_x\rangle\langle e_y|$ and $|e_y\rangle\langle e_x|$) or preserved by the terms ($|e_x\rangle\langle e_x|$ and $|e_y\rangle\langle e_y|$). At time t_2, the dipole interaction induces the de-excitation process of the electronic state ($|e_1^{'},1\rangle \rightarrow |g,1\rangle$).

Then the density operator $\rho_1(t)$ was obtained as

$$\begin{aligned}\rho_1(t) = i\left(\alpha\sin 2\theta+\beta\right)\sum_k\left(\frac{\mu_k E_0}{\hbar}\right)^2\omega e^{-i\omega t}\int_{t_1}^{t_2}d\tau\int_{-\infty}^{t}dt_2\int_{-\infty}^{t_2}dt_1 \\ \times f(t_1)f(t_2)e^{-\frac{i}{\hbar}(\varepsilon_k-\hbar\Omega_0)(t_2-t_1)}e^{-\frac{\eta}{\hbar}|t_2-t_1|}e^{i\omega\tau}\left|g,1\right\rangle\left\langle g,0\right|.\end{aligned} \tag{A.2.3}$$

Since the only term involved in the integration of time τ is $e^{i\omega\tau}$, we calculate $\int_{t_1}^{t_2} e^{i\omega\tau} d\tau$ and get

$$\begin{aligned}\rho_1(t) = (\alpha \sin 2\theta + \beta) \left(\frac{E_0}{\hbar}\right)^2 e^{-i\omega t} \sum_k |\mu_k|^2 \int_{-\infty}^{t} dt_2 \int_{-\infty}^{t_2} dt_1 \\ \times f(t_1) f(t_2) e^{-\frac{i}{\hbar}(\varepsilon_k - \hbar\Omega_0)(t_2 - t_1)} e^{-\frac{\eta}{\hbar}|t_2 - t_1|} \left(e^{i\omega t_2} - e^{i\omega t_1}\right) |g,1\rangle \langle g,0| \\ = (\alpha \sin 2\theta + \beta) P_{11}(t) |g,1\rangle \langle g,0| . \end{aligned} \tag{A.2.4}$$

The term $\alpha \sin 2\theta + \beta$ comes from $\langle e_1 | e_1^{'} \rangle$:

$$\begin{aligned}\langle e_1 | e_1^{'} \rangle &= \alpha (\sin\theta \cos\theta + \sin\theta \cos\theta) + \beta \left(\cos^2\theta + \sin^2\theta\right) \\ &= \alpha \sin 2\theta + \beta. \end{aligned} \tag{A.2.5}$$

At a long time delay t from the pump pulses, the upper limit of the integral can be replaced by ∞. We performed the integration by substitution with $t_1 = s - u/2,\ t_2 = s + u/2$. Using these parameters, we rewrite the terms $f(t_1)f(t_2)$ and $e^{i\omega t_2} - e^{i\omega t_1}$ as

$$f(t_1) f(t_2) = \frac{1}{\pi\sigma^2\Omega_0^2} \exp\left(-\frac{2s^2}{\sigma^2} - \frac{u^2}{2\sigma^2}\right), \tag{A.2.6}$$

$$e^{i\omega t_2} - e^{i\omega t_1} = 2ie^{i\omega s} \sin\left(\frac{\omega u}{2}\right), \tag{A.2.7}$$

and get the function $P_{11}(t)$ as a function of s and u:

$$\begin{aligned}P_{11}(t) = 2iAe^{-i\omega t} \sum_k |\mu_k|^2 \int_{-\infty}^{\infty} ds \exp\left(-\frac{2s^2}{\sigma^2}\right) e^{i\omega s} \\ \times \int_0^{\infty} du \exp\left(-\frac{u^2}{2\sigma^2}\right) e^{-\frac{i}{\hbar}\varepsilon_k u} e^{i\Omega_0 u} e^{-\frac{\eta}{\hbar}|u|} \sin\left(\frac{\omega u}{2}\right), \end{aligned} \tag{A.2.8}$$

where $A = \left(E_0/(\sqrt{\pi}\sigma\Omega_0\hbar)\right)^2$. The integration over s is a Gaussian integral, which gives a common constant ($G = \sqrt{\pi/2\sigma^2}\exp(-\sigma^2\omega^2/8)$) for each path. Therefore, we summarize the common constant factor as

$B = AG$, which yields the equation

$$P_{11}(t) = Be^{-i\omega t}\, 2i \int_0^\infty du \exp\left(-\frac{u^2}{2\sigma^2}\right) \sin\left(\frac{\omega u}{2}\right) e^{i\Omega_0 u} F(u)$$
$$= Be^{-i\omega t} L(0). \tag{A.2.9}$$

Appendix B: Γ dependence

We calculated the amplitude of LO phonons with $\beta/\alpha = 6$ for parallel-polarized pulses with $\phi = 0$ and $\theta = 0$ as a function of the pulse delay t_{12} and several Γ values ($\hbar\Gamma$ = 0.01, 0.02, and 0.06 (eV)), as shown in Fig. B 2.1. With increasing decay constant Γ, the electronic coherence decreased at a faster rate. The electronic interference fringes show the collapse at time t_c $(= \pi/\omega)$ and revival. The amplitude of the LO phonons at t_c decreases with increasing Γ.

References

[1] I. Takagi, Y. Kayanuma, and K. G. Nakamura, Phys. Rev. B **104**, 134301 (2021).

[2] D. J. Tannor and S. A. Rice, J. Chem. Phys. **83**, 5013 (1985).

[3] P. Brumer and M. Shapiro, Chem. Phys. Letters **126**, 541 (1986).

[4] D. J. Tannor, R. Kosloff, and S. A. Rice, J. Chem. Phys. **85**, 5805 (1986).

[5] D. Meshulach and Y. Silberberg, Nature **396**, 239 (1998).

[6] T. C. Weinacht, J. Ahn, and P. H. Bucksbaum, Nature **397**, 233 (1999).

[7] H. Katsuki, H. Chiba, B. Girard, C. Meier, and K. Ohmori, Science **311**, 1589 (2006).

[8] M. P. A. Branderhorst, P. Londero, P. Wasylczyk, C. Brif, R. L. Kosut, H. Rabitz, and I. A. Walmsley, Science **320**, 638 (2008).

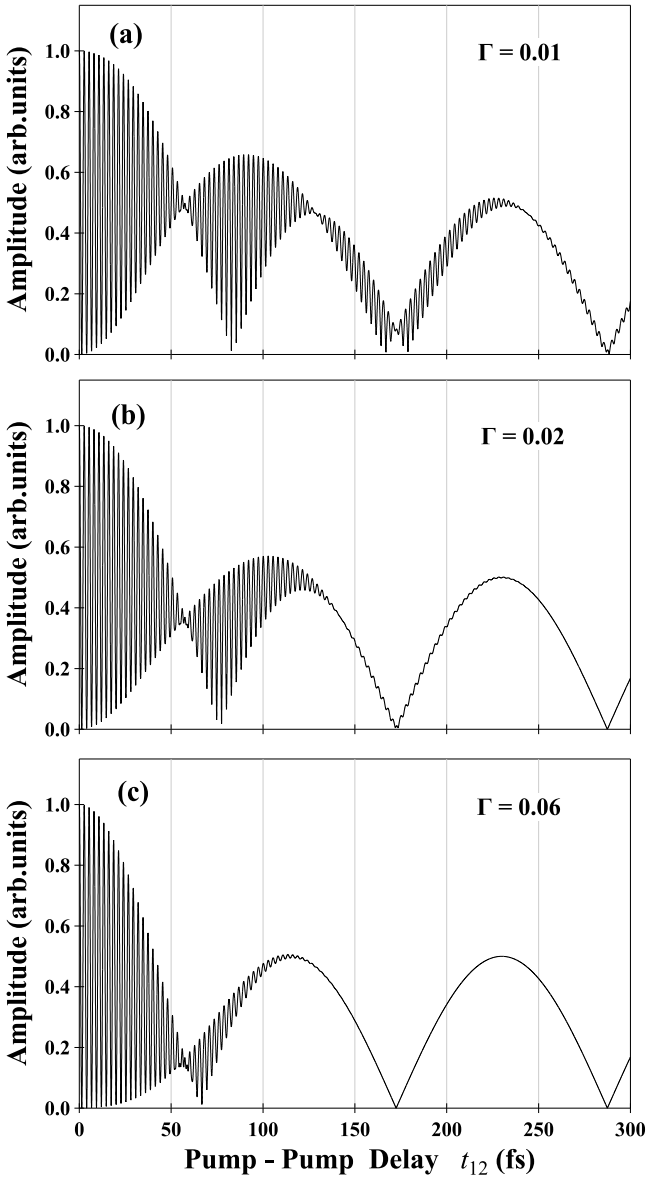

Figure B 2.1: Amplitude of LO phonons for parallel polarization for different decay constants: (a) $\hbar\Gamma = 0.01$, (b) $\hbar\Gamma = 0.02$, and (c) $\hbar\Gamma = 0.06$ (eV). The vertical axis is normalized such that the maximum value is 1. This figure is obtained from Ref. [1].

[9] G. Higgins, F. Pokorny, C. Zhang, Q. Bodart, and M. Hennrich, Phys. Rev. Lett. **119**, 220501 (2017).

[10] M. U. Wehner, M. H. Ulm, D. S. Chemla, and M. Wegener, Phys. Rev. Lett. **80**, 1992 (1998).

[11] M. V. G. Dutt, L. Childress, L. Jiang, E. Togan, J. Maze, F. Jelezko, A. S. Zibrov, P. R. Hemmer, and M. D. Lukin, Science **316**, 1312 (2007).

[12] D. Press, T. D. Ladd, B. Zhang, and Y. Yamamoto, Nature **456**, 218 (2008).

[13] H. Katsuki, Y. Kayanuma, and K. Ohmori, Phys. Rev. B **88**, 014507 (2013).

[14] H. Tahara and Y. Kanemitsu, Phys. Rev. B **90**, 245203 (2014).

[15] B. Pingault, D.-D. Jarausch, C. Hepp, L. Klintberg, J. N. Becker, M. Markham, C. Becher, and M. Atatüre, Nat. Commun. **8**, 15579 (2017).

[16] H. Mashiko, Y. Chisuga, I. Katayama, K. Oguri, H. Masuda, J. Takeda, and H. Gotoh, Nat. Commun. **9**, 1468 (2018).

[17] Y.-X. Yan, E. B. Gamble, and K. A. Nelson, J. Chem. Phys. **83**, 5391 (1985).

[18] G. C. Cho, W. Kütt, and H. Kurz, Phys. Rev. Lett. **65**, 764 (1990).

[19] H. J. Zeiger, J. Vidal, T. K. Cheng, E. P. Ippen, G. Dresselhaus, and M. S. Dresselhaus, Phys. Rev. B **45**, 768 (1992).

[20] R. Merlin, Solid State Commun **102**, 207 (1997).

[21] T. Dekorsy, G. C. Cho, and H. Kurz, "Coherent phonons in condensed media", in *Light scattering in solids viii: fullerenes, semiconductor surfaces, coherent phonons*, edited by M. Cardona and G. Güntherodt (Springer Berlin Heidelberg, Berlin, Heidelberg, 2000), pp. 169–209.

[22] K. G. Nakamura, Y. Shikano, and Y. Kayanuma, Phys. Rev. B **92**, 144304 (2015).

[23] A. M. Weiner, D. E. Leaird, G. P. Wiederrecht, and K. A. Nelson, J. Opt. Soc. Am. B **8**, 1264 (1991).

[24] T. Dekorsy, W. Kütt, T. Pfeifer, and H. Kurz, Europhys. Lett. **23**, 223 (1993).

[25] M. Hase, K. Mizoguchi, H. Harima, S. Nakashima, M. Tani, K. Sakai, and M. Hangyo, Appl. Phys. Lett. **69**, 2474 (1996).

[26] H. Takahashi, K. Kato, H. Nakano, M. Kitajima, K. Ohmori, and K. G. Nakamura, Solid State Commun **149**, 1955 (2009).

[27] J.-H. Kim, A. Nugraha, L. Booshehri, E. Hároz, K. Sato, G. Sanders, K.-J. Yee, Y.-S. Lim, C. Stanton, R. Saito, and J. Kono, Chem. Phys. **413**, 55 (2013).

[28] K. G. Nakamura, K. Yokota, Y. Okuda, R. Kase, T. Kitashima, Y. Mishima, Y. Shikano, and Y. Kayanuma, Phys. Rev. B **99**, 180301 (R) (2019).

[29] H. Matsumoto, T. Kitashima, T. Maruhashi, I. Takagi, Y. Kayanuma, and K. G. Nakamura, Solid State Commun **327**, 114215 (2021).

[30] T. Pfeifer, T. Dekorsy, W. Kütt, and H. Kurz, Appl. Phys. A **55**, 482 (1992).

[31] K. Ishioka, A. K. Basak, and H. Petek, Phys. Rev. B **84**, 235202 (2011).

[32] C. Trallero-Giner, A. Cantarero, and M. Cardona, Phys. Rev. B **40**, 4030 (1989).

[33] A. V. Kuznetsov and C. J. Stanton, Phys. Rev. B **51**, 7555 (1995).

[34] T. E. Stevens, J. Kuhl, and R. Merlin, Phys. Rev. B **65**, 144304 (2002).

[35] J. D. Lee and M. Hase, Phys. Rev. Lett. **101**, 235501 (2008).

[36] Y. Shinohara, K. Yabana, Y. Kawashita, J.-I. Iwata, T. Otobe, and G. F. Bertsch, Phys. Rev. B **82**, 155110 (2010).

[37] Y. Watanabe, K.-i. Hino, M. Hase, and N. Maeshima, Phys. Rev. B **95**, 014301 (2017).

[38] A. Yamada and K. Yabana, Phys. Rev. B **99**, 245103 (2019).

[39] F. Glerean, S. Marcantoni, G. Sparapassi, A. Blason, M. Esposito, F. Benatti, and D. Fausti, J PHYS B-AT MOL OPT **52**, 145502 (2019).

[40] T. Kimata, K. Yoda, H. Matsumoto, H. Tanabe, F. Minami, Y. Kayanuma, and K. G. Nakamura, Phys. Rev. B **101**, 174301 (2020).

[41] P. Y. Yu and M. Cardona, *Fundamentals of semiconductors: physics and materials properties*, 3rd ed. (Springer Berlin, 2001).

[42] M. D. Sturge, Phys. Rev. **127**, 768 (1962).

[43] H. C. Casey, D. D. Sell, and K. W. Wecht, J. Appl. Phys. **46**, 250 (1975).

[44] J. Kanasaki, H. Tanimura, and K. Tanimura, Phys. Rev. Lett. **113**, 237401 (2014).

[45] A. Alexandrou, V. Berger, and D. Hulin, Phys. Rev. B **52**, 4654 (1995).

[46] J. J. Li, J. Chen, D. A. Reis, S. Fahy, and R. Merlin, Phys. Rev. Lett. **110**, 047401 (2013).

[47] Y. Kayanuma and K. G. Nakamura, Phys. Rev. B **95**, 104302 (2017).

Chapter 3
Ultrafast quantum path interferometry to determine the electronic decoherence time in n-GaAs

In this chapter, we demonstrate how to measure the decoherence time of electronic excited states in n-type gallium arsenide crystals as a test sample using a relative-phase locked double pulse excitation method. The electronic coherence shows uplifting and splitting in the collapse and revival of the electronic interference, which is sensitive to temperature, and these features are well reproduced using a simple quantum mechanical model. The evaluation and discussion are based on comparative analyses with theoretical calculations. This work is published in Physical Review B [1].

3.1 Introduction

Quantum coherence represents a superposition of quantum states and has been widely studied in atomic, molecular, biological, and solid-state systems [2–10]. In solid-state materials, any coherence disappears quickly due to interactions with the environment, and consequently the decoherence time and mechanism are still not well understood.

Optical phonons are often coherently induced by irradiating a crystal lattice with ultrashort optical pulses [11–16]. These can be observed using a pump-probe method in time-resolved reflection or transmission measurements [17–21]; often called coherent optical phonons, they are a super-

position of phonon Fock states that can be interpreted as a coherence of phonon states. During the photoexcitation process, the wave packets of quantum superpositions are generated via several quantum transition pathways, and the evolution of phonon decoherence can be evaluated via the decay of coherent oscillation in transient reflection or transmission. By using double-pump pulses, the generated wave packets undergo quantum interference with each other [22–24]. These quantum interferences can be manipulated by controlling the polarization and the delay time between double pulses, which is called coherent control [25–28]. Furthermore, by applying a relative phase of the optical pulses, not only phonon interference but also electronic interference can be observed [29, 30].

In our previous work, we have performed quantum path interferometry to study the quantum coherence of the electron–phonon composite system in n-type gallium arsenide (n-GaAs) single crystals using femtosecond pulses with relative phase-locking [30, 31]. Under the parallel polarization of double-pump pulses, both electronic coherence with rapid oscillation ($\sim$ 2.7 fs period) and phononic interference with slow oscillation ($\sim$ 115 fs period) can be simultaneously observed. Electronic coherence is also found to have a longer lifetime than the optical interference, and also shows collapse-revival behavior [30]. In contrast, with orthogonal polarization, only phononic interference is observed in this situation, with no electronic interference being observed [31].

This interference behavior can be theoretically explained using a simple quantum mechanical model, consisting of two electronic bands and a single longitudinal optical (LO) phonon mode, with a classical optical electric field and the Raman tensor [30, 32]. Theory predicts that uplifting and splitting will be observable in the collapse and revival of the electronic interference, when the two pump pulses are at $\pi/4$ relative polarization. Moreover, this characteristic uplift and splitting width is sensitively de-

pendent on the decoherence in n-GaAs. This allows decoherence time to be determined quantitatively from the values of the height and width in the interference pattern.

In this chapter, we demonstrate the quantitative determination of the electronic decoherence time in the electron–phonon composite system (n-GaAs), using ultrafast quantum path interferometry experiments with relative-phase locking and $\pi/4$ polarization. Temperature dependence of the electronic decoherence time is also discussed.

3.2 Experimental details

Using a pump-probe method with double-pump pulses, we measure the transient reflectance from the (001) plane in a single crystal of n-type GaAs with a thickness of 0.35 mm. The sample is doped with Si at a donor concentration of $1.0 \times 10^{18}\ \mathrm{cm}^{-3}$, and set in a cryostat.

This experimental setup (Fig. 3.1) uses a Ti: Sapphire laser (KM laser), producing pulses of width $\sim$ 60 fs at a repetition rate of 94 MHz centered at approximately 800 nm. Chirped mirrors compensate for the dispersion in group velocity of the optics. A beam splitter divides the pulse into pump and probe pulses. The pump pulse is directed into a scan delay driven at 20 Hz to control the pump-probe delay, and a custom-built Michelson-type interferometer to create double-pump pulses. In this interferometer, we use a feedback stage (Sigma Tech Co. Ltd.) in the optical path of pump 2 to control the pump-pump time delay (t_{12}) in steps of 300 attoseconds. A wave plate ($\lambda/2$) and a linear polarizer placed in each optical path set the polarization direction and optical intensity before a lens focuses the pump and probe pulses onto the n-GaAs crystal in the cryostat. A portion of the double-pump pulses created by the Michelson-type interferometer is extracted by a beam sampler and introduced into the optical monitor sys-

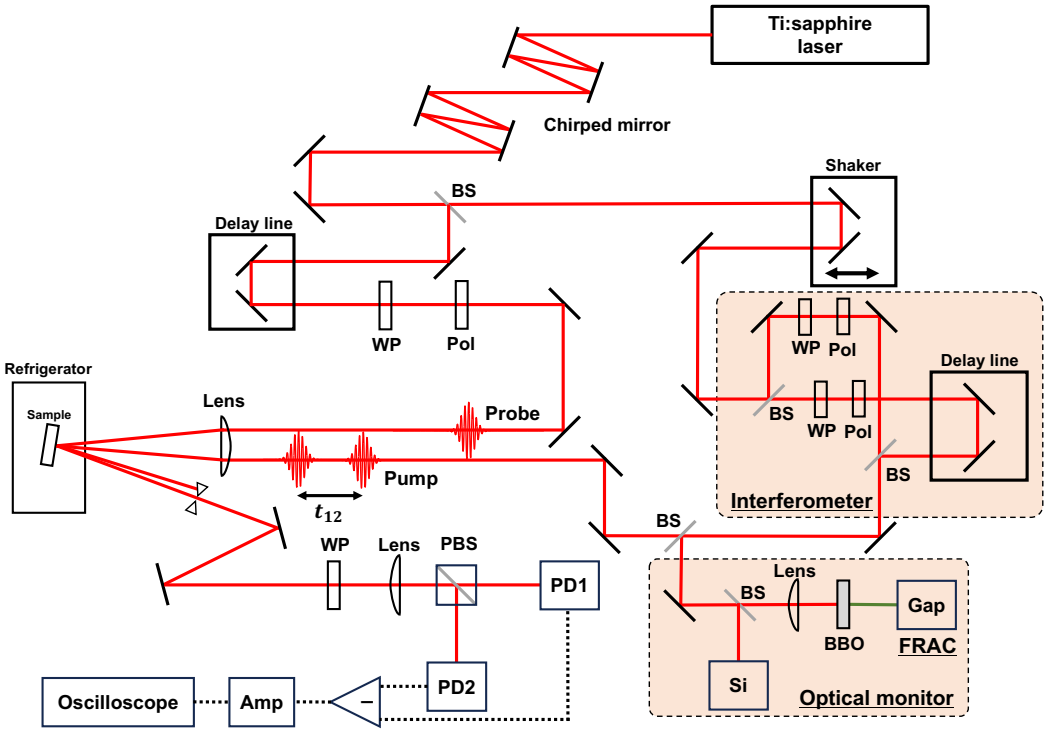

Figure 3.1: Optical system for quantum path interferometry. BS: beam splitter, WP: waveplate, Pol: linear polarizer, PBS: polarizing beam splitter, PD: photodetector.

tem. With this system, interference between pump pulses is also observed simultaneously during transient reflectance measurements.

Applying the electro-optic (EO) sampling technique, photodetectors are used to measure the photocurrent of the reflected probe pulse. In this technique, a polarizing beam splitter separates the reflected probe pulse into a pair of beams, which are subsequently detected using twin balanced photodetectors. The differential signal detected in balanced photodetectors is amplified using a low-noise current amplifier and recorded using a digital oscilloscope. The signals are averaged 4000 times using an oscilloscope to remove electrical noise.

In this experiment, we set the relative polarized angle of the double-pump pulses to $\pi/4$. The pump pulse pairs were polarized in the crystal orientations [-110] and [010], respectively (Fig. 3.2(a)), with both intensities set to 10 mW. In addition, the probe pulse is polarized in the [100]

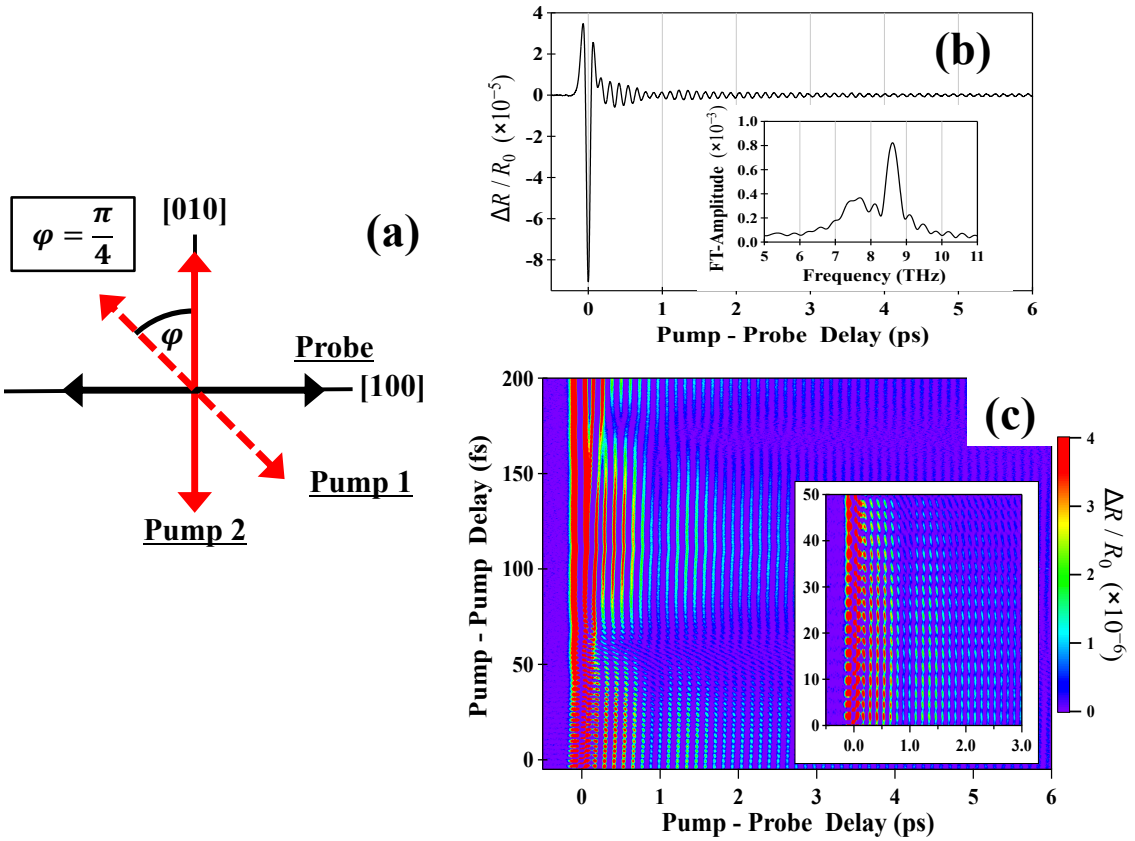

Figure 3.2: Quantum path interferometry experiment on the n-GaAs (001) surface. (a) The relation between the electric polarization of pump 1, pump 2, and probe pulse and the crystal orientation ([100] and [010]). The red dotted and solid lines show the electric polarization of pump 1 and pump 2, respectively. The black solid line shows the electric polarization of the probe pulse. φ is the angle between the polarization of pumps 1 and 2, set to $\pi/4$. (b) Pump-probe delay dependence of the relative change in transient reflectivity ($\Delta R/R_0$) in double-pulse excitation at pump-pump delay time (t_{12}) of approximately 0 fs under 290 K. (c) Two-dimensional image map of the change in transient reflectance intensity with pump-probe delay and pump-pump delay, under the $\pi/4$ relative polarized pump pulse condition, at 290 K. This original figure is Ref. [1], and is plotted with modifications.

direction (Fig. 3.2(a)), with an intensity of 5 mW. To measure temperature dependence, three cryostat settings are used at 290 K, 90 K, and 10 K.

3.3 Ultrafast quantum path interferometry results

Fig. 3.2(b) shows the transient reflectance ($\Delta R/R_0$) obtained by double-pump pulse excitation ($t_{12} \approx 0$ fs) of n-GaAs sample as a function of

pump-probe delay at 290 K with the light intensity of about 30 mW. A non-oscillation background signal was removed. After Fourier transformation with pump-probe delays ranging from 0.3 to 3.0 ps, the Fourier-transformed (FT) signals are approximately 7.6 THz and 8.6 THz. These correspond to oscillations of the longitudinal optical phonon-plasmon couple (LOPC), and LO phonon mode [12, 16, 33–35], where the LOPC mode is smaller than that of the LO phonons. The ratio of the LO and LOPC peaks in the Fourier spectrum depends on the range of the Fourier transform and results from the much shorter lifetime of the LOPC mode compared to the LO phonons. Therefore, we focus only on the LO phonon in this study.

Fig. 3.2(c) shows two-dimensional image maps of the relative change in transient reflection ($\Delta R/R_0$) against pump-probe delay (t_{13}) and pump-pump delay (t_{12}). We vary t_{12} in steps of 300 attoseconds and measure the transient reflectance of each pump-pump delay. At a delay time t_{12} between pump pulses, we observe two types of oscillations: 1) slow oscillation with a period of approximately 115 fs, corresponding to the LO phonon of GaAs, and; 2) rapid oscillation with a period of approximately 2.7 fs.

To see greater detail of the interference behavior at a pump-pump delay time of (t_{12}), Fourier transforms are performed for all pump-pump data along with the pump-probe delay (e.g., horizontal axis in Fig. 3.2(c)). Subsequently, we plot the 8.6 THz signal corresponding to the LO phonon signal versus the pump-pump delay time. Fig. 3.3(a) shows rapid oscillation via electronic coherence simultaneously with slow interference fringes due to phononic interference. Moreover, electronic coherence is confirmed to persist for a longer time than optical interference. The splitting width of the electronic interference is 15.9 $\pm$ 0.3 fs. We observe a less pronounced amplitude suppression in the interference shape near the pump-pump delay

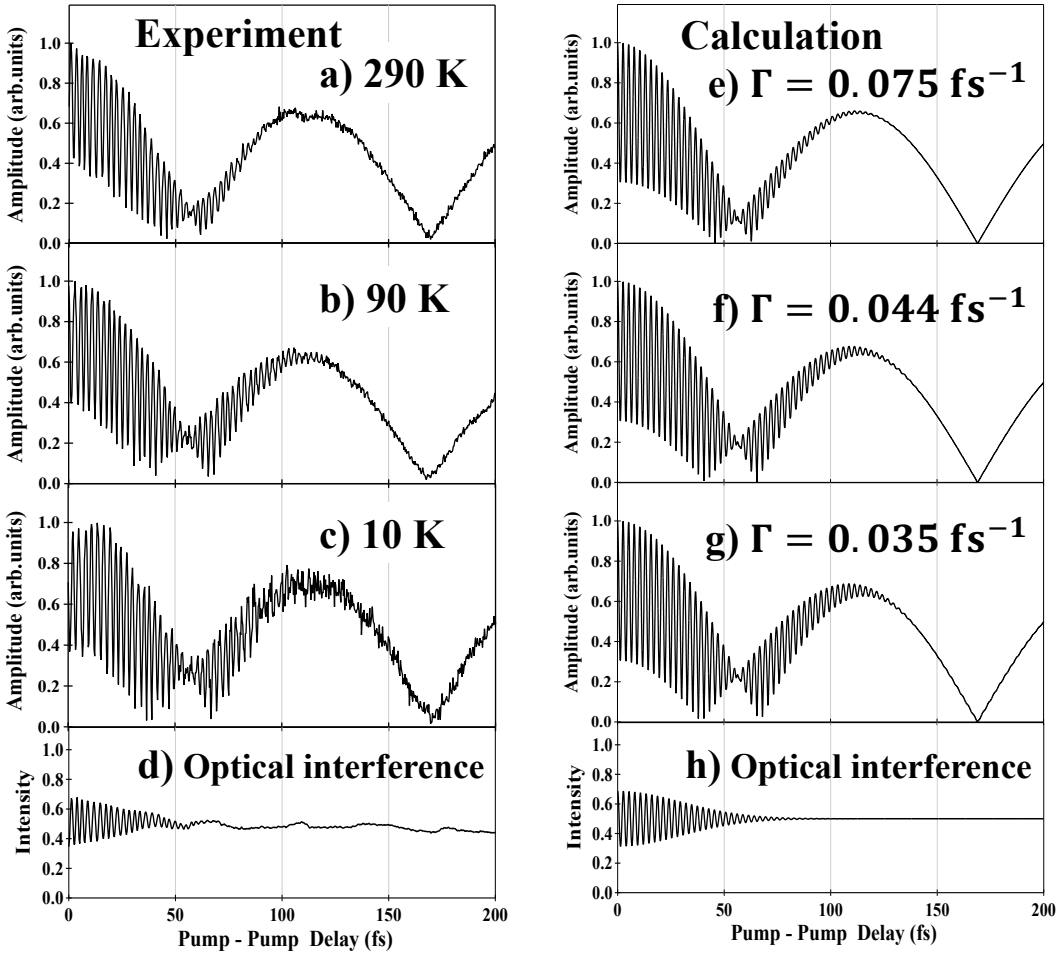

Figure 3.3: Quantum path interference as a function of pump–pump delay t_{12}. (a)-(d) Measured LO phonon amplitudes as a function of pump-pump delay time t_{12} at (a) 290 K, (b) 90 K, (c) 10 K, and (d) optical interference of pump pulses. (e)-(h) The calculated LO phonon amplitudes as a function of pump-pump delay time at a relative polarization angle of $\pi/4$ for the parameter Γ: (e) 0.075 fs^{-1}, (f) 0.044 fs^{-1}, (g) 0.035 fs^{-1}, and (h) theoretical optical interference of pump pulses. Each calculated result reflects the experimental visibility of optical interference. The vertical axis is normalized by the maximum phonon amplitude of each data in experiment and theory. This original figure is Ref. [1], and is plotted with modifications.

time $t_{12} = 0$ fs, which is different to our previously reported results under parallel polarization [30].

Fig. 3.3(a)-(c) shows the measured LO phonon amplitudes (i.e., interference of quantum coherence) as a function of pump-pump delay time t_{12} at 290 K, 90 K, and 10 K conditions. The electronic decoherence time increases at lower temperatures. By focusing on the quantum coherence's

interference shape at a pump-pump delay time around $t_{12} = 55$ fs, a significant triangle pattern (due to uplifting of the phonon amplitude and splitting of the interference shape) is observed with decreasing temperature. This uplifting of phonon amplitude is a characteristic phenomenon caused by quantum path interference in the impulsive stimulated Raman scattering (ISRS) process [30]. Notably, this splitting width is seen to expand as the temperature decreases, with the splitting widths of the electronic interference at 10 and 90 K obtained to be 27.4 and 24.6 $\pm$ 0.3 fs, respectively. Note that we define splitting value as the width of the triangles observed in the quantum interference shape when the pump-pump delay t_{12} is around 55-fs. Furthermore, we define the experimental and theoretical uplifting value as the height from the minimum phonon amplitude to the point where the electronic interference collapse-revival behavior. Details of the definition of uplifting and splitting are given in the Appendix.

3.4 Theoretical calculation with decoherence parameter

The theoretical model for the coherent control of LO phonons in GaAs by double-pulse excitation is derived using the quantum mechanical model and ISRS process [32], described as follows. This model was derived using a simplified electronic band model, the phonon state as a harmonic oscillator, and the electron–phonon interaction taking into account the allowed and forbidden Raman scattering process [21, 36–38]. The Hamiltonian model and calculation of the density operator corresponding to the double-sided Feynman diagrams are described in detail elsewhere [32], and in the Chapter 2. In this model, the resonant excitation occurs at an energy slightly higher than the excitation band edge of GaAs, and coherent phonons are generated. We therefore introduce a phenomenological effective response function $F(t)$ to describe the probability of electron transition

to the energy region corresponding to resonant Raman scattering. In this calculation, we use a simplified Lorenz model for the effective response function

$$\begin{aligned} F(t) &= \sum_k |\mu_k|^2 e^{-\frac{i}{\hbar}(\varepsilon_k - \varepsilon_g)t - \eta|t|/\hbar}, \quad (\eta = 0_+) \\ &\propto |\mu|^2 \exp\left(-i\Omega_c t - \Gamma|t|\right), \end{aligned} \tag{3.1}$$

where Ω_c corresponds to the center frequency of the optical pulse and Γ to the decay constant, which is the reciprocal of the electronic decoherence time.

We calculate the four quantum pathways in optical transition via ISRS with double-pump pulses. The visibility of optical interference in the experiment (Fig. 3.3(d)) is confirmed to be only approximately 75% of perfect interference (100%), so we therefore consider a contribution of 0.75 from the two quantum pathways related to electronic coherence.

Fig. 3.3(e)-(h) shows the calculated LO phonon amplitudes as a function of pump-pump delay time at a relative polarization angle of $\pi/4$ while varying the parameter Γ. In these figures, the theoretical results confirm that the experimental interference shapes are well reproduced. In particular, the splitting or uplifting of the interference shape shows a similar change as the decay constant Γ decreases, i.e., as the decoherence time increases, the feature interference pattern formed becomes more significant as in the case of the experimental lower temperature.

These results strongly suggest that the splitting and uplifting of the interference shape are dependent upon the decay constant. Moreover, it is possible to determine the decoherence time in electron–phonon composite states by comparing the theoretical and experimental splitting widths and uplifting of phonon amplitudes, whose calculations as a function of the decay constant are shown in Fig. 3.4.

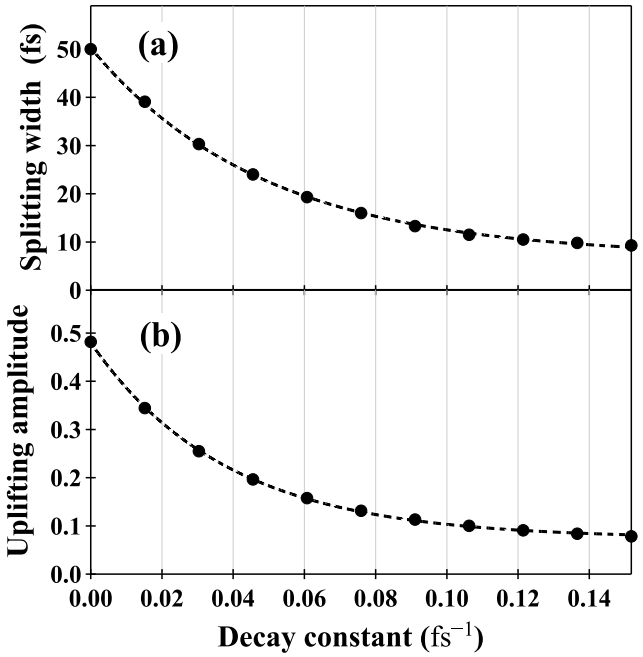

Figure 3.4: The relation among the calculated decay constant Γ, the splitting width, and the uplifting of the phonon amplitude in the interference shapes at around $t_{12} = 55$ fs; (a) Splitting width where the phonon amplitude reaches a minimum. (b) Uplifting amplitude at the moment of collapse and revival of the electronic coherence. This figure is obtained from Ref. [1].

3.5 Discussion on electronic decoherence time

Using the calculated relation between the splitting width or uplifting of phonon amplitude and the decay constant (Fig. 3.4), the electronic decoherence time at each temperature is obtained, shown in Fig. 3.5 with a plot of decoherence time as a function of temperature. Each decoherence time was determined by comparing experimental and theoretical splitting and uplifting values of triangle patterns in quantum interference shape. The electronic decoherence time is found to be 27.8 ± 0.5, 23.0 ± 0.3, and 12.9 ± 0.3 fs at each temperature of 10, 90, and 290 K, decreasing as the temperature increases, respectively.

Wegener et al [8, 9, 39, 40] have studied the influence of photoinduced carriers on electronic coherence in bulk GaAs (0.6 μm layer in GaAs/$Al_{0.3}Ga_{0.7}As$) using four-wave mixing (FWM) and photon-echo

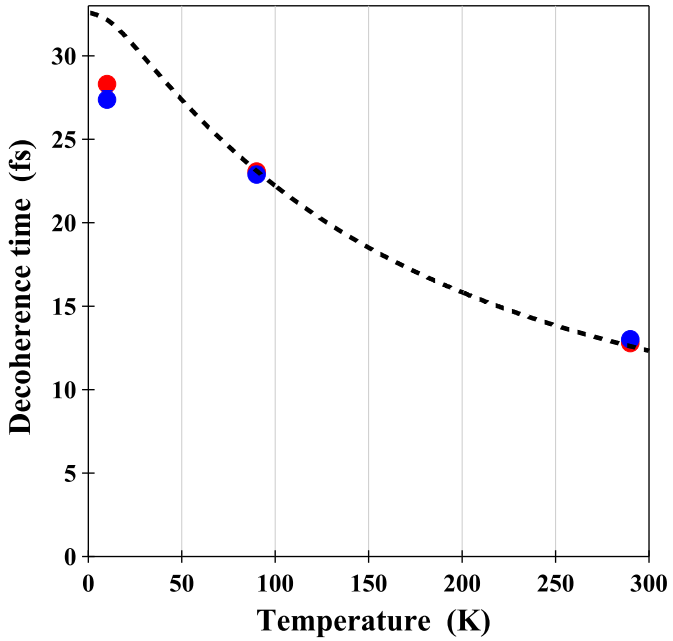

Figure 3.5: The decoherence time as a function of temperature. The red and blue dotted lines show experimental decoherence times obtained by uplifting of phonon amplitude and splitting width, respectively. The black dashed line is the relation between the electronic decoherence time and temperature estimated by the quantum kinetic theory (Eq. (3.3)). This figure is obtained from Ref. [1].

techniques at room temperature. They report that the electronic decoherence time (τ) is 18 fs at a carrier density of 10^{17} cm^{-3}, and is dependent on the photoexcited carrier density n_e as

$$\tau^{-1} = \tau_0^{-1} + c\, n_e^{1/3}, \tag{3.2}$$

where n_e is the sum of the two individual photoexcited carrier densities ($n_e = n_{e1} + n_{e2}$), and τ_0 is the decay constant for scattering by phonons, and $\tau_0 = 100$ fs. The coefficient c can be estimated from Fig. 1 in Ref. [8] to be 9×10^7 cm/s.

In this study, two types of carriers may contribute to electronic coherence. One is the photoinduced carriers under irradiation by double-pump pulses, while the other is the carrier density from Si dopants. It is necessary to consider the contribution of both carrier densities to the theoretical

model in Eq. (3.2).

In Eq. (3.2), the parameter τ_0 is the decay constant for scattering by phonons, and c is the coefficient. Here, we consider the meaning of parameter c. Examination of the unit dimension of Eq. (3.2) shows that the first terms on the left and right sides are in 1/s. For the second term on the right side, $n_e^{1/3}$ has a unit in cm^{-1}. We infer the dimension of c to be cm/s and interpret it as akin to the group velocity of electrons. Calculating the group velocity of electrons excited by the optical pulse (1.55 eV) using the free electron model ($E = \hbar^2 k^2/2m_n + E_c$) at 300 K gives an estimated group velocity of about 8.4×10^7 cm/s.

Subsequently, we attempt to evaluate the decoherence time due to the photoinduced and dopant carrier densities by using the modified quantum kinetic theory in Eq. (3.2), as

$$\tau^{-1} = \tau_0^{-1} + v(T)\,(n_d(T) + n_e(T))^{1/3}. \tag{3.3}$$

where $\tau_0 = 100$ fs, and $v(T)$ is the group velocity of electrons, $n_d(T)$ is the dopant carrier density. $n_e(T)$ is the photoinduced carrier density with double-pump pulses, which was derived using the pulse power at maximum interference. Details of each carrier density are given in the Appendix. The estimated decoherence time with respect to temperature is shown in Fig. 3.5, in which the estimated values are shown to agree well with the experimental results. Equation (3.3) can be easily interpreted as follows. $(n_d(T) + n_e(T))^{1/3}$ corresponds to the reciprocal of the mean distance between electrons in the conduction band. $v(T)$ corresponds to the group velocity of the photoinduced electron in the conduction band. Consequently, $v(T) \times (n_d(T) + n_e(T))^{1/3}$ corresponds to the reciprocal of the collision time. Therefore, the decoherence time can be determined by the collision time for the photoexcited electrons in the conduction band

in the present condition. The experimentally obtained decoherence time at 10 K is shorter than the estimated values, and there are two possible explanations for this. One is that the free electron model may not explain the parameter value of $v(T)$ at extremely low temperatures, because the band structure and effective mass change with temperature. Alternatively, τ_0 may depend on temperature because the lifetime caused by phonon scattering, such as electron–phonon scattering, varies with temperature. In actuality, the estimated decoherence time becomes lower and more consistent with the experimental decoherence time at 10 K when τ_0 is set to a time shorter than 100 fs. In addition, excitons are generated by electrons at the conduction band edge as the temperature decreases. Consequently, the carrier density is expected to decrease, and the electronic decoherence time should increase beyond the estimated time in this calculation. However, our experimental result shows a shorter decoherence time at 10 K. This may be due to the fact that our observations concern electronic coherence at energies beyond the band edge, which are relatively less affected by exciton generation. Further experiments with various pump power densities, center wavelengths, and temperatures will help to further elucidate the details of the decoherence mechanism.

3.6 Summary

We investigate the electronic decoherence time in the electron–phonon composite system (n-GaAs) using ultrafast quantum path interferometry experiments with relative-phase locked and $\pi/4$-polarized double-pulse excitation. The decoherence time is quantitatively determined from the uplifting of phonon amplitude, and the split width is obtained with the help of a quantum mechanical model calculation: 27.8 ± 0.5, 23.0 ± 0.3, and 12.9 ± 0.3 fs at 10, 90, and 290 K. The temperature dependence of the

decoherence time is discussed from the perspective of electron density, and is reproduced using carrier densities in the conduction band, and the group velocity of the photoinduced electrons. The derived formulas with electronic dispersion, photon energy, and intensity will be expected to evaluate the electronic decoherence time in solids. We also anticipate that the ultrafast quantum path interferometry will be used to examine quantitatively electronic and phononic decoherence times in solids.

Appendix A: Uplifting and splitting of a quantum path interference

In this chapter, we measured the electronic coherence using relative phase-locked double pump pulses. We also determined the electronic decoherence time at different temperatures. In particular, we focused on the distinctive quantum-path interference shape under the $\pi/4$ relative polarization. This interference shape is a triangular pattern observed at a pump-pump delay time of about 60 fs. To support the main point, we present a supplementary figure showing the uplifting and splitting of the quantum interference shape, as indicated in the main text. In addition, we provide evidence for a good agreement between our experimental data and theoretical calculation as a consequence of our analytical approach.

Figure A 3.1 shows the definition of uplift and splitting of the quantum path interference under the $\pi/4$ relative polarization. We define the splitting value as the width of the triangles (in red arrows) observed in the quantum interference shape when the pump-pump delay t_{12} is about 60 fs. Furthermore, we define the experimental and theoretical uplift value as the height from the minimum phonon amplitude to the point where the electronic interference collapse-revival behavior (in blue arrow).

Figure A 3.2 shows the comparison of the experimental data at 90 K

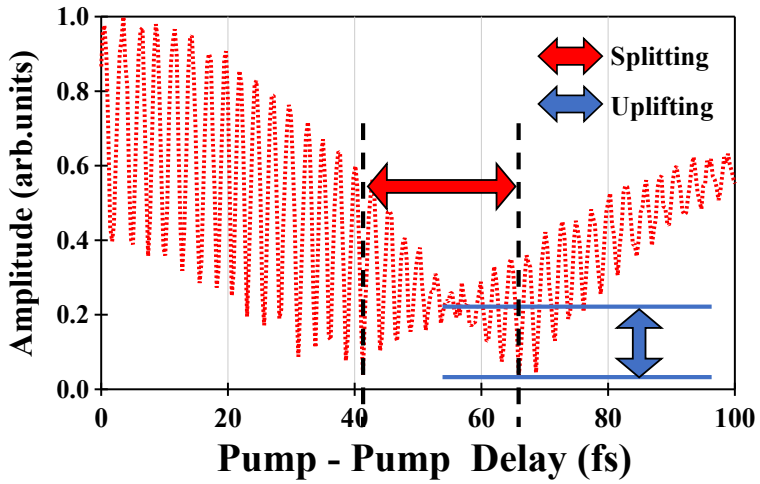

Figure A 3.1: The definition of splitting and uplifting in the quantum path interference pattern. The red and blue arrows correspond to splitting and uplifting. The red dotted line is the experimentally measured quantum path interference pattern at 90 K. This figure is obtained from supplementary materials in Ref. [1].

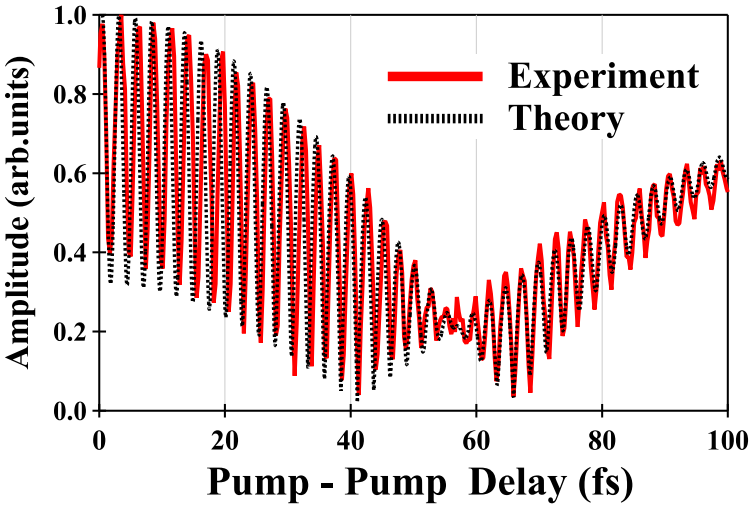

Figure A 3.2: Comparison of experimental and theoretical quantum interference at 90 K as a function of pump-pump delay in the form of matching phonon amplitude minima. The red curve and blue dotted are correspond to the experimental and theoretical results, respectively. This figure is obtained from supplementary materials in Ref. [1].

by using a theoretical calculation ($\Gamma = 0.044$ fs^{-1}) from the quantitative analysis of the electronic decoherence time. It is found that both are fit in good agreement.

Appendix B: Doped carrier density

In n-type semiconductors, the occupancy $f_d(E_d)$ in the donor level at temperature T is

$$f_d(E_d) = \frac{1}{1 + \frac{1}{g}\exp[(E_d - E_F)/k_B T]}, \tag{B.3.1}$$

where E_d and E_F are energies of the donor level and Fermi level, g is the degeneracy factor, and k_B is Boltzmann's constant [41]. The number of electrons (n_d) occupied in the donor level is $n_d = N_D f_d(E_d)$ for the dopant density of N_D. Then, the number of electrons (n') excited to the conduction band from dopants is $n' = N_D - n_d$.

The electron density (n) in the conduction band is

$$n = N_c \exp[-(E_c - E_F)/k_B T], \tag{B.3.2}$$

where N_c is the effective density state defined by

$$N_c(T) = 2\left(\frac{2\pi m_n k_B T}{h^2}\right)^{3/2}. \tag{B.3.3}$$

Here, m_n is the effective mass of electrons. When the bandgap energy ($E_c - E_v$) is larger than the thermal energy, the electron density in the conduction band is equivalent to n' (i.e., the charge neutrality condition):

$$N_c \exp[-(E_c - E_F)/k_B T] = \frac{N_D}{1 + g\exp[-(E_d - E_F)/k_B T]}. \tag{B.3.4}$$

Thus the Fermi energy E_F is obtained as

$$E_F = E_d + k_B T \log\left[-\frac{1}{2g} + \frac{1}{2g}\sqrt{1 + \frac{4gN_D}{N_c}\exp\left(\frac{E_c - E_d}{k_B T}\right)}\right]. \tag{B.3.5}$$

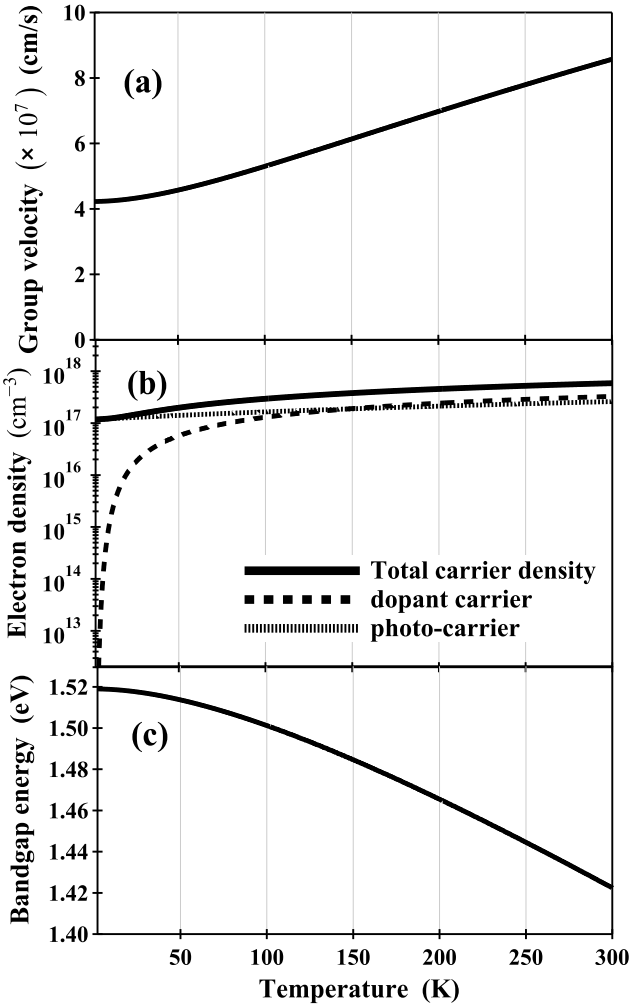

Figure B 3.1: (a) The group velocity, (b) electron density, and (c) bandgap energy versus temperature in n-GaAs. (b) The solid, dashed, and dotted curves are total carrier density, dopant carrier, and photoinduced carrier, respectively. The vertical axis in (b) is plotted as a logarithm with base 10. This figure is obtained from supplementary materials in Ref. [1].

Using the Fermi energy, the carrier density in the conduction band is calculated.

In this study, we used Si-doped GaAs with a concentration of $N_D = 10^{18}$ cm^{-3}, and a degeneracy factor of $g = 2$. The energy of the conduction band edge (E_c) is defined as the band gap energy (E_g), assuming that the top of the valence band (E_v) is 0 eV. The bandgap energy is determined as a function of temperature, $E_g(T) = 1.519 - 5.408 \times 10^{-4}\, T^2/(T + 204)$

[42]. Furthermore, the bandgap energy is approximately 1.42 eV, which is larger than the thermal energy ($\sim$ 26 meV) at 300 K. The ionization energy for Si in GaAs is 0.0059 eV [41]. Figure B 3.1 shows the calculated group velocity, electron density, and bandgap energy as a function of temperature.

Appendix C: Laser intensity and photocarriers

The laser focused spot is approximated as Gaussian function, $\sqrt{\frac{2}{\pi\sigma^2}}\exp(-2r^2/\sigma^2)$, in which σ is the radius of the beam at $1/e^2$ times of the maximum intensity. The intensity profile along one axis is measured using a knife-edge method, and r_{HWHM} is determined to be about 25 μm. The power density is estimated to be 86% of the power irradiated onto the focused area ($S = \pi\sigma^2,\ \sigma = \sqrt{2}r_{\mathrm{HWHM}}/\sqrt{\ln 2}$). The reflection coefficient used is $R = 0.39$ [43]. The absorption coefficient at photon energy of 1.55 eV is determined as a function of temperature, as $\alpha(T) = 36.7\,T + 9.0 \times 10^3\ (\mathrm{cm}^{-1})$. This is because it has been reported to show slight fluctuations with temperature [44].

In this experiment, the optical pulse travels through the quartz glass mounted in the cryostat, so the optical power irradiated onto the sample is multiplied by the transmittance (τ) of the quartz glass ($\tau = 0.95$). Before accounting for the cryostat, each pump laser power (pump 1, pump 2) is 10 mW with a repetition rate of 94 MHz and a central wavelength of 800 nm (corresponding to 1.55 eV). The maximum pump laser power is about 30 mW due to the optical interference. Consequently, the number of photons is estimated to be $I_0 = 1.29 \times 10^9$ photons/pulse. Using these parameters, the density of photoinduced electrons (n_{e}) per pulse is determined as

$$n_{\mathrm{e}}(T) = 0.86\,\alpha(T)(1-R)\,\tau I_0/(\pi\sigma^2) \tag{C.3.1}$$

Here, we set the quantum efficiency of photoexcitation to be 1.

Appendix D: Estimated decoherence time for photoexcited electrons from heavy and light holes in valance bands

In this chapter, we evaluated the electron group velocity, which corresponds to the energy difference between the band gap and the photoexcitation energy by using a free electron model. In addition, we estimated the decoherence time based on quantum kinetic theory. Here, we considered the difference in valance band curvature resulting from the effective mass of the heavy and light holes [41], and analyzed the influence of the decoherence time of photo-excited electron from each hole band.

Figure D 3.1 shows the temperature dependence of the estimated decoherence times for electrons excited from each hole band. From Fig. D 3.1, it can be concluded that electrons from heavy holes undergo more efficient scattering (decoherence) than those from light holes, since electron excitation occurs on the $k > 0$ side. Furthermore, the estimated decoherence time due to electronic excitation from the heavy holes is close to the result of the electron group velocity, which corresponds to the energy difference between the band gap and the optical excitation energy as presented in the main text.

References

[1] I. Takagi, Y. Kayanuma, and K. G. Nakamura, Phys. Rev. B **107**, 184305 (2023).

[2] I. Bloch, Nature **453**, 1016 (2008).

[3] K. Bader, D. Dengler, S. Lenz, B. Endeward, S.-D. Jiang, P. Neugebauer, and J. van Slageren, Nat. Commun. **5**, 5304 (2014).

[4] S. Lloyd, J. Phys.: Conf. Ser. **302**, 012037 (2011).

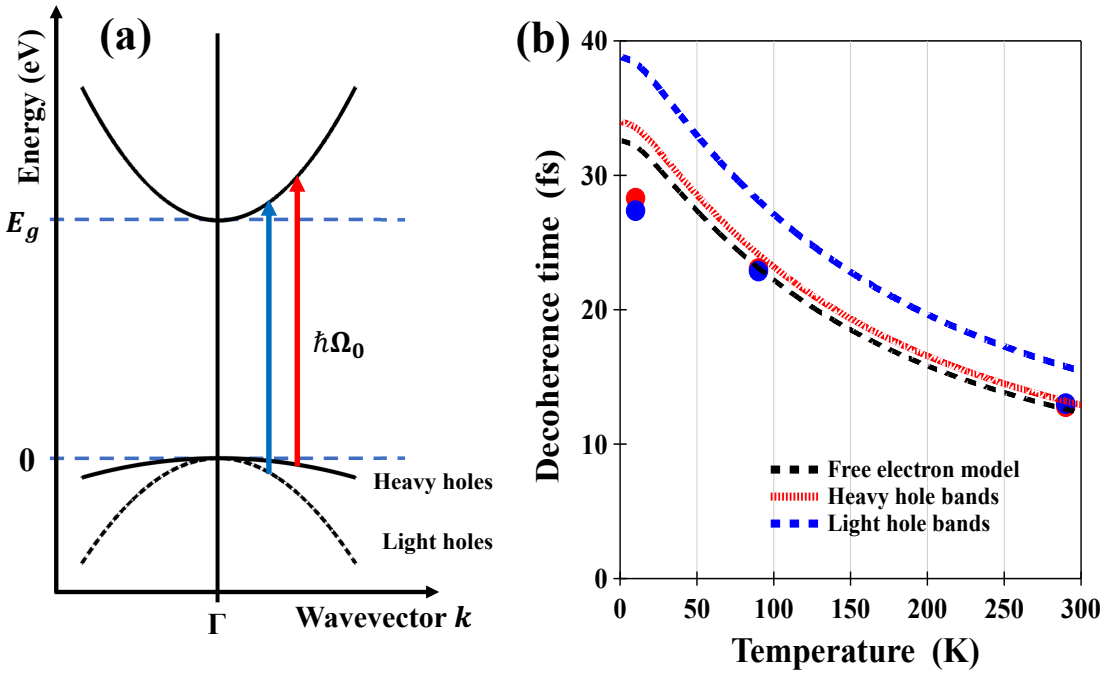

Figure D 3.1: The comparison of estimated decoherence time in the electronic excitation from the heavy and light hole bands in the valence band; (a) schematic diagram of optical excitation from each hole band. (b) estimated decoherence time as a function of temperature T. The red and blue dashed lines correspond to the estimated decoherence time in the electronic excitation from heavy and light hole bands, respectively. The black line is the estimated decoherence time on the main text. This figure is obtained from supplementary materials in Ref. [1], and is plotted with modifications.

[5] N. Lambert, Y. N. Chen, Y. C. Cheng, C. M. Li, G. Y. Chen, and F. Nori, Nat. Phys. **9**, 10 (2013).

[6] W. W. Chow, H. C. Schneider, and M. C. Phillips, Phys. Rev. A **68**, 053802 (2003).

[7] S. Welinski, P. J. T. Woodburn, N. Lauk, R. L. Cone, C. Simon, P. Goldner, and C. W. Thiel, Phys. Rev. Lett. **122**, 247401 (2019).

[8] W. A. Hügel, M. F. Heinrich, M. Wegener, Q. T. Vu, L. Bányai, and H. Haug, Phys. Rev. Lett. **83**, 3313 (1999).

[9] M. Wegener, J. Lumin. **87-89**, 20 (2000).

[10] M. U. Wehner, M. H. Ulm, D. S. Chemla, and M. Wegener, Phys. Rev. Lett. **80**, 1992 (1998).

[11] Y.-X. Yan, E. B. Gamble, and K. A. Nelson, J. Chem. Phys. **83**, 5391 (1985).

[12] G. C. Cho, W. Kütt, and H. Kurz, Phys. Rev. Lett. **65**, 764 (1990).

[13] H. J. Zeiger, J. Vidal, T. K. Cheng, E. P. Ippen, G. Dresselhaus, and M. S. Dresselhaus, Phys. Rev. B **45**, 768 (1992).

[14] A. V. Kuznetsov and C. J. Stanton, Phys. Rev. Lett. **73**, 3243 (1994).

[15] R. Merlin, Solid State Commun **102**, 207 (1997).

[16] T. Dekorsy, G. C. Cho, and H. Kurz, "Coherent phonons in condensed media", in *Light scattering in solids viii: fullerenes, semiconductor surfaces, coherent phonons*, edited by M. Cardona and G. Güntherodt (Springer Berlin Heidelberg, Berlin, Heidelberg, 2000), pp. 169–209.

[17] K. Sokolowski-Tinten, C. Blome, J. Blums, A. Cavalleri, C. Dietrich, A. Tarasevitch, I. Uschmann, E. Förster, M. Kammler, M. Horn-von-Hoegen, and D. von der Linde, Nature **422**, 287 (2003).

[18] S. L. Johnson, P. Beaud, C. J. Milne, F. S. Krasniqi, E. S. Zijlstra, M. E. Garcia, M. Kaiser, D. Grolimund, R. Abela, and G. Ingold, Phys. Rev. Lett. **100**, 155501 (2008).

[19] R. P. Chatelain, V. R. Morrison, B. L. M. Klarenaar, and B. J. Siwick, Phys. Rev. Lett. **113**, 235502 (2014).

[20] T. Dekorsy, T. Pfeifer, W. Kütt, and H. Kurz, Phys. Rev. B **47**, 3842 (1993).

[21] T. Pfeifer, T. Dekorsy, W. Kütt, and H. Kurz, Appl. Phys. A **55**, 482 (1992).

[22] D. J. Tannor and S. A. Rice, J. Chem. Phys. **83**, 5013 (1985).

[23] P. Brumer and M. Shapiro, Chem. Phys. Letters **126**, 541 (1986).

[24] D. J. Tannor, R. Kosloff, and S. A. Rice, J. Chem. Phys. **85**, 5805 (1986).

[25] H. Katsuki, N. Takei, C. Sommer, and K. Ohmori, Acc. Chem. Res. **51**, 1174 (2018).

[26] H. Mashiko, Y. Chisuga, I. Katayama, K. Oguri, H. Masuda, J. Takeda, and H. Gotoh, Nat. Commun. **9**, 1468 (2018).

[27] T. Kimata, K. Yoda, H. Matsumoto, H. Tanabe, F. Minami, Y. Kayanuma, and K. G. Nakamura, Phys. Rev. B **101**, 174301 (2020).

[28] I. Takagi, T. Kato, Y. Kayanuma, and K. G. Nakamura, Solid State Commun **350**, 114747 (2022).

[29] S. Hayashi, K. Kato, K. Norimatsu, M. Hada, Y. Kayanuma, and K. Nakamura, Sci. Rep **4**, 4456 (2014).

[30] K. G. Nakamura, K. Yokota, Y. Okuda, R. Kase, T. Kitashima, Y. Mishima, Y. Shikano, and Y. Kayanuma, Phys. Rev. B **99**, 180301 (R) (2019).

[31] H. Matsumoto, T. Kitashima, T. Maruhashi, I. Takagi, Y. Kayanuma, and K. G. Nakamura, Solid State Commun **327**, 114215 (2021).

[32] I. Takagi, Y. Kayanuma, and K. G. Nakamura, Phys. Rev. B **104**, 134301 (2021).

[33] A. Mooradian and A. L. McWhorter, Phys. Rev. Lett. **19**, 849 (1967).

[34] J. D. Lee and M. Hase, Phys. Rev. Lett. **101**, 235501 (2008).

[35] J. Hu, O. V. Misochko, A. Goto, and K. G. Nakamura, Phys. Rev. B **86**, 235145 (2012).

[36] K. Ishioka, A. K. Basak, and H. Petek, Phys. Rev. B **84**, 235202 (2011).

[37] C. Trallero-Giner, A. Cantarero, and M. Cardona, Phys. Rev. B **40**, 4030 (1989).

[38] P. Y. Yu and M. Cardona, *Fundamentals of semiconductors: physics and materials properties*, 3rd ed. (Springer Berlin, 2001).

[39] H. Haug and A. P. Jauho, *Quantum kinetics in transport and optics of semiconductors*, Springer Series in Solid-State Sciences (Springer Berlin Heidelberg, 2008).

[40] W. Schäfer and M. Wegener, *Semiconductor optics and transport phenomena*, Advanced Texts in Physics (Springer, 2002).

[41] S. M. Sze, Y. Li, and K. K. Ng, *Physics of semiconductor devices* (Wiley, 2021).

[42] J. S. Blakemore, J. Appl. Phys. **53**, R123 (1982).

[43] E. Vigil, J. A. Rodríguez, and R. P. Alvarez, Phys. Status Solidi (b) **90**, 409 (1978).

[44] M. D. Sturge, Phys. Rev. **127**, 768 (1962).

Chapter 4
Influence of initial phonon states on the generation of coherent optical phonons

In this chapter, we explore whether the initial state of the system due to temperature conditions affects the quantum path interference results. We define a mixed state as the system's initial state, taking into account the phonon distribution determined by the thermal equilibrium distribution, and investigate the generation of coherent phonons under finite temperatures. This work is published in Solid State Communications [1].

4.1 Introduction

Coherent phonon oscillations are a common phenomenon observed in many ultrafast pump-probe experiments, including those with electron, optical, and X-ray probe pulses [2–11]. The ultrafast dynamics of optical phonons, including their lifetimes and frequency chirping, have been studied using coherent phonons in various materials [12–19].

There are two main mechanisms behind the generation of coherent optical phonons depending on the transition of the optical pulse: impulsive stimulated Raman scattering (ISRS) [2, 8, 12] under transparent conditions and impulsive absorption (IA) under opaque conditions, where the products of the latter are often called displacive excitation of coherent phonons (DECP) [6, 12, 20]. These two mechanisms have usually been treated separately in theoretical calculations. We have previously developed a theory that treats both the ISRS and IA mechanisms using a simple quantum

mechanical model. The material system is modeled using two electronic levels. Shifted harmonic oscillators are assumed for the optical phonons and a dipole interaction between the system and light (a classical optical field). The time evolution of the coherent optical phonons is calculated by solving the quantum Liouville or time-dependent Schrödinger equation with second-order perturbations. The results replicate experimental observations well [18, 21, 22].

In previous work [21, 23–25], the initial phonon state was assumed to be a zero-phonon state, which is a reasonable assumption for high-frequency phonons and low-temperature conditions. However, under some experimental conditions, non-zero number states might contribute to the coherent phonons. For example, the population ratio $P_{n=1}/P_{n=0}$ is approximately 0.49 for optical phonons of the Cu-mode in $\mathrm{YBa_2Cu_3O_{7-\delta}}$ (4.5 THz) at room temperature (300 K). It is therefore important to study the effect of the initial phonon distribution on the dynamics of coherent optical phonons.

In this chapter, we study the influence of the initial distribution of phonon states on the generation of coherent optical phonons. We solve the quantum Liouville equation using two electronic states and phonon basis sets for the initial phonon states, expressed using a density matrix as a mixed state under thermal equilibrium conditions.

4.2 Model with initial phonon states

We consider a two-level electronic system and a harmonic oscillator for the optical phonons at the Γ-point ($\vec{k} = 0$). It is assumed that the electronic excited state is coupled with the optical phonon mode through a deformation-potential interaction with a dimensionless coupling constant ($\alpha > 0$). We approximate the interactions by neglecting the $\overrightarrow{k}$-

dependence of the coupling constant. In a bulk crystal, the Huang-Rhys factor (α^2) is considered to be small, i.e., $\alpha^2 \ll 1$. In the present model, the physical properties specific to the materials (e.g., phase transitions in superconductivity) are not taken into account.

The Hamiltonian of the electron-phonon composite states is given by

$$H_0 = H_{\mathrm{e}} + H_{\mathrm{ph}} + H_{\mathrm{ep}}, \tag{4.1}$$

$$H_{\mathrm{e}} = \varepsilon_g \left|g\right\rangle \left\langle g\right| + \varepsilon_e \left|e\right\rangle \left\langle e\right|, \tag{4.2}$$

$$H_{\mathrm{ph}} = \hbar\omega b^\dagger b, \tag{4.3}$$

$$H_{\mathrm{ep}} = \alpha\hbar\omega \left(b^\dagger + b\right) \left|e\right\rangle \left\langle e\right|, \tag{4.4}$$

where H_{e} and H_{ph} are the Hamiltonians of the electronic and phonon states, respectively. H_{ep} is the Hamiltonian of the electron-phonon interaction. The parameter ω is the phonon frequency, and $\varepsilon_g, \varepsilon_e$ are the energies of the ground and excited levels, respectively. The operators $b^\dagger, b$ are the creation and annihilation operators of the phonons, respectively.

Within the rotating-wave approximation, the interaction Hamiltonian between light and electrons is expressed as

$$H_I(t) = \mu E(t) \left(e^{-i\Omega_0 t} \left|e\right\rangle \left\langle g\right| + e^{i\Omega_0 t} \left|g\right\rangle \left\langle e\right|\right), \tag{4.5}$$

where μ is a transition dipole moment and Ω_0 is the frequency of the pump pulse. $E(t)$ is the optical electric field of the pump pulse, expressed as $E(t) = E_0 f(t)$. The function $f(t)$ is the Gaussian pulse envelope, which is defined as

$$f(t) = \frac{1}{\sqrt{\pi}\sigma} \exp\left(-\frac{t^2}{\sigma^2}\right), \tag{4.6}$$

where E_0 is the amplitude of the electric field and σ is the pulse width.

In our model, we use a density matrix formalism and the quantum Liou-

ville equation to calculate the time evolution of coherent optical phonons. A wavefunction $|\psi(t)\rangle$ is expanded in the composite system using basis sets of two electronic states ($|g\rangle$ and $|e\rangle$) and phonon Fock states of a harmonic oscillator ($|n\rangle$):

$$|\psi(t)\rangle = \sum_{n=0}^{N} (c_n(t)\,|g,n\rangle + d_n(t)\,|e,n\rangle), \tag{4.7}$$

where $c_n(t)$ and $d_n(t)$ are the time evolution coefficients of the n-phonon states in the electronic ground and excited states, respectively. N is the upper limit of the phonon number state. Note that $|g,n\rangle$ is the electronic ground state in the n-phonon state, i.e., $|g,n\rangle = |g\rangle \otimes |n\rangle$.

The quantum Liouville equation is expressed as

$$i\hbar\frac{d}{dt}\rho(t) = [H, \rho(t)], \tag{4.8}$$

where H is the total Hamiltonian $H = H_0 + H_I(t)$ and $\rho(t)$ is the density operator $\rho(t) = |\psi(t)\rangle\langle\psi(t)|$. Simultaneous differential equations for the coefficients $(c_n(t), d_n(t))$ were obtained by inserting Eq. 4.7 into Eq. 4.8. The time evolution of the density operator was obtained by solving the simultaneous differential equations numerically for several initial phonon distributions. We calculated the expected value of any state related to the phonon polarization or population. In the present model, both the IA and ISRS processes coexist and the contributions of both are calculated simultaneously.

The initial phonon states were determined from the thermal equilibrium distribution at temperature T:

$$\rho(-\infty) = \sum_{n=0}^{N} \frac{1}{Z} \exp\left(-\frac{n\hbar\omega}{k_B T}\right) |g,n\rangle\langle g,n|\,. \tag{4.9}$$

where k_B is the Boltzmann constant and Z is a partition function: $Z = \sum_n \exp(-n\hbar\omega/k_BT)$. The population in the electronic states was assumed to be negligibly tiny because the bandgap energy ($\varepsilon_e - \varepsilon_g$) is much larger than the thermal energy.

In the actual calculations, we considered five phonon states ($N = 4$) in each electronic state. The phase relaxation effect of electrons in the electronic excited state was not considered. We set the electron-phonon coupling constant to $\alpha = 0.01$. The band gap energy and the vibrational energy were set to $\varepsilon_e - \varepsilon_g = 1.4$ eV and $\hbar\omega = 18.6$ meV (≈ 4.5 THz), respectively. We also set the parameters $\sigma = 30$ fs and $\mu E_0 = \sqrt{0.55}$ (eV $\cdot$ fs), corresponding to a pulse energy of 7.53 $(\mu\mathrm{J/cm}^2)$. We examined the effect of an initial phonon distribution under resonant excitation conditions ($\hbar\Omega_0 = \varepsilon_e - \varepsilon_g$).

In addition to these, the effects of pulse width and detuning were examined, which showed basically the same trends as the previously reported results with the second-order perturbations, which are described in Appendices A and B.

4.3 Results and discussion of induced coherent phonons

The polarization, population, and variance of coherent optical phonons were calculated for two possible initial phonon distributions at 10 and 300 K. In this calculation, we focus on changes of phonon amplitudes, and do not consider the relative displacement of the phonon coordinate between the electronic ground and excited states.

We evaluated the phonon polarization corresponding to coherent phonons as proportional to the expectation value of the phonon position operator ($\langle Q(t)\rangle = \mathrm{Tr}[Q\rho(t)]$, $Q = \sqrt{\frac{\hbar}{2\omega}}(b + b^\dagger)$). For example, the off-diagonal element between the $n = 0$ and $n = 1$ phonon states for

the electronic ground state in the density operator was obtained using the coefficients $c_0(t)c_1^*(t) + c_1(t)c_0^*(t)$. In contrast, the electronic excited state was obtained as $d_0(t)d_1^*(t) + d_1(t)d_0^*(t)$. Hereinafter, the phonon coherence between the $n-$ and $m-$phonon states in the electronic ground and excited states is denoted by $L_g(n,m) = c_n(t)c_m^*(t) + c_m(t)c_n^*(t)$ and $L_e(n,m) = d_n(t)d_m^*(t) + d_m(t)d_n^*(t)$, respectively. Furthermore, the phonon polarization in the electronic ground and excited states are denoted by $Q_g(n,m) = \sqrt{m}\ L_g(n,m)$ and $Q_e(n,m) = \sqrt{m}\ L_e(n,m)$. Note that the phonon polarization $\langle Q \rangle$ is the sum of the polarization in each electronic state, $\langle Q \rangle = \sqrt{\frac{\hbar}{2\omega}}(Q_g + Q_e) = \sqrt{\frac{\hbar}{2\omega}}\Sigma_n(Q_g(n,n+1) + Q_e(n,n+1))$.

4.3.1 Phonon polarization and population

Low temperature case ($T = 10\mathrm{K}$)

Figure 4.1 shows the calculated time evolution of the phonon polarization for an initial phonon distribution at $T = 10$ K. The initial distribution is almost dominated by zero-phonon states in the electronic ground state ($\rho(-\infty) \fallingdotseq |g,0\rangle \langle g,0|$) at 10 K.

Figure 4.1(a) shows the time evolution of the phonon polarization $Q_e(0,1)$ in the electronic excited state induced via IA and that of $Q_g(0,1)$ in the electronic ground state induced via ISRS. The intensity of $Q_e(0,1)$ increases as the pump-pulse intensity increases and begins to oscillate. Only the first oscillation peak (near $t = 0$) is smaller than the subsequent oscillation intensities (at $t > 110$ fs). The intensity of $Q_g(0,1)$ shows an oscillation with a slight delay compared with that of $Q_e(0,1)$. It is clear that the oscillation of $Q_e(0,1)$ is cosine-like and that of $Q_g(0,1)$ is sine-like, and the initial phases are different by $\pi/2$. These features agree well with experimental results and second-order perturbation theory

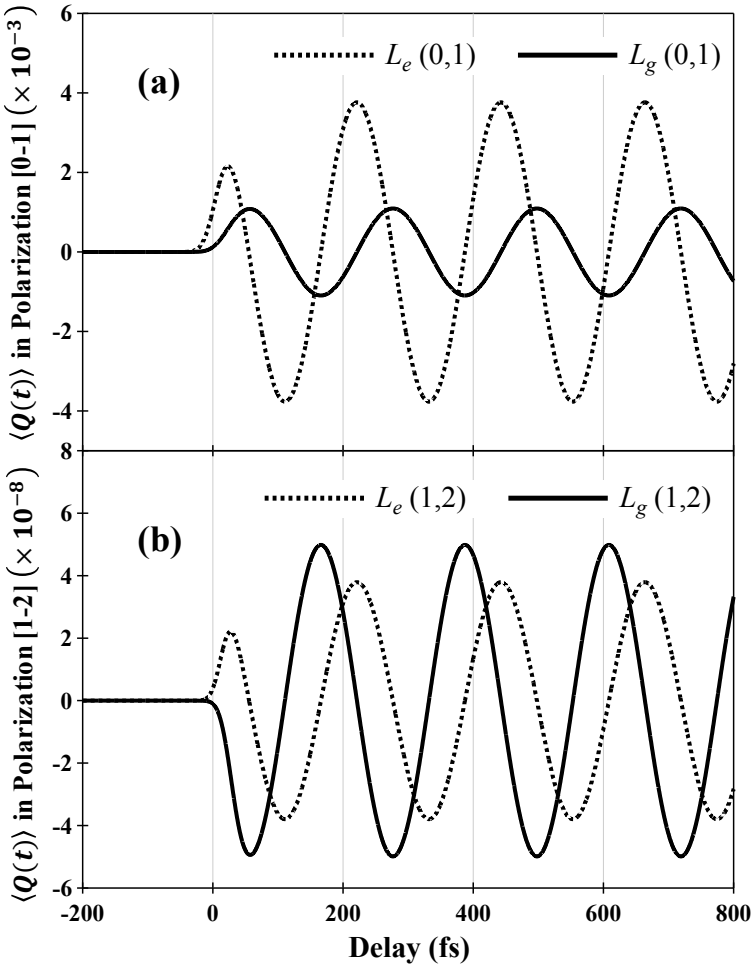

Figure 4.1: The phonon polarization in the electronic ground state (solid curves) and excited state (dotted curves) as a function of time delay for an initial state at the low-temperature limit (10 K, $\rho(-\infty) \fallingdotseq |g,0\rangle \langle g,0|$). (a) polarization between $n = 0$ and $n = 1$ states: $L_e(0,1)$ and $L_g(0,1)$, and (b) polarization between $n = 1$ and $n = 2$ states: $L_e(1,2)$ and $L_g(1,2)$. This figure is obtained from Ref. [1].

calculations [11, 23, 26].

Figure 4.1(b) shows the calculated phonon polarizations between higher-order number states ($Q_e(1,2)$ and $Q_g(1,2)$), which were not calculated using second-order perturbation theory. The amplitude of the phonon polarization between the one- and two-phonon states is 10^5 times smaller than that between the zero- and one-phonon states. The first peak position shows a shift (approximately 25 fs) compared with that of $Q_e(0,1)$. The phase of the $Q_g(1,2)$ oscillation is π different from that of the $Q_g(0,1)$ oscillation, while the $Q_e(1,2)$ and $Q_e(0,1)$ oscillations are in phase.

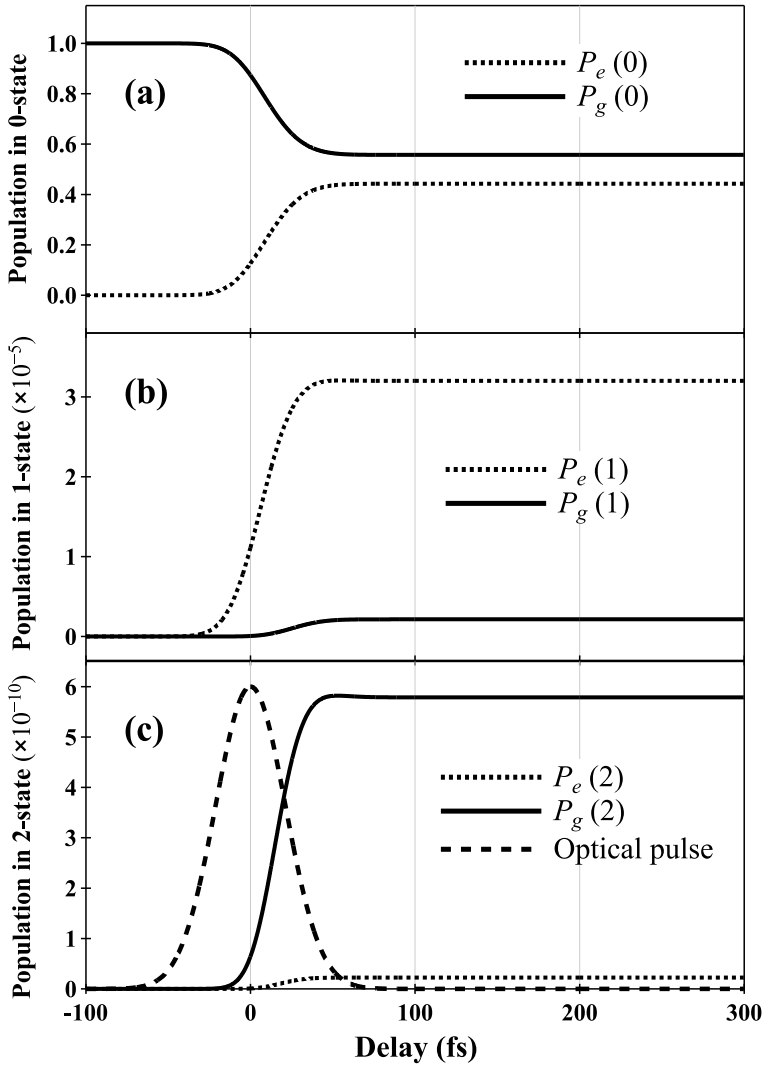

Figure 4.2: The phonon population in each phonon number state in the electronic ground state (solid curves) and excited state (dotted curves) as a function of time delay for the initial state $\rho(-\infty) \fallingdotseq |g,0\rangle\langle g,0|$. The optical pulse used in the calculation is superimposed (red solid curve). (a) population at $n = 0$ state: $P_e(0)$ and $P_g(0)$, (b) population at $n = 1$ state: $P_e(1)$ and $P_g(1)$, and (c) population at $n = 2$ state: $P_e(2)$ and $P_g(2)$. This figure is obtained from Ref. [1].

Figure 4.2 shows the time evolution of the phonon population in the electronic ground and excited states ($P_g(n),\ P_e(n)$), where n corresponds to the phonon number state ($|n\rangle$). The increase in $P_e(0)$ corresponds approximately to the decrease in $P_g(0)$ due to photoabsorption (Fig. 4.2(a)). The populations in the phonon-excited states increase with the pump-pulse irradiation, and their values are much smaller than those of

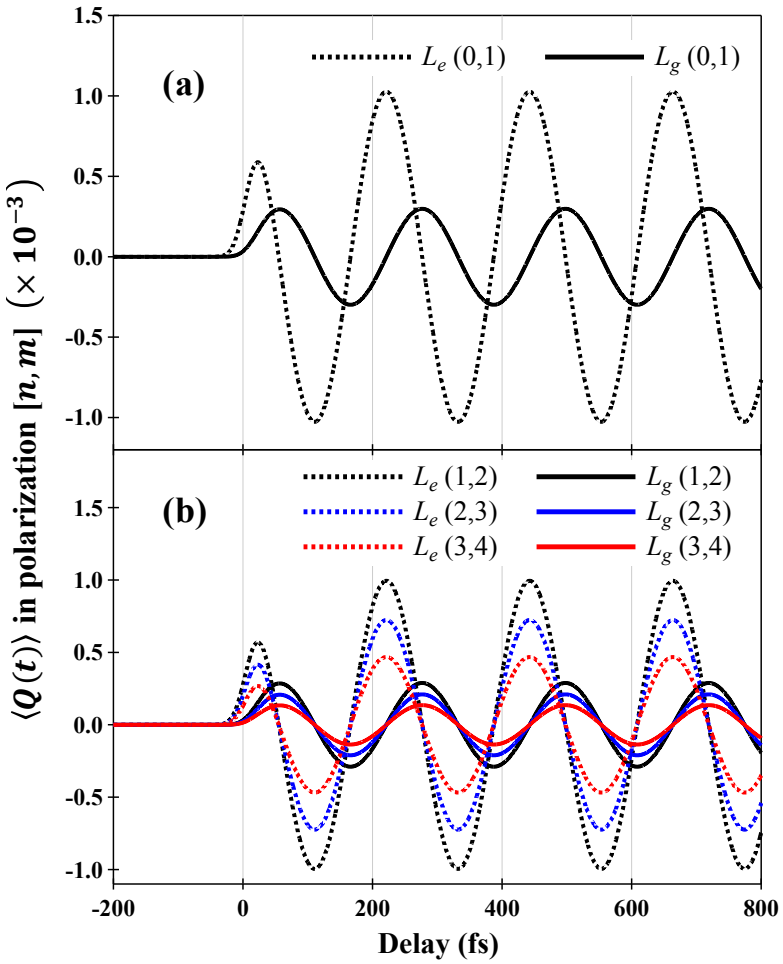

Figure 4.3: The phonon polarization in the electronic ground state (solid curves) and excited state (dotted curves) as a function of time delay for an initial state of thermal equilibrium (at 300 K). (a) polarization between $n = 0$ and $n = 1$ states: $L_e(0,1)$ and $L_g(0,1)$, and (b) polarization between higher two Fock states. This figure is obtained from Ref. [1].

the zero-phonon state. $P_e(1)$ is larger than $P_g(1)$, while $P_e(2)$ is smaller than $P_g(2)$.

All of the populations show constant values that do not oscillate, while the polarizations oscillate with the delay time. These results indicate that the coherent optical phonons correspond to the polarization.

The room temperature case ($T = 300\mathrm{K}$)

Figure 4.3 shows the time evolution of the phonon polarization for an initial phonon distribution at $T = 300$ K. The behaviors of $Q_g(0,1)$ and $Q_e(0,1)$ are almost identical to those calculated for the initial distribution at $T = 10$ K, except for the intensity of the oscillation.

The behaviors of $Q_g(1,2)$ and $Q_e(1,2)$ are also the same as those of $Q_g(0,1)$ and $Q_e(0,1)$. The oscillation intensities of $Q_e(1,2)$ and $Q_e(0,1)$ are almost the same, while the population of the one-phonon state is half of that of the zero-phonon state under the initial condition ($P_{n=1}/P_{n=0} = 0.485$). The evolution of the phonon polarization of higher phonon states shows the same behavior except for the oscillation intensity. The intensity decreases as the number of phonon states increases. Furthermore, the $Q_g(n,m)$ of the higher-order phonon states oscillate in phase.

These features of the oscillation amplitude and behavior are caused by the phonon generation process via creation and annihilation operators in phonon Fock states.

When creating phonon polarization, each phonon state ($|n\rangle$) interacts with one state above it ($|n+1\rangle$) and one state below it ($|n-1\rangle$). However, the zero-phonon state, unlike the other phonon states, cannot interact with the state below. This may be the reason for the intensity of phonon polarization $(Q_e(0,1),\ Q_g(0,1))$ being comparable with that of $(Q_e(1,2),\ Q_g(1,2))$, respectively.

Figure 4.4 shows the time evolution of the phonon population in the electronic ground and excited states $(P_g(n),\ P_e(n))$ under thermal equilibrium conditions at 300 K. The population $P_e(n)$ of the electronic excited state increases as the population $P_g(n)$ of the ground state decreases by an almost equal amount. This response is observed only for $P_g(0)$ and $P_e(0)$ at 10 K.

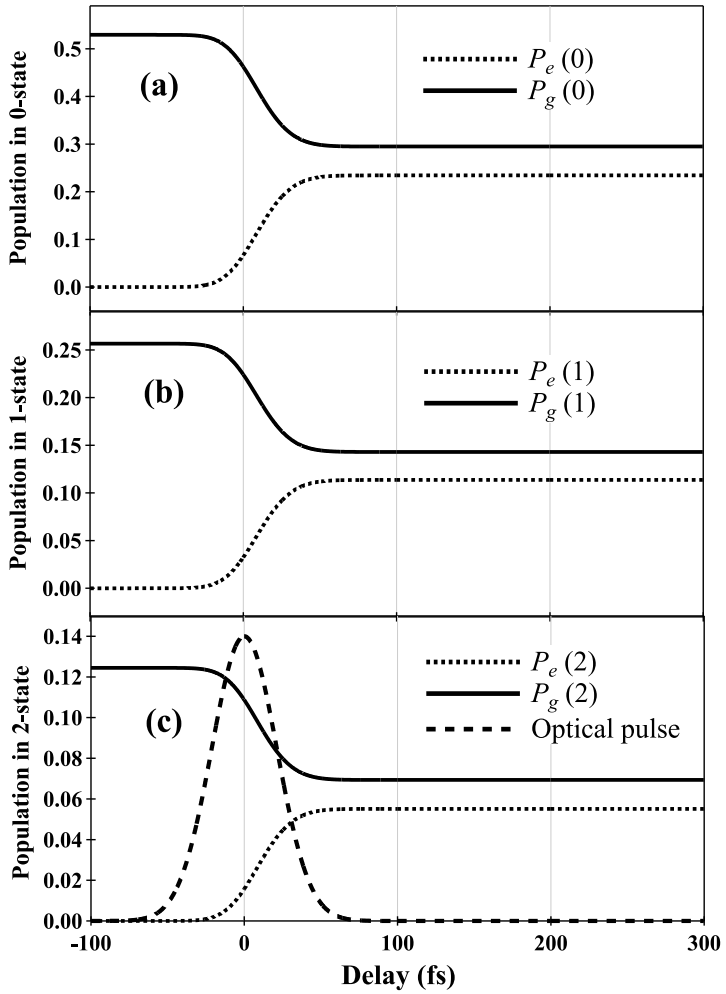

Figure 4.4: The phonon population in each phonon number state in the electronic ground state (solid curves) and excited state (dotted curves) as a function of time delay for an initial state of thermal equilibrium (at 300 K). The optical pulse used in this calculation is superimposed (red solid curve). (a) population at $n = 0$ state: $P_e(0)$ and $P_g(0)$, (b) population at $n = 1$ state: $P_e(1)$ and $P_g(1)$, and (c) population at $n = 2$ state: $P_e(2)$ and $P_g(2)$. This figure is obtained from Ref. [1].

4.3.2 The total coherent phonon amplitude

In the previous section, we evaluated the amplitude of coherent phonon oscillation between selected phonon states. However, in a typical pump-probe measurement, the oscillation intensity of coherent phonons is measured without identifying the phonon state. We also calculated the total amplitude of the photo-induced coherent phonons. Figure 4.5 (a) shows

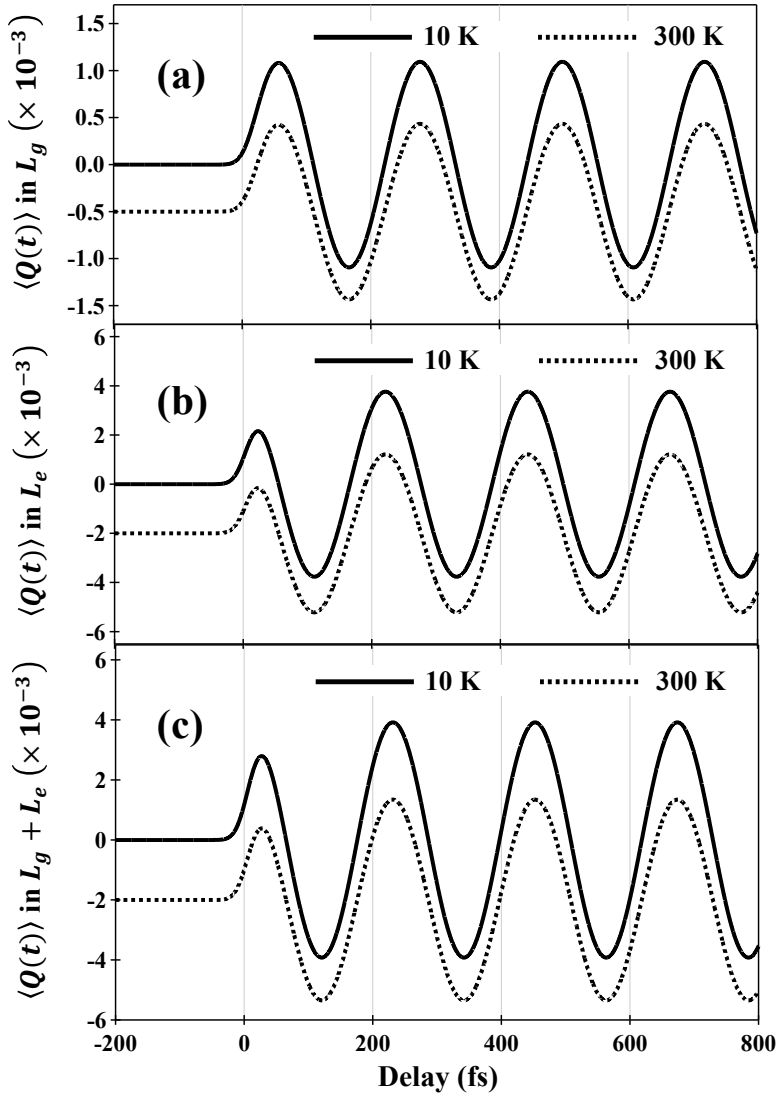

Figure 4.5: The time evolution of the total phonon polarization for the electronic ground and excited states ($Q_g,\ Q_e$). The initial phonon distributions are at 10 K (solid line) and 300 K (dotted line). The top (a) and middle (b) panels show the total polarization in the electronic ground state (Q_g) and excited state (Q_e), respectively. The bottom (c) panel shows the sum of the polarization in the electronic ground and excited states ($Q_g + Q_e$). This figure is obtained from Ref. [1].

the total amplitude of coherent phonons in the electronic ground state ($Q_g = \sum_{n=0}^{4} Q_g(n, n+1)$) as a function of time delay. The oscillation behaviors of Q_g at 10 K and 300 K are almost the same and sine-like. Figure 4.5 (b) shows the total amplitude of coherent phonons in the electronic excited state ($Q_e = \sum_{n=0}^{4} Q_e(n, n+1)$). The oscillation behaviors of Q_e at 10 K and 300 K are almost the same and cosine-like. The oscillation

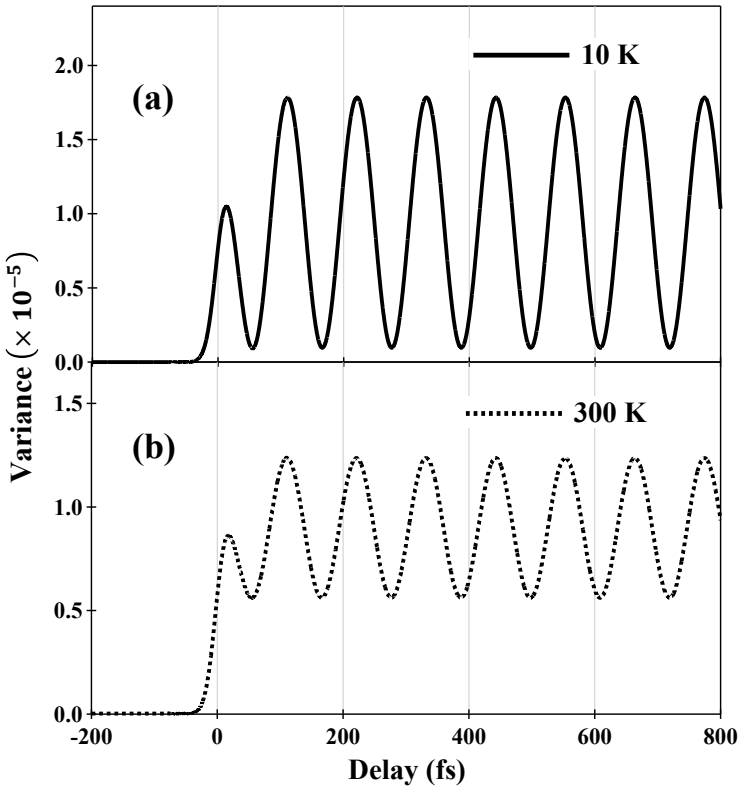

Figure 4.6: The variance of the total phonon states as a function of time delay. The initial phonon distributions are at (a) 10 K (solid line) and (b) 300 K (dotted line). Each data is offset based on the negative delay time: (0.25×10^{-5}) for 10 K, (0.65×10^{-5}) for 300 K. This figure is obtained from Ref. [1].

amplitude of Q_e is four times larger than that of Q_g.

The phonon oscillation characteristics and amplitudes ($\langle Q \rangle = Q_g + Q_e$) at 10 K and 300 K are almost the same (Fig. 4.5 (c)) when we do not select the electronic state. The oscillation shows a phase shift from cosinusoidal oscillation. These results show that the time evolution of the total amplitude of coherent phonons can be evaluated well from a calculation that assumes an initial zero-phonon state.

4.3.3 The fluctuation of coherent optical phonons

The fluctuation of the coherent optical phonons was calculated from the variance ($\Delta Q(t) = \langle Q(t)^2 \rangle - \langle Q(t) \rangle^2$) obtained from the time evolution

coefficients of each electron-phonon composite state. The variances of the total phonon state at each temperature (10 and 300 K) are shown in Figure 4.6. The magnitude of the variance is different for thermal conditions because it depends on the initial phonon distribution.

After pulse irradiation, the variance oscillates periodically at twice the phonon frequency (2ω). The oscillation intensity of the variance (17×10^{-6}) at 10 K is approximately twice that (6.8×10^{-6}) at 300 K. These results indicate that the induced coherent phonons are not in the pure coherent state, in which the mean value of the displacement oscillates with the frequency ω without changing the variance, and are instead slightly squeezed.

A similar oscillation of noise with a frequency of 2ω has been reported in optical pump-probe experiments [27, 28].

4.4 Summary

Theoretical calculations for coherent phonon generation were performed without perturbations and using a thermal equilibrium phonon distribution as the initial condition. The time evolution of the coherent phonon amplitude and phonon population was studied for 4.5-THz phonons with initial conditions of 10 and 300 K. The phonon-state-selected coherent-phonon amplitudes were found to be dependent on the initial phonon distribution. In particular, for an initial distribution at 300 K, the oscillation amplitude between the zero- and one-phonon states was almost the same as that between the one- and two-phonon states, even though the initial population ratio of the one-phonon state to the zero-phonon state was 1/2. Furthermore, it was found that the oscillation amplitude of the phonon polarization did not correspond to the initial phonon distribution, but was closely related to the creation and annihilation processes of the phonon state. The

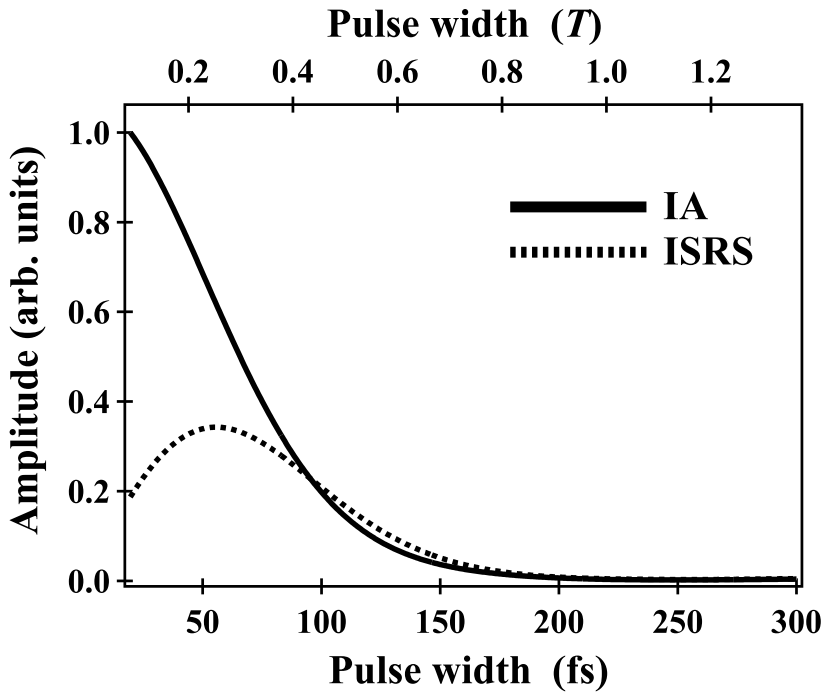

Figure 4.7: The dependence of the pulse width on the phonon amplitude for IA ($\langle Q_e(t)\rangle$ in L_e) and ISRS mechanism ($\langle Q_g(t)\rangle$ in L_g). The solid and dotted curves correspond to the phonon amplitude in IA and ISRS mechanisms, respectively. The bottom horizontal axis corresponds to the pulse width (fs), and the top axis corresponds to the pulse width (T) based on a phonon period of 221 fs. The vertical axis is normalized by the maximum amplitude in IA. The initial phonon distributions are at 300 K. This figure is obtained from Ref. [1].

coherent-phonon amplitudes, considering all phonon states without selecting phonon levels, were almost the same for the 10 K and 300 K initial distributions. The variance of the coherent-phonon amplitude was seen to oscillate with a frequency of 2ω, and the oscillation amplitude was about twice as large for an initial distribution at 10 K than for an initial distribution at 300 K, indicating a dependence on the initial phonon distribution. Future improvements to the model to incorporate anharmonic interactions would be useful.

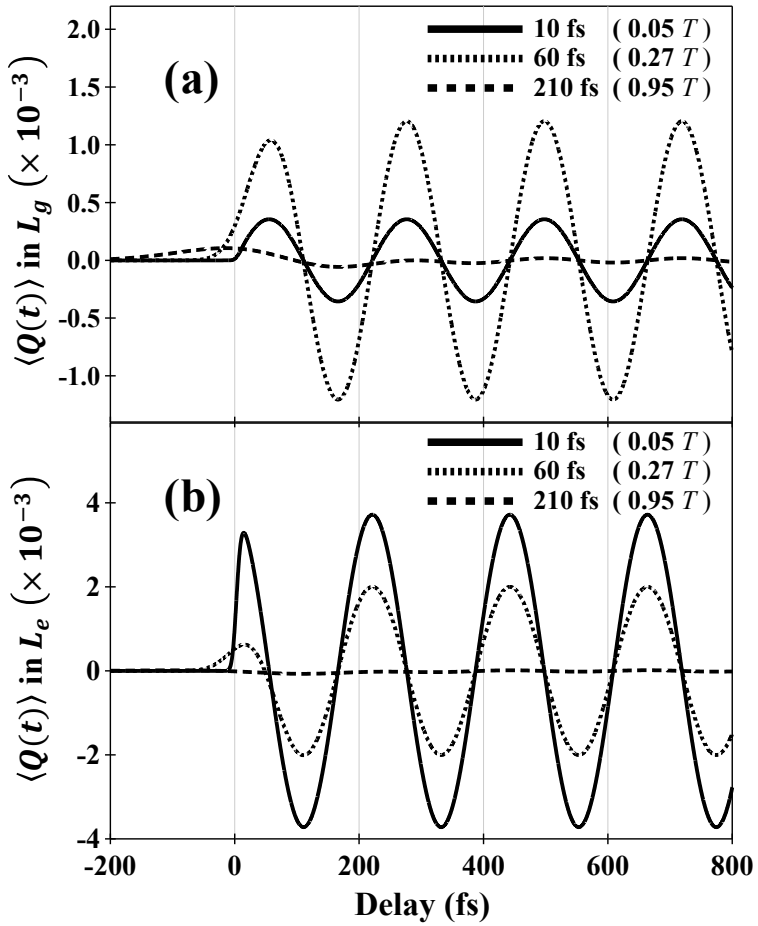

Figure 4.8: The time evolution of the total phonon polarization for the electronic ground and excited states ($Q_g,\ Q_e$). The solid, dotted, and dashed curves are corresponded to the pulse width of 10, 60, and 210 fs, respectively. The top (a) and bottom (b) panels show the total polarization in the electronic ground state (Q_g) and excited state (Q_e), respectively. The initial phonon distributions are at 300 K. This figure is obtained from Ref. [1].

Appendix A: The dependence of the pulse width

We evaluated the pulse width dependence of coherent phonons at 300 K.

Figure A 4.7 shows the dependence of the pulse width on the amplitude in the expectation value of the phonon coordinate in ISRS and IA. In Fig. A 4.7, the coherent phonon amplitude via the IA mechanism dominates in the case of an extremely short pulse width (transition-limited condition). By contrast, the amplitude via the ISRS mechanism reaches its maximum value at pulse widths of about 60 fs (i.e., about $0.3\ T$ with respect to the

phonon period T of 221 fs). This result is consistent with the previous reports using second-order perturbation theory [23].

Figure A 4.8 shows the time evolution of the expectation values of the phonon coordinate operators via ISRS and IA ($\langle Q_g(t)\rangle$, $\langle Q_e(t)\rangle$) at several pulse widths. The pulse widths were set to 10, 60, and 210 fs. In Fig. A 4.8(a), the initial behavior of coherent phonons via ISRS around a delay time of 0 fs shows a more sine-like response as the pulse width is shortened. This is because it is close to the transition limit of the excited and de-excited processes of the electronic state in the Raman process. Furthermore, in Fig. A 4.8(b), the amplitude via IA became comparable to the second periodic oscillation under the pulse width of 10 fs. This is caused by the sudden electronic transition, where the excited electrons oscillate on the potential energy surface in the excited state. These results were also identical to those of the second-order perturbations calculated in the low-temperature approximation [23].

Appendix B: The dependence of the photoexcitation energy

We examined the effect of photoexcitation energy on coherent phonon behaviors at 300 K. The photoexcitation energies were set to 1.30 and 1.45 eV, corresponding to the energies below and above the band gap (1.40 eV).

Fig. B 4.1(a) shows the time evolution of coherent phonons on the ISRS. The coherent phonon amplitude is slightly smaller under high energy excitation than the resonance of the band gap, and this is because of the effect of laser detuning [23]. This laser detuning is caused by the contribution as the term of $\exp\left[-i\Delta E t/\hbar\right] = \exp\left[-i\left(\varepsilon_e - \varepsilon_g - \hbar\Omega_0\right)t/\hbar\right]$. In low energy excitation at 1.30 eV, the coherent phonon amplitudes became much smaller than those under band excitation. By contrast, in Fig. B 4.1(b),

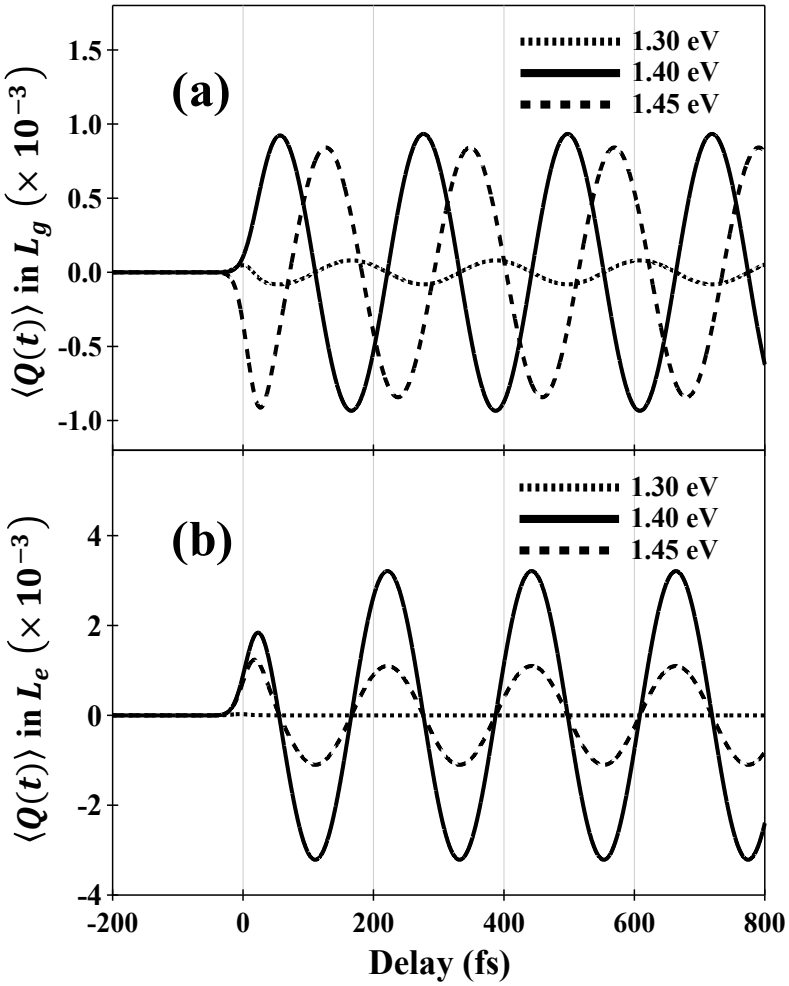

Figure B 4.1: The dependence of the photoexcitation energy on the coherent phonons for the electronic ground and excited states. The dotted, solid, dashed curves are corresponded to the excitation energy of optical pulse under 1.30, 1.40, and 1.45 eV, respectively. The top (a) and bottom (b) panels show the total polarization in the electronic ground state (Q_g) and excited state (Q_e), respectively. The initial phonon distributions are at 300 K. This figure is obtained from Ref. [1].

the amplitude of coherent phonons on the IA at 1.45 eV is much smaller than that of resonance excitation. This is also an effect of laser detuning. Moreover, no coherent phonon oscillations in IA are observed under photoexcitation below band gap energy.

References

[1] I. Takagi and K. G. Nakamura, Solid State Commun **360**, 115053 (2023).

[2] Y.-X. Yan, E. B. Gamble, and K. A. Nelson, J. Chem. Phys. **83**, 5391 (1985).

[3] K. Sokolowski-Tinten, C. Blome, J. Blums, A. Cavalleri, C. Dietrich, A. Tarasevitch, I. Uschmann, E. Förster, M. Kammler, M. Horn-von-Hoegen, and D. von der Linde, Nature **422**, 287 (2003).

[4] S. L. Johnson, P. Beaud, C. J. Milne, F. S. Krasniqi, E. S. Zijlstra, M. E. Garcia, M. Kaiser, D. Grolimund, R. Abela, and G. Ingold, Phys. Rev. Lett. **100**, 155501 (2008).

[5] R. P. Chatelain, V. R. Morrison, B. L. M. Klarenaar, and B. J. Siwick, Phys. Rev. Lett. **113**, 235502 (2014).

[6] H. J. Zeiger, J. Vidal, T. K. Cheng, E. P. Ippen, G. Dresselhaus, and M. S. Dresselhaus, Phys. Rev. B **45**, 768 (1992).

[7] A. V. Kuznetsov and C. J. Stanton, Phys. Rev. Lett. **73**, 3243 (1994).

[8] R. Merlin, Solid State Commun **102**, 207 (1997).

[9] G. C. Cho, W. Kütt, and H. Kurz, Phys. Rev. Lett. **65**, 764 (1990).

[10] T. Dekorsy, T. Pfeifer, W. Kütt, and H. Kurz, Phys. Rev. B **47**, 3842 (1993).

[11] T. Dekorsy, G. C. Cho, and H. Kurz, "Coherent phonons in condensed media", in *Light scattering in solids viii: fullerenes, semiconductor surfaces, coherent phonons*, edited by M. Cardona and G. Güntherodt (Springer Berlin Heidelberg, Berlin, Heidelberg, 2000), pp. 169–209.

[12] G. Lanzani, G. Cerullo, and S. De Silvestri, *Coherent vibrational dynamics*, Practical Spectroscopy (CRC Press, 2007).

[13] A. M. Weiner, D. E. Leaird, G. P. Wiederrecht, and K. A. Nelson, J. Opt. Soc. Am. B **8**, 1264 (1991).

[14] T. Dekorsy, W. Kütt, T. Pfeifer, and H. Kurz, Europhys. Lett. **23**, 223 (1993).

[15] M. Hase, K. Mizoguchi, H. Harima, S. Nakashima, M. Tani, K. Sakai, and M. Hangyo, Appl. Phys. Lett. **69**, 2474 (1996).

[16] H. Takahashi, K. Kato, H. Nakano, M. Kitajima, K. Ohmori, and K. G. Nakamura, Solid State Commun **149**, 1955 (2009).

[17] J.-H. Kim, A. Nugraha, L. Booshehri, E. Hároz, K. Sato, G. Sanders, K.-J. Yee, Y.-S. Lim, C. Stanton, R. Saito, and J. Kono, Chem. Phys. **413**, 55 (2013).

[18] K. G. Nakamura, K. Yokota, Y. Okuda, R. Kase, T. Kitashima, Y. Mishima, Y. Shikano, and Y. Kayanuma, Phys. Rev. B **99**, 180301 (R) (2019).

[19] T. Kimata, K. Yoda, H. Matsumoto, H. Tanabe, F. Minami, Y. Kayanuma, and K. G. Nakamura, Phys. Rev. B **101**, 174301 (2020).

[20] A. V. Kuznetsov and C. J. Stanton, Phys. Rev. B **48**, 10828 (1993).

[21] H. Sasaki, R. Tanaka, Y. Okano, F. Minami, Y. Kayanuma, Y. Shikano, and K. G. Nakamura, Sci. Rep **8**, 9609 (2018).

[22] H. Matsumoto, T. Kitashima, T. Maruhashi, I. Takagi, Y. Kayanuma, and K. G. Nakamura, Solid State Commun **327**, 114215 (2021).

[23] K. G. Nakamura, Y. Shikano, and Y. Kayanuma, Phys. Rev. B **92**, 144304 (2015).

[24] Y. Kayanuma and K. G. Nakamura, Phys. Rev. B **95**, 104302 (2017).

[25] I. Takagi, Y. Kayanuma, and K. G. Nakamura, Phys. Rev. B **104**, 134301 (2021).

[26] K. Ishioka, M. Kitajima, and O. V. Misochko, J. Appl. Phys. **100**, 093501 (2006).

[27] O. V. Misochko, K. Sakai, and S. Nakashima, Phys. Rev. B **61**, 11225 (2000).

[28] O. V. Misochko, Phys. Lett. A **269**, 97 (2000).

Chapter 5
Coherent phonon generation with open quantum theory; optical intensity dependence

In this chapter, we explore the influence of laser intensity on coherent phonons in an electron-phonon composite system from a theoretical point of view. We calculate the coherent phonons from impulsive stimulated Raman scattering (ISRS) and impulsive absorption (IA) mechanisms with a nonperturbative model. In addition, we also attempt to reformulate our previous theoretical models in the framework of open quantum theory, with a further focus on the decoherence phenomenon. This work is published in Solid State Communications [1].

5.1 Introduction

Coherent optical phonons are commonly induced by ultrashort optical pulses [2, 3], and detected as a transient change in the reflectivity or transmissivity of probe pulse by the time-resolved pump–probe method [4–6]. The dynamics of these phonons and electrons in materials have been extensively studied by various approaches [7–10].

The mechanisms that are responsible for generating coherent optical phonons can be broadly classified into two main categories, based on the electronic transition induced by the ultrashort optical pulse: impulsive stimulated Raman scattering (ISRS) [3, 11–14] and impulsive absorption (IA), the latter of which is often termed displacive excitation of coherent phonons (DECP) [3, 15–17]. In the transparent region, the ISRS mecha-

nism is the primary process that generates coherent phonons [3, 11, 12]. In the opaque region, both mechanisms can contribute to generating coherent phonons. The initial phases of the phonon oscillations induced by each mechanism are distinct, with ISRS exhibiting a sine-type oscillation [3, 11–14] and IA exhibiting a cosine-type oscillation [3, 15, 17]. However, determining the contribution of each mechanism in the opaque region can be challenging because the contribution ratio depends on various factors, such as the parameters of the optical pulse.

In previous works, we applied coherent control to achieve quantum path interferometry by using relative phase-locked pump pulse pairs at attosecond precision [18–20]. Quantum path interferometry is a powerful technique for revealing unknown quantum paths in matter. For instance, we observed electronic coherence and phononic interference in n-GaAs simultaneously [18]. Furthermore, by examining the interference shape, we distinguished whether ISRS or IA primarily contributed to the quantum path of the observed quantum state. It is revealed that ISRS mechanisms dominate for quantum paths when electrons are excited near the band edge in n-GaAs. We also developed a theoretical framework that uses a simplified quantum mechanical model for treating the ISRS and IA mechanisms in a unified manner [18, 21]. The characteristics of the experimental results can be reproduced by calculations that use second-order perturbations, representing the lowest-order interaction with the optical field. However, the interference pattern deviated slightly from the theoretical results at high optical intensities because of optical interference between the double-pump pulses [18]. This result suggests a close relationship among the higher-order interactions of intense optical pulses, generation of coherent phonons, and quantum path interference.

Indeed, previous studies on coherent phonons in both the transparent and opaque regions have reported a dependence of the single-pump pulse

on the optical intensity. For instance, in transparent materials such as diamonds, the phonon amplitude exhibits a linear increase up to the pump intensity of approximately $10\ \mathrm{GW/cm^2}$ by irradiation with near-infrared light [22]. In contrast, in opaque regions, the coherent phonon amplitude either linearly changes or gradually saturates at the maximum pump intensity of up to $0.53\ \mathrm{GW/cm^2}$ [23]. Additionally, the nonlinear dependence of coherent phonons under nonresonant excitation by extremely intense optical pulses (around $\mathrm{TW/cm^2}$) has been experimentally and theoretically reported [24].

In this chapter, we present a theoretical study of the dependence of coherent phonon generation on the optical pulse intensity. Specifically, we are interested in the pulse-intensity dependence of the generation efficiency of the coherent phonons in accordance with the difference in the generation mechanisms, namely either by ISRS or IA. This is quite natural because the transition paths to the final states of the transition differ between the two processes. Furthermore, we focused not only on the case of single-pulse excitation but also on the case of double-pulse excitation. Regarding double-pulse excitation, it will be interesting to see the delay-time dependence of the amplitude of the coherent phonons because at small values of the delay time, the two optical pulses might overlap temporarily, so that the effect of the high-intensity excitation will be more pronounced. It will be shown below that the profile of the generation amplitudes of coherent phonons for GaAs at low temperatures supports our proposal that the generation mechanism is ISRS [18].

5.2 Model with open quantum theory

The generation efficiency of coherent optical phonons are examined for an electron–phonon composite system with two electronic bands and a

single longitudinal optical (LO) phonon. Ultrashort optical pulses have a broad spectral width. It is necessary to consider an energy broadening for electronic excited states. The excited electron band exhibits a continuous level with inhomogeneous broadening of the energy. This broadening gives rise to dephasing in the excited states. In our previous work [18, 25], this effect was treated simply by introducing a Lorentz function for the excited state. Note that the shape of the Lorentzian function exhibited not only the state density but also the effective coupling constants with the LO phonon. The width of the Lorentzian function was determined phenomenologically by adjusting the relaxation time of the electronic interference fringe in comparison with experimental data [18].

In the present work, we study the dependence of the coherent phonons on the intensity of optical pulses, using the quantum master equation approach to the electron-phonon composite system. We describe the dephasing of the electronic states in the excited states in terms of the Lindblad equation. The system Hamiltonian for the electron–phonon composite state [21, 26, 27] can be expressed as follows:

$$H = H_{\rm ph} + H_{\rm el} + H_{\rm ep}, \tag{5.1}$$

$$H_{\rm ph} = \hbar\omega b^{\dagger} b, \tag{5.2}$$

$$H_{\rm el} = \sum_{k} \sum_{\nu=h,l} \varepsilon_{\nu}(k) a^{\dagger}_{k,\nu} a_{k,\nu} + \sum_{k} \varepsilon_{c}(k) a^{\dagger}_{k,c} a_{k,c}, \tag{5.3}$$

$$H_{\rm ep} = \sum_{k} \alpha\hbar\omega (b^{\dagger} + b) a^{\dagger}_{k,c} a_{k,c}, \tag{5.4}$$

where $H_{\rm ph}$, $H_{\rm el}$ represent the Hamiltonian of the phonon and electronic systems, respectively. $H_{\rm ep}$ is the Hamiltonian of the electron–phonon interaction. The parameter ω is the phonon frequency, and $\varepsilon_{\nu}(k)$, $\varepsilon_{c}(k)$ are the energies of the valence and conduction bands, respectively. k is the wavevector of the electron. The operators $a_{k,\nu}$ and $a_{k,c}$ are the annihila-

tion operator for the electrons (fermion) in valence and conduction bands. Furthermore, the index ν refers to the heavy (h) and light hole (l) bands. The band structure of GaAs has been extensively studied [28, 29]. The operators $b^{\dagger},\ b$ are the creation and annihilation operators, respectively, for phonons (boson) at the Γ-point. In general, the wavelength of the optical pulse exceeds the lattice constant, and the electron-hole pairs generated by the optical pulse are uniformly distributed around the Γ-point. Therefore, the wavevectors of phonons which can be excited by the optical process are only those close to the Γ-point ($q = 0$). The parameter α is a dimensionless coupling constant between the electron and phonon states, corresponding to the diagonal elements of the electron–phonon coupling matrix. In a bulk crystal, the Huang–Rhys factor (α^2) is considered to be small; i.e., $\alpha^2 \ll 1$. In our simple model, the effect of transient depletion of field screening (TDFS) is taken into account in the diagonal elements (forbidden Raman scattering) in the electron–phonon coupling matrix [30], while the depth dependence of the effect is not considered.

Within the rotating-wave approximation, the interaction Hamiltonian between light and electrons is expressed by

$$H_I(t) = \sum_k \sum_{\nu=h,l} \mu_{k,\nu} E(t) e^{-i\Omega_0 t} a^{\dagger}_{k,c} a_{k,\nu} + H.c., \tag{5.5}$$

where the parameter $\mu_{k,\nu}$ is the transition dipole moment and Ω_0 is the frequency of optical pulse. Here $H.c.$ represents the Hermitian conjugate term and corresponds to $\mu^*_{k,\nu} E^*(t) e^{i\Omega_0 t} a_{k,c} a^{\dagger}_{k,\nu}$. $f(t)$ is the envelope function of the pump pulses, expressed as $E(t) = E_0 f(t)$ in the single-pulse case. Moreover, in the case of double-pulse excitation, it is denoted by $E(t) = E_0 f(t) + E_0 f(t - t_{12}) e^{i\Omega_0 t_{12}}$. The time t_{12} is the delay time between pulses 1 and 2. The function $f(t)$ is the Gaussian pulse envelope,

defined as

$$f(t) = \frac{1}{\sqrt{\pi}\sigma} \exp\left(-\frac{t^2}{\sigma^2}\right), \tag{5.6}$$

where E_0 is the amplitude of the electric field and σ is the pulse width.

In this model, the initial electronic distribution is assumed to occupy the valence bands based on the low-temperature approximation. Therefore, we define the electronic ground state as the valence bands are fully occupied; i.e., $|g\rangle = \Pi_{k,\nu} a^{\dagger}_{k,\nu} |vac\rangle$, with $|vac\rangle$ being the vacuum of electron [31, 32]. In addition, the electronic excited state is defined as $|e_{k,\nu}\rangle = a^{\dagger}_{k,c} a_{k,\nu} |g\rangle$.

The state vector $|\psi(t)\rangle$ is expanded in the composite system by using basis sets of electronic states ($|g\rangle$ and $|e_{k,\nu}\rangle$) and phonon Fock states ($|n\rangle$):

$$|\psi(t)\rangle = \sum_{k} \sum_{\nu=h,l} \sum_{n} (c_n(t) |g, n\rangle + d_{k,\nu,n}(t) |e_{k,\nu}, n\rangle), \tag{5.7}$$

where $c_n(t)$ and $d_{k,\nu,n}(t)$ are the time-dependent probability amplitudes of the n-phonon states in the electronic ground and excited states, respectively. Note that $|g, n\rangle$ is the electronic ground band in the n-phonon state; i.e., $|g, n\rangle = |g\rangle \otimes |n\rangle$. Here, we consider the representative excited state with the wavevector at which the bandgap matches the photon energy ($\hbar\Omega_0 = \varepsilon_c(k) - \varepsilon_\nu(k)$). We defined the electronic excited state with energy broadening for this condition as $|e\rangle$ [18, 25, 26, 30, 33].

In this calculation, the density operator formalism and the quantum master equation [34, 35] are used to calculate the time evolution of the density operator:

$$i\hbar \frac{d}{dt}\rho(t) = [H, \rho(t)] + i\hbar \hat{D}(\rho(t)), \tag{5.8}$$

$$\hat{D}(\rho(t)) = \sum_{i} \Gamma_i \left[2L_i \rho(t) L_i^{\dagger} - \{L_i^{\dagger} L_i, \rho(t)\}\right], \tag{5.9}$$

where H is the total Hamiltonian $H = H_0 + H_I(t)$ and $\rho(t)$ is the density

operator $\rho(t) = |\psi(t)\rangle \langle\psi(t)|$. $\hat{D}(\rho(t))$ is the dissipator. L_i and Γ_i are the Lindblad operator and decay rate for the electronic and phonon states, respectively. Dephasing is introduced as a Markovian process described by the phenomenological Lindblad operator [35, 36]:

$$L_1 = |e\rangle \langle e|, \tag{10.A}$$

$$L_2 = |g\rangle \langle e|, \tag{10.B}$$

$$L_3 = b^\dagger b = \hat{n}. \tag{10.C}$$

where index 1 refers to pure dephasing of the electronic excited state, including inhomogeneous broadening of the electronic excited bands. Label 2 refers to decay of the electronic excited state. Label 3 refers to pure dephasing of the phonon state.

The expectation value of the phonon coordinate operator ($\langle Q(t)\rangle = \mathrm{Tr}[Q\rho(t)]$, where $Q = \sqrt{\hbar/2M\omega}(b^\dagger + b)$ and M is the reduced mass of atoms per unit cell) is calculated from the probability amplitudes obtained by solving the simultaneous differential equation [in Eq. (5.8)]. The coherent phonon behavior corresponds to the density operator's coherence term. Then, the coherent phonons in the IA and ISRS mechanisms are distinguished by the selected electronic states; i.e., $\langle Q_{\mathrm{IA}}(t)\rangle = \sum_{n,m} \langle e,n|Q|e,m\rangle$, and $\langle Q_{\mathrm{ISRS}}(t)\rangle = \sum_{n,m} \langle g,n|Q|g,m\rangle$, where n, m are the numbers of phonon quanta.

In the actual calculations, the quantum master equation is applied for the coherent phonon generation model under a Markov approximation, implemented in the Python package QuTiP [37] for numerical calculations. The GaAs parameter is the simplest test material for this subject. The electron–phonon coupling constant is set to α = 0.1. The central energy of the electronic excited state is set to ε_c = 1.52 eV, which corresponds to the center of the optical frequency Ω_0. The vibrational energy is set to $\hbar\omega$ = 36

meV (approximately 8.7 THz). The parameter of the optical pulse is set to σ = 30 fs, and $\mu_k E_0$ = 0.46 at a peak power intensity of 0.087 $\mathrm{GW/cm^2}$. The transition strength ($\mu_k E_0$) is determined from information about the laser pulse used in our group. Appendix A describes the details of this parameter.

The initial state of the electron–phonon system is assumed to be an electronic ground state with zero-phonon ($\rho(-\infty) = |g,0\rangle\langle g,0|$). Under the assumption of weak electron-phonon coupling, the phonon states are set to be two levels ($n = 0, 1$) for both the electronic ground and excited states. Furthermore, the decay rate of the dissipator (Γ_i) is set as $\Gamma_1 = 1/30$ $(1/\mathrm{fs})$. Note that the decay rate of Γ_1 depends on the pulse width, the band structure, and the electron-phonon coupling, among others. Additionally, the decay of the electronic excited state (Γ_2) and pure dephasing of the phonon state (Γ_3) are disregarded in this study because their respective decay times were as long as pico- to nanoseconds.

An electron in the ground state is excited to $|e,0\rangle$ and $|e,1\rangle$ coherently by a pump pulse (Fig. 5.1). This induces a coherent oscillation of the LO phonon in the electronic excited state (IA). At the same time, the excited electron might be de-excited by the same pump pulse from $|e,0\rangle$ and $|e,1\rangle$ to $|g,0\rangle$ and $|g,1\rangle$ coherently. This results in coherent oscillation of the LO phonon in the ground state of the electron (ISRS). Because the final state of the transition in the IA process is band states, the saturation is slow when the intensity of the pump pulse is increased. However, the final states of the transition for the ISRS process are the discrete states $|g,0\rangle$ and $|g,1\rangle$, such that they will be easily saturated. This phenomenon of the saturation of transitions can be termed a blockade of the stimulated Raman process.

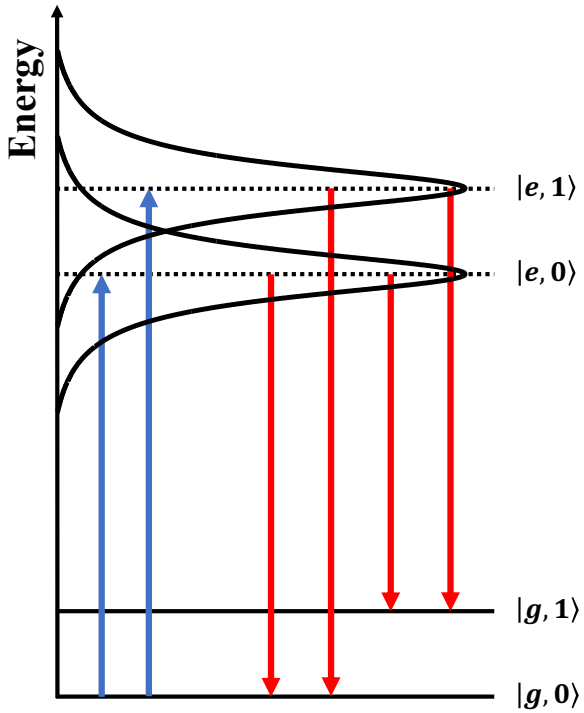

Figure 5.1: Schematic of saturation phenomena in the IA and ISRS mechanisms. In the IA mechanism, coherent phonons are generated by excitation (blue line) from the electronic ground state in the initial state. In the ISRS mechanism, the generation of coherent phonons requires an initial electronic excitation to an excited state as the intermediate state (blue line), which subsequently undergoes electronic de-excitation to return to the electronic ground state (red line). The IA mechanism requires the blue line path, while the ISRS consists of both red and blue lines. This figure is obtained from Ref. [1].

5.3 Results and discussion on intensity dependence

5.3.1 Single-pulse excitation

First, we examine the optical intensity dependence of the coherent phonons induced by single-pulse excitation.

Figure 5.2 shows the time evolution of coherent phonons generated via each mechanism under resonant excitation ($\hbar\Omega_0 = 1.52$ eV) at 0.02 GW/cm^2 of a low pulse intensity. Both mechanisms induced coherent phonons, resulting in phonon oscillations. The ISRS mechanism $\langle Q_{\mathrm{ISRS}}(t)\rangle$ exhibited an oscillation with a slight lag compared with the IA mechanism $\langle Q_{\mathrm{IA}}(t)\rangle$. It is evident that the oscillation of $\langle Q_{\mathrm{IA}}(t)\rangle$ is

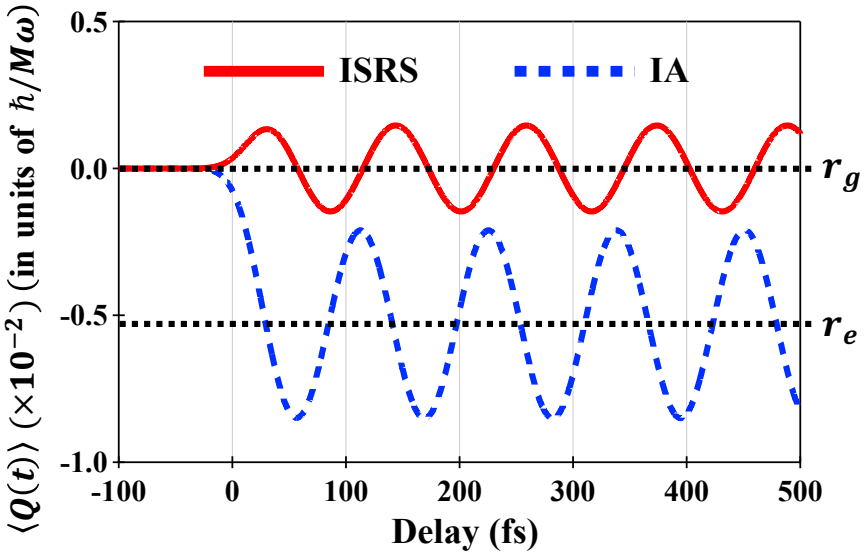

Figure 5.2: Time evolution of the expectation value of the phonon coordinate operator $\langle Q(t)\rangle$ by the selected electronic states. Red curves and blue dotted lines represent the amplitudes in ISRS and IA, respectively. r_g and r_e are the positions of the minimum of the phonon potential of the electronic ground and excited states. This figure is obtained from Ref. [1].

cosine-like, whereas that of $\langle Q_{\mathrm{ISRS}}(t)\rangle$ is sine-like.

Figure 5.3 shows the phonon amplitude through both IA and ISRS as a function of the pulse intensity. We plot the phonon amplitude as the absolute value of the phonon oscillation amplitudes. Initially, we investigate the relationship between the coherent phonon and pulse intensity under resonant excitation [Figure 5.3(a)]. The phonon amplitudes of both mechanisms are increased with increasing pulse intensity. In our previous perturbation calculations for coherent phonons, we obtained numerically that the generation efficiency via ISRS and IA is proportional to the pulse intensity [21]. In Figure 5.3(a), a linear variation of the phonon amplitude is exhibited in the region of extremely weak pulse intensity, as in the perturbation calculations. In addition, the ISRS phonon amplitude exhibits a nonlinear increase at a substantial pulse power of approximately 0.06 $\mathrm{GW/cm^2}$ and greater. In contrast, the phonon amplitude via IA exhibits a slight nonlinear change before 0.4 $\mathrm{GW/cm^2}$, followed by substantial sat-

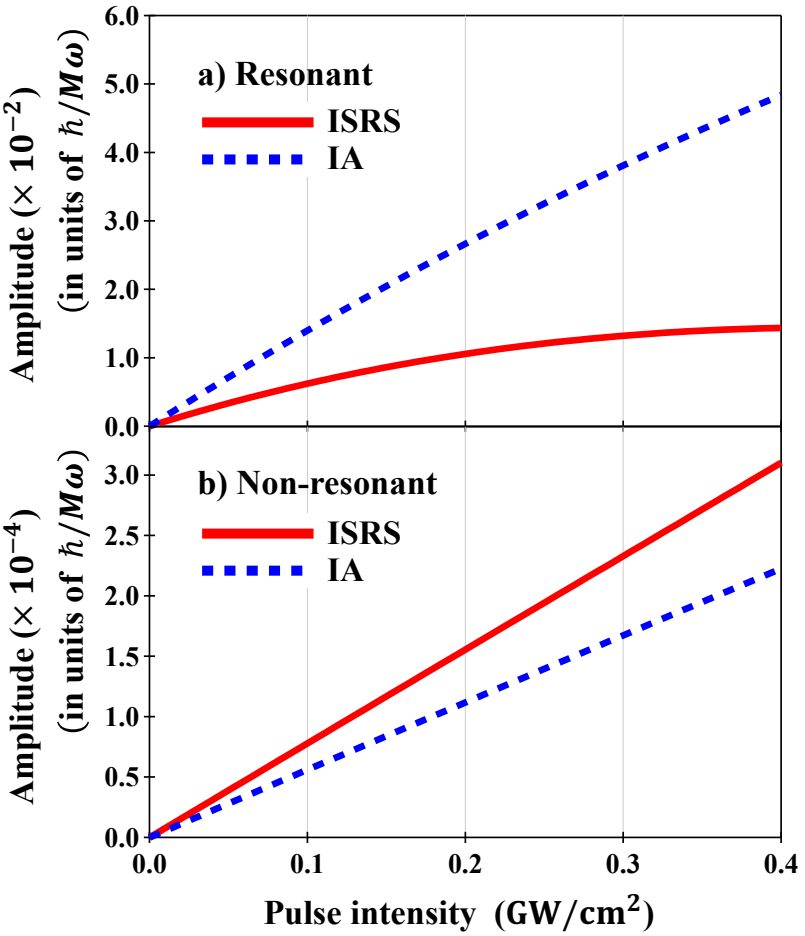

Figure 5.3: Theoretical phonon amplitude via ISRS and IA mechanisms as a function of the pulse intensity ($\mathrm{GW/cm^2}$). (a): Pulse intensity dependence of coherent phonons under resonant excitation. (b): Pulse intensity dependence of coherent phonons under nonresonant excitation. Red curves and blue dotted lines represent the amplitudes in ISRS and IA, respectively. Phonon amplitude in IA is plotted as an intensity change with the center of oscillation as the baseline. Note the difference of the scale in the vertical axis between a) and b). This figure is obtained from Ref. [1].

uration at intensities greater than approximately 1.5 $\mathrm{GW/cm^2}$ (not shown here). Next, we examine the pulse intensity dependence under nonresonant excitation [$\hbar\Omega_0 = 1.20\,\mathrm{eV}$, Figure 5.3(b)]. Note the difference of the scale in the vertical axis between Fig. 5.3(a) and (b). The ISRS phonon amplitude is changed linearly with increasing pulse intensity. In addition, the phonon amplitude via IA is observed to be smaller than that of ISRS, and changed linearly with respect to pulse intensity. The reason for the smaller amplitude of the IA mechanism is due to the laser detuning effect [21].

There is a marked difference in the blockade behavior of the oscillation amplitude between the two mechanisms.

The two reasons for ISRS having a saturation of phonon amplitudes compared with the IA mechanism, as previously mentioned, are as follows. First, the final state of each mechanism is an electronic continuous state in IA but a single state in ISRS. In this model, we introduced dephasing—such as intraband phase relaxation of the electronic excited states—using the Lindblad operator in a phenomenological manner. The electronic excited state $|e\rangle$ with the L_1 dissipator corresponds to a continuous excited band with corresponding broadening. Thus, the effectiveness of the saturation phenomenon between IA and ISRS is attributable to the final state being a continuous band or single level. Second, the differences in the quantum path also affect the saturation phenomenon. In Figure 5.1, we consider the state vector of the electron–phonon composite system. In the IA mechanism, coherent phonons are generated by electronic excitation from the electronic ground state induced by an optical pulse. However, the ISRS mechanism requires an initial electronic excitation to an excited state as the intermediate state, which subsequently undergoes electronic de-excitation to return to the electronic ground state.

5.3.2 Double-pulse excitation

In this section, we apply our model to calculate phonon amplitudes excited with double pulses as a function of pump–pump delay t_{12}. We initially assess the behavior of quantum path interference via the IA and ISRS mechanisms at 0.004 $\mathrm{GW/cm^2}$ (equivalent to 1 mW) at low pulse intensity (i.e., the linear region in Figure 5.2), wherein perturbation theory is applicable.

Figure 5.4(a)-(b) shows the phonon amplitude via each mechanism as

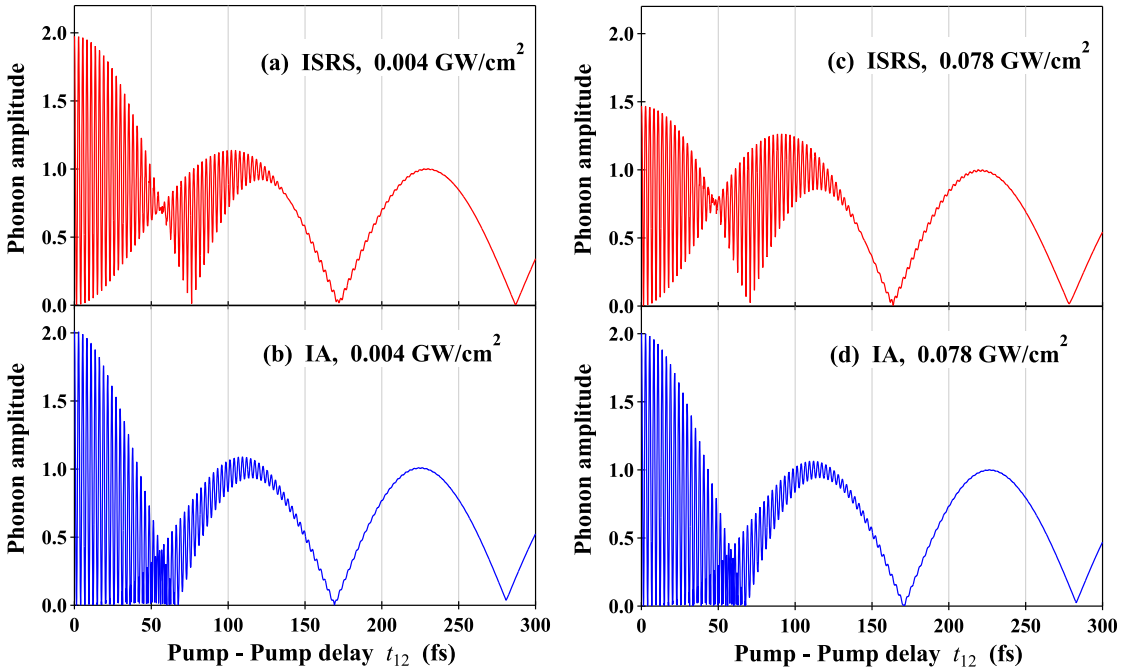

Figure 5.4: Phonon amplitude via ISRS and IA mechanisms as a function of pump–pump delay t_{12}. (a)-(b): Theoretical quantum path interference results for double-pulse excitation at weak optical intensities (0.004 $\mathrm{GW/cm^2}$) in ISRS and IA. (c)-(d): Theoretical quantum path interference under higher optical intensity (0.078 $\mathrm{GW/cm^2}$) in ISRS and IA. The red and blue curves represent the phonon amplitude in ISRS and IA, respectively. Phonon amplitude in IA is determined through the baseline with the center of oscillation. Vertical axis of each data set normalized with the maximum phonon amplitude in the region where only phonon interference was observed after around 200 fs. This figure is obtained from Ref. [1].

a function of the pump–pump delay time (t_{12}) under double-pulse excitation. The interference shapes at low pulse intensity are consistent with those calculated by second-order perturbation theory [18]. A fast oscillation of the electronic coherence is discernible with a slow oscillation of the phononic interference. The ratio of the maximum phonon amplitude after 200 fs of pump–pump delay time to the maximum phonon amplitude at 0 fs was approximately $1/2$.

Figure 5.4(c)-(d) shows the phonon amplitude resulting from the ISRS and IA process under higher intensity double-pulse excitation (at 0.078 $\mathrm{GW/cm^2}$, corresponding to 18 mW) as a function of the pump–pump delay time (t_{12}). The ISRS interference pattern exhibits a pronounced sup-

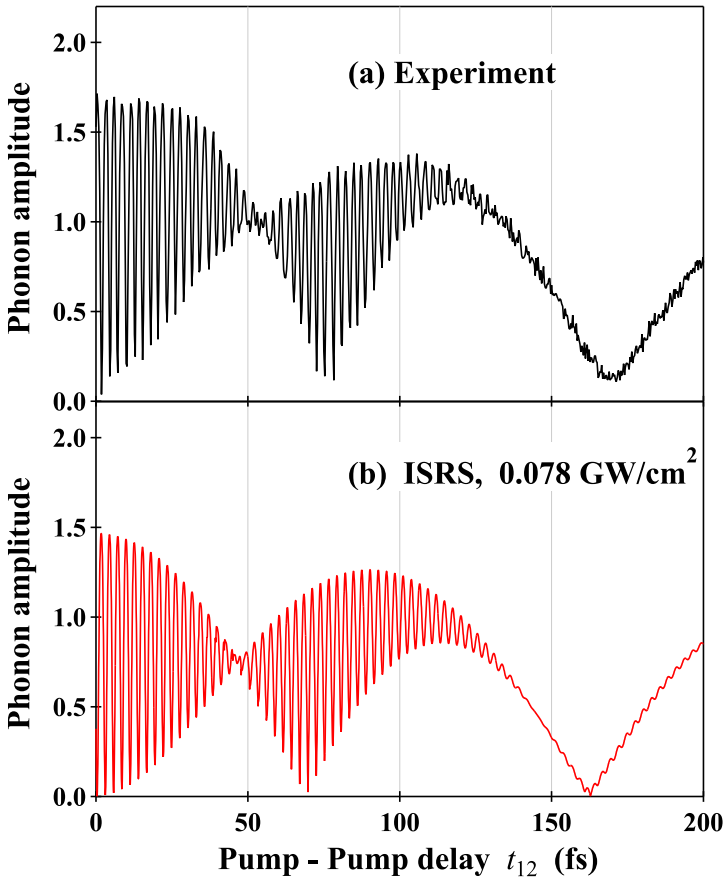

Figure 5.5: Comparison of experimental and theoretical results under double-pulse excitation. (a): Experimental results of n-GaAs in previous work [18]. (b): Theoretical results under higher intensity in ISRS. Vertical axis of each data set normalized with the maximum phonon amplitude in the region of only phonon interference. This figure is obtained from Ref. [1].

pression in phonon intensity at a delay time of 0 fs compared with low-power pulse irradiation. In contrast, the interference pattern via IA does not exhibit shape alteration and remains unchanged compared with the low intensities. These phenomena indicate a blockage in the linear progression of phonon amplitude via ISRS because of high-intensity pulses, as inferred from the calculation of single-pulse excitation.

For comparison, Figure 5.5(a) shows the experimental quantum path interference in n-GaAs in previous work [18], shown with the present calculation [Fig. 5.5(b)]. The theoretical ISRS interference shape (Fig. 5.5(b)) is in alignment with the experimental results obtained in previous work.

It is clearly demonstrated in this comparison that the stimulated Raman blockade is reflected in the experimental data.

5.4 Summary

We performed theoretical calculations for the optical pulse intensity dependence of coherent phonon generation without perturbative theory. There is a difference in the blockade behavior of the phonon amplitude in the ISRS and IA mechanisms in terms of the pulse intensity dependence of single-pulse excitation. We confirmed that coherent phonons via the ISRS mechanism exhibited a substantial nonlinear amplitude change at lower pulse intensities than the IA mechanism. For double-pulse excitation, the quantum path interference corresponded to the phonon blockade of single-pulse excitation. The quantum path interference via the ISRS mechanism exhibited substantial saturation behavior at ca. 0 fs of pump–pump delay, whereas the IA mechanism exhibited almost no saturation behavior. We interpreted the influence of coherent phonons by a high intensity of optical pulses as higher-order interactions than second-order. Furthermore, the difference in the saturation behavior in both mechanisms is attributed to the distinct transition paths to the final states, and also to the difference in the final states, whether it is the energy-broadened excited states in IA, or a single electronic state in the ground state in ISRS.

We found that theoretical calculations incorporating the transition strength with the experimental laser parameters well-reproduced the tendency of the experimental results. These results will provide a more detailed understanding of coherence phenomena by using quantum path interferometry and theoretical models. In particular, the quantum path in a material will be revealed, and ultrafast quantum coherence of electronic states associated with a phonon system can be further quantitatively and

qualitatively evaluated.

Appendix A: Determination of transition strength

We present an estimation of transition strength ($\mu_k E_0$) as a theoretical parameter. We derived this estimation through the information obtained from our optical system, which uses a Ti: sapphire laser (KM laser).

We determined the focused diameter of the pump pulse (σ_{HWHM}) to be approximately 30 $\mu\mathrm{m}$ by measurements in the one-dimensional direction via the knife-edge method. When the laser's intensity distribution is considered to be a two-dimensional Gaussian function, the effective intensity of the laser is approximately 86%. The beam spot is given by πr^2, where $r = \sqrt{2/\ln(2)}\ \sigma_{\mathrm{HWHM}}$. The optical intensity can be determined from the Poynting vector:

$$\mathbf{S} = \mathbf{E} \times \mathbf{H}, \tag{A.5.1}$$

$$S = \sqrt{\frac{\varepsilon}{\mu}}\, E^2, \tag{A.5.2}$$

where ε and μ are the permittivity and permeability, respectively. The electric field E is the time average of the optical field. The time average of the square of the optical field of the pump pulse is obtained by integration over time t:

$$E^2 = \frac{E_0^2}{\pi\sigma^2} \int_{-\infty}^{\infty} \exp\left(-\frac{2t^2}{\sigma^2}\right) \left(2 + e^{-2i\Omega_0 t} + e^{2i\Omega_0 t}\right) dt, \tag{A.5.3}$$

We estimated the magnitude of the Poynting vector (S) in accordance with the laser pulse condition as $S = I/\pi r^2 f$, where I and f are the power of the pump pulse and repetition rate (94 MHz), respectively. Therefore, S

and E_0 can be summarized as follows:

$$S = \frac{E_0^2}{\sigma}\sqrt{\frac{2\varepsilon}{\mu\pi}} = \frac{c\varepsilon_0 E_0^2}{\sigma}\sqrt{\frac{2}{\pi}} \tag{A.5.4}$$

$$E_0 = \sqrt{\frac{S\sigma}{c\varepsilon_0}\sqrt{\frac{\pi}{2}}} = \sqrt{\frac{I\sigma}{c\varepsilon_0\pi r^2 f}\sqrt{\frac{\pi}{2}}} \tag{A.5.5}$$

where ε_0 is the permittivity in a vacuum, and c is the speed of light, and we used the relation $c = 1/\sqrt{\varepsilon_0\mu_0}$.

The transition dipole moment μ_k is classically represented as

$$\mu_k = qr \tag{A.5.6}$$

where q is the elementary charge and r is the interatomic distance. For GaAs, the interatomic distance is approximately 0.5 nm.

Finally, we derived the transition strength at a particular optical intensity:

$$\mu_k E_0 = qr\sqrt{\frac{I\sigma}{c\varepsilon_0\pi r^2 f}\sqrt{\frac{\pi}{2}}} \tag{A.5.7}$$

References

[1] I. Takagi, Y. Kayanuma, and K. G. Nakamura, Solid State Commun **373-374**, 115316 (2023).

[2] Y.-X. Yan, E. B. Gamble, and K. A. Nelson, J. Chem. Phys. **83**, 5391 (1985).

[3] G. Lanzani, G. Cerullo, and S. De Silvestri, *Coherent vibrational dynamics*, Practical Spectroscopy (CRC Press, 2007).

[4] G. C. Cho, W. Kütt, and H. Kurz, Phys. Rev. Lett. **65**, 764 (1990).

[5] R. Merlin, Solid State Commun **102**, 207 (1997).

[6] T. Dekorsy, T. Pfeifer, W. Kütt, and H. Kurz, Phys. Rev. B **47**, 3842 (1993).

[7] K. Sokolowski-Tinten, C. Blome, J. Blums, A. Cavalleri, C. Dietrich, A. Tarasevitch, I. Uschmann, E. Förster, M. Kammler, M. Horn-von-Hoegen, and D. von der Linde, Nature **422**, 287 (2003).

[8] S. L. Johnson, P. Beaud, C. J. Milne, F. S. Krasniqi, E. S. Zijlstra, M. E. Garcia, M. Kaiser, D. Grolimund, R. Abela, and G. Ingold, Phys. Rev. Lett. **100**, 155501 (2008).

[9] R. P. Chatelain, V. R. Morrison, B. L. M. Klarenaar, and B. J. Siwick, Phys. Rev. Lett. **113**, 235502 (2014).

[10] T. Dekorsy, G. C. Cho, and H. Kurz, "Coherent phonons in condensed media", in *Light scattering in solids viii: fullerenes, semiconductor surfaces, coherent phonons*, edited by M. Cardona and G. Güntherodt (Springer Berlin Heidelberg, Berlin, Heidelberg, 2000), pp. 169–209.

[11] Y.-X. Yan and K. A. Nelson, J. Chem. Phys. **87**, 6240 (1987).

[12] Y.-X. Yan and K. A. Nelson, J. Chem. Phys. **87**, 6257 (1987).

[13] L. Dhar, J. A. Rogers, and K. A. Nelson, Chem. Rev. **94**, 157 (1994).

[14] T. E. Stevens, J. Kuhl, and R. Merlin, Phys. Rev. B **65**, 144304 (2002).

[15] T. K. Cheng, J. Vidal, H. J. Zeiger, G. Dresselhaus, M. S. Dresselhaus, and E. P. Ippen, Appl. Phys. Lett. **59**, 1923 (1991).

[16] A. V. Kuznetsov and C. J. Stanton, Phys. Rev. Lett. **73**, 3243 (1994).

[17] H. J. Zeiger, J. Vidal, T. K. Cheng, E. P. Ippen, G. Dresselhaus, and M. S. Dresselhaus, Phys. Rev. B **45**, 768 (1992).

[18] K. G. Nakamura, K. Yokota, Y. Okuda, R. Kase, T. Kitashima, Y. Mishima, Y. Shikano, and Y. Kayanuma, Phys. Rev. B **99**, 180301 (R) (2019).

[19] H. Matsumoto, T. Kitashima, T. Maruhashi, I. Takagi, Y. Kayanuma, and K. G. Nakamura, Solid State Commun **327**, 114215 (2021).

[20] Y. Furusho, R. Yagi, M. Suda, T. Maruhashi, I. Takagi, Y. Kayanuma, F. Minami, and K. G. Nakamura, Solid State Commun **360**, 115056 (2023).

[21] K. G. Nakamura, Y. Shikano, and Y. Kayanuma, Phys. Rev. B **92**, 144304 (2015).

[22] K. Ishioka, M. Hase, M. Kitajima, and H. Petek, Appl. Phys. Lett. **89**, 231916 (2006).

[23] K. Ishioka, M. Kitajima, and K. Ushida, J. Phys. Soc. Japan **75**, 084704 (2006).

[24] K. Uchida, K. Nagai, N. Yoshikawa, and K. Tanaka, Phys. Rev. B **101**, 094301 (2020).

[25] K. G. Nakamura, K. Ohya, H. Takahashi, T. Tsuruta, H. Sasaki, S.-i. Uozumi, K. Norimatsu, M. Kitajima, Y. Shikano, and Y. Kayanuma, Phys. Rev. B **94**, 024303 (2016).

[26] Y. Kayanuma and K. G. Nakamura, Phys. Rev. B **95**, 104302 (2017).

[27] I. Takagi and K. G. Nakamura, Solid State Commun **360**, 115053 (2023).

[28] I. Vurgaftman, J. R. Meyer, and L. R. Ram-Mohan, J. Appl. Phys. **89**, 5815 (2001).

[29] H. Tanimura and K. Tanimura, Phys. Rev. B **102**, 045204 (2020).

[30] I. Takagi, Y. Kayanuma, and K. G. Nakamura, Phys. Rev. B **104**, 134301 (2021).

[31] C. Kittel, *Quantum theory of solids* (Wiley, 1987).

[32] R. P. Feynman, *Statistical mechanics: a set of lectures* (CRC Press, 2018).

[33] I. Takagi, Y. Kayanuma, and K. G. Nakamura, Phys. Rev. B **107**, 184305 (2023).

[34] C. Gardiner and P. Zoller, *Quantum noise: a handbook of markovian and non-markovian quantum stochastic methods with applications to quantum optics*, Springer Series in Synergetics (Springer Berlin Heidelberg, 2010).

[35] H. P. Breuer and F. Petruccione, *The theory of open quantum systems* (OUP Oxford, 2007).

[36] T. Hahn, D. Groll, T. Kuhn, and D. Wigger, Phys. Rev. B **100**, 024306 (2019).

[37] J. R. Johansson, P. D. Nation, and F. Nori, Comput. Phys. Commun. **184**, 1234 (2013).

Chapter 6
Conclusion

In this chapter, I provide a comprehensive discussion, summarize the research findings, and provide a general conclusion of the findings for the objectives of this doctoral thesis.

6.1 Comprehensive discussion

In this study, we experimentally measured the quantum path interference of an electron–phonon composite system in GaAs as a test material. We established through several theoretical studies that the experimentally observed phenomena can be analyzed using a quantum mechanical model, and we experimentally determined the coherence retention time (i.e., the decoherence time) of the electronic states during interband excitations. The electronic decoherence time was found to be approximately 12.9 fs at 290 K, while at a lower temperature of 10 K, it extended to approximately 27.8 fs. The observed decoherence phenomenon can be understood as a dephasing result of dissipative processes occurring within the electronic excited state, especially within the conduction band. In this context, our assumption revolves around the identification of the dissipative phenomenon as electron scattering. We evaluated the electronic decoherence time by considering the electron density within the conduction band and the photoinduced electron group velocities. Consequently, we established that the temperature-dependent behavior of the electronic decoherence time is primarily due to electron-electron scattering. However, the estimated electronic decoherence times in the low-temperature region of

10 - 90 K deviated slightly from the experimental values.

The two main points of discussion are;

I. Is electron-electron scattering the most influential factor contributing to electronic decoherence among the possible types of electron scattering ?

II. What is the reason for the gradual discrepancy between experimental and theoretical times in the low-temperature range of 10 - 90 K when there is a pronounced agreement between experimental and theoretical data in the broader range of 90 - 290 K ?

I. Electron scattering time with phonon and impurity

There are several types of electron scattering, and the representative types are electron-electron, electron-phonon, and electron-impurity scattering. The scattering probability is often determined by Matthiessen's law, which is determined by the respective scattering probability distributions. Matthiessen's law is that the sum of the scattering rates of the individual mechanisms determines the overall scattering probability. The electronic decoherence time used in this study also follows Matthiessen's law;

$$\tau^{-1} = \tau_0^{-1} + v(T)\,(n_d(T) + n_e(T))^{1/3}, \tag{6.1}$$

According to Matthiessen's law, τ_0 includes various scattering contributions, including electron-phonon, electron-hole, and electron-impurity interactions, while excluding electron-electron scattering;

$$\frac{1}{\tau_0} = \frac{1}{\tau_{\mathrm{e-ph}}} + \frac{1}{\tau_{\mathrm{e-h}}} + \frac{1}{\tau_{\mathrm{e-im}}} + \cdots . \tag{6.2}$$

In addition, we observed electronic coherence via coherent phonons gen-

erated by electron–phonon interaction in n-GaAs. Therefore, it is mainly the electron-phonon and electron-impurity scattering that are essential in Eq. (6.2).

I will review the electron scattering times due to electron-phonon and electron-impurity interactions.

A) Electron–phonon scattering

In polar semiconductors such as GaAs, the electron-phonon interaction includes the deformation potential interaction and the Fröhlich interaction [1, 2]. Polar LO phonon scattering via the Fröhlich interaction is more influential than scattering via the deformation potential interaction. Therefore, the electron–phonon scattering of GaAs is dominated by polar LO phonon scattering. The electron LO-phonon scattering time via the Fröhlich interaction in the Γ valley of GaAs is approximately 125 fs by a simple calculation [2, 3].

There are also theoretical studies of electron-to-one-phonon or two-phonon scattering in GaAs [4–6]. These studies have reported the scattering rate (inverse of the scattering time) of electron-phonon scattering at 300 K as a function of electron energy using ab initio calculations and other methods.

We used the AMSET [6] in the Python package to calculate the electron-phonon scattering time via deformation potential (in acoustic phonon) and polar interaction (in optical phonon). AMSET calculates scattering rates within the Born approximation using general material parameters. The differential scattering rate from state $|n\mathbf{k}\rangle$ to state $|m\mathbf{k}+\mathbf{q}\rangle$ is calculated using Fermi's golden rule [6].

Figure 6.1(a)-(b) show the temperature dependence of the estimated electron-phonon scattering time in GaAs. We calculate the electron en-

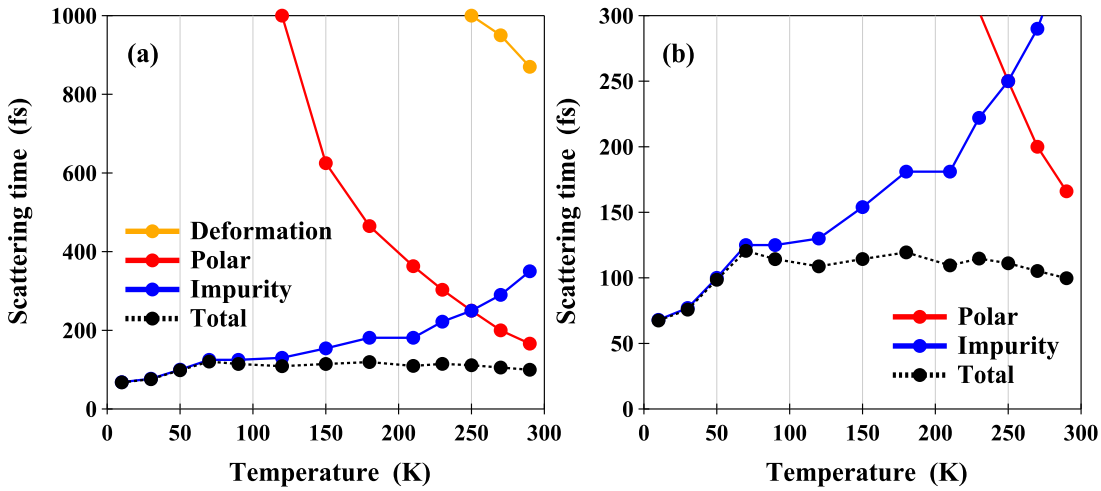

Figure 6.1: Estimated electron scattering time as a function of temperature by calculating AMSET. The used dopant concentration is approximately $\sim 3 \times 10^{17}$ cm^{-3}. The yellow line represents acoustic deformation potential scattering, the red line represents polar optical phonon scattering, and the blue line represents ionized impurity scattering. The black line represents the total scattering time for each scattering time according to Matthiessen's law; $\frac{1}{\tau_{\mathrm{total}}} = \sum \frac{1}{\tau_i}$. Figure (b) is an expanded version of the vertical axis in Figure (a).

ergy dependence of the scattering time at each temperature using AMSET. We then plot the scattering time at differential energies between the optical pulse and the conduction band minimum (i.e., $\Delta E(T) = \hbar\Omega_0 - E_g(T)$) in Fig. 6.1.

In Fig. 6.1, the scattering of polar phonons is approximately 150 fs at 290 K, and the effect of scattering decreases as the temperature decreases. The explanation for these reasons can be described as follows [1]. The phonons have energies of only a few tens of meV. Therefore, most electrons do not have enough energy for phonon emission at lower temperatures. This makes the influence of the scattering of the phonon processes negligible at lower temperatures.

B) Electron–impurity scattering

There are two types of electron–impurity scattering: ionized impurity and neutral impurity scattering.

Figure 6.1(a)-(b) show the temperature dependence of the estimated electron–(ionized) impurity scattering time in GaAs. The impurity scattering time is approximately 400 fs at 290 K. In contrast, in the low-temperature region, the probability of impurity scattering increases, and the scattering time can be interpreted as approximately 65 fs. It depends on electron energy in terms of impurity scattering cross-sections [1, 7]. Consequently, ionized impurity scattering becomes dominant at low temperatures where the electron energy is small.

II. Momentum relaxation time of electron

A simplified overview of electron scattering by phonons and impurities is described in the section above. In general, the electron scattering time, which is referred to in the field of electron scattering, corresponds to the momentum relaxation time (or momentum scattering time). There is also energy relaxation as a relaxation phenomenon, although the energy relaxation time is much longer than the momentum relaxation time. It is conceivable to infer that τ_0 in Eq. (6.2) is likely to coincide with the average momentum relaxation time of the electron.

The momentum relaxation time encapsulates the cumulative effects of all electron scattering processes, including interactions with other particles such as holes and phonons and scattering due to spatial disorder involving impurities and defects [1, 8, 9]. Furthermore, it is argued that electron-electron scattering, exemplified by electron-electron collisions, does not directly contribute to the electron momentum scattering time under an

isotropic parabolic conduction band that does not incorporate umklapp scattering [8–10]. These arguments are valid because the photoexcitation energies in this study are near the band edge of the conduction band.

The averaged momentum scattering time depends on the dynamic and static conditions of the phenomenon [8]. In the static (i.e., equilibrium) condition, the average electronic relaxation properties can be evaluated by drift and Hall mobility measurements [11]. In contrast, the average relaxation times in the dynamic limit, which are of interest in this discussion, have been studied using ultrafast coherent spectroscopy.

Several research groups have detailed the (dynamic) momentum relaxation times of electrons in n-GaAs [8, 12]. Notable among them are F. Vallée, F. Ganikhano, and F. Boganin, who delineated the temperature dependence of momentum relaxation times in n-GaAs using the infrared time-resolved coherent anti-Stokes Raman scattering (CARS) technique [8]. They compared the momentum relaxation times obtained by coherent spectroscopy and Hall effect measurements and reported that the dynamical relaxation times were shorter than those obtained from Hall effect measurements. Their experimental dopant concentration in n-GaAs is approximately $4.5 \times 10^{16}\ \mathrm{cm}^{-3}$, a level lower than the concentration used in the present study. Hase et al. reported electron relaxation times using n-GaAs with donor concentrations ranging from 10^{17} to $10^{18}\ \mathrm{cm}^{-3}$ [12]. These reported relaxation times are interpreted as not being significantly different for either in the electron density regime (due to dopants and photoexcitation) that we are currently investigating.

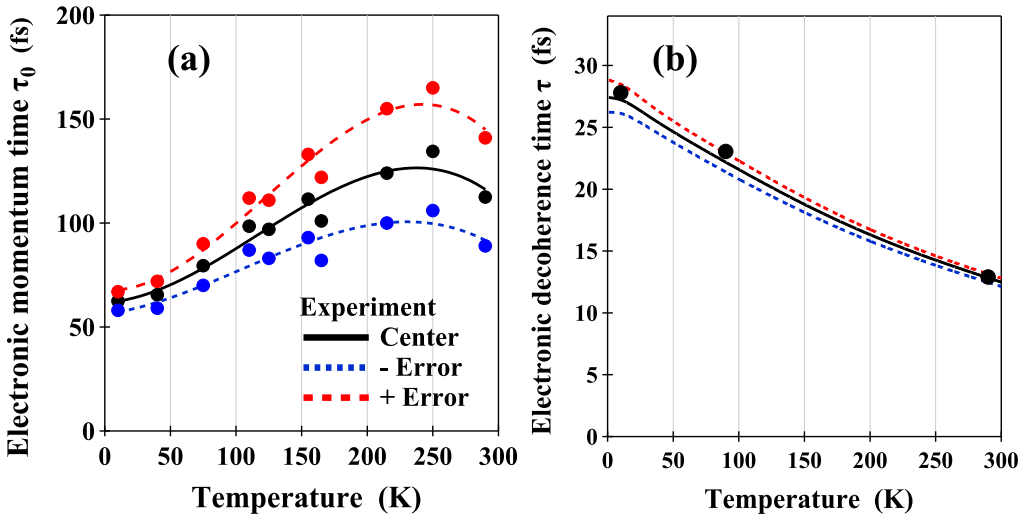

Figure 6.2: Electronic decoherence time as a function of temperature while considering the temperature dependence of τ_0. (a): Temperature dependence of dynamic electron momentum relaxation times adapted from Ref. [8]. We extracted the values and constructed a graphical representation. Red, blue, and black dots are the positive error, negative error, and median values, respectively. The red and blue dotted lines, and black lines are curve-fitted using polynomial functions (degree is 3). (b): Temperature dependence of the calculated electronic decoherence times. Black dot is the experimental result obtained by analyzing quantum interference shapes. The red, blue, and black lines are estimated electronic decoherence times using the positive error, negative error, and median value of electronic momentum time (τ_0), respectively.

III. Electronic decoherence time with momentum relaxation time of electrons

We incorporated the temperature dependence of the momentum relaxation time as τ_0 parameter into a theoretical model of the electronic decoherence time in Eq. (6.1).

Figure 6.2(a) shows the temperature dependence of the (dynamic) electron momentum time in n-GaAs, as reported by Vallée et al. [8]. In this case, we extracted three sets of values, including positive and negative error ranges and the median, from Ref. [8] and then constructed a graphical representation. We then performed a curve fitting procedure using a polynomial function, which yielded the function $\tau_0(T)$. In Fig. 6.2(a), the electron momentum time is almost constant (about 100 fs) in the temper-

ature range of 100 - 300 K. In addition, as the temperature approaches 10 K, the electron momentum time decreases to approximately 70 fs. These trends are very similar to the estimated average electron scattering time by phonon and impurity scattering, as shown in Fig. 6.1. The temperature dependence of τ_0 in Fig. 6.2(a) can be interpreted as the electron scattering is dominated by the interaction with impurities and defects in the low-temperature region. In contrast, the influence of electron-phonon scattering (mainly via Fröhlich interaction) intensifies with increasing temperature [8].

Figure 6.2(b) shows the estimated electronic decoherence time as a function of temperature, considering the temperature dependence of τ_0. The estimated decoherence times, as derived from the electron scattering model in Eq. (6.1), show remarkable agreement over a range of temperatures, including 10, 90, and 290 K, compared with the decoherence times obtained in the present experimental outcome. Thus, it is clear that electron-electron scattering is the dominant factor influencing decoherence in the temperature range of 90 - 290 K. However, in the low-temperature region, the effect of electron-electron scattering is diminished, emphasizing that the electronic decoherence time is influenced by electron scattering within τ_0.

These discussions show that electron scattering other than electron-electron scattering has a temperature dependence, but the electron momentum scattering time is considered to be about 70 fs at its most influential temperature of 10 K. In comparison, the electronic decoherence time is 28 fs at 10 K, indicating that electron-electron scattering has more influence than any other electron scattering in the present study.

6.2 Summary of the research findings

This doctoral thesis focuses on the ultrafast dynamics of quantum coherence in an electron–phonon composite system of GaAs as a test material and aims to reveal electronic decoherence times and decoherence phenomena.

The findings of this study are described as follows.

I. The quantitative evaluation method for the electronic decoherence time relevant to the distinctive quantum interference pattern obtained in n-GaAs by the attosecond-precision relative phase-locked double-pulse excitation method was conceived.
II. The electronic decoherence times were quantitatively determined as 27.8, 23.0, and 12.9 fs at 10, 90, and 290 K, respectively. The decoherence phenomena can be explained by the electron scattering involving interactions between photoexcited electrons and their environment within the conduction band. In addition, electron–electron scattering is identified as a major decoherence factor.

In addition, incidental results were achieved in this study.

1. A novel theoretical framework was developed for coherent control of electron-phonon composite systems using relatively phase-locked and polarization-controlled double-pulse excitation. The influence of the electronic decoherence time and the polarization of the double pulse on the experimentally observable quantum interference is clarified.
2. A comprehensive non-perturbative model was introduced to advance beyond second-order perturbation calculations. Theoretically, the generation of coherent phonons and quantum-path interference re-

main almost unaffected by arbitrary initial states because of the weak electron-phonon coupling in solid-state materials.

3. A saturation phenomenon in coherent phonons at relatively low pulse intensity was explained theoretically. This observation strengthens the contention that the Raman-like quantum path is the dominant quantum pathway observed in GaAs. Furthermore, the electronic decoherence is represented by using the dissipator induced by the excited states, which agrees with the factors identified in these experimental quantum-path interferometry.

6.3 General conclusion

From the above research findings, the conclusion of this thesis is as follows:

In this thesis, we explored quantum coherence within an electron-phonon composite system in solid-state materials. We embarked on an investigation aimed at understanding electronic coherence and its intricate relation with decoherence, an ultrafast phenomenon that disappears within a few tens of femtoseconds. The crux of this endeavor revolved around the central challenge of determining the duration of electronic coherence. We developed a novel approach to quantify the electronic decoherence time in n-GaAs as a test sample, a semiconductor material. Our investigation yielded quantitative results for electronic decoherence times 27.8 fs at 10 K to 12.9 fs at 290 K. The observed decoherence phenomena were attributed to electron scattering between photoexcited electrons and their environment within the conduction band. In addition, electron–electron scattering is identified as a major decoherence factor.

The attosecond precision relative phase-locked double femtosecond pulse excitation technique revealed distinct quantum interference patterns,

facilitating the elucidation of the intricate nature of the electron-phonon composite system. Our results provide invaluable insights into this field, enabling a discussion and understanding of quantum interference, electronic decoherence times, and the underlying interactions.

References

[1] P. Y. Yu and M. Cardona, *Fundamentals of semiconductors: physics and materials properties*, 3rd ed. (Springer Berlin, 2001).

[2] J. Shah, *Ultrafast spectroscopy of semiconductors and semiconductor nanostructures*, Springer Series in Solid-State Sciences (Springer Berlin Heidelberg, 2013).

[3] B. K. Ridley, *Quantum processes in semiconductors*, 3rd ed (Oxford University Press, New York, United Kingdom, 1993).

[4] J.-J. Zhou and M. Bernardi, Phys. Rev. B **94**, 201201 (2016).

[5] N.-E. Lee, J.-J. Zhou, H.-Y. Chen, and M. Bernardi, Nat. Commun. **11**, 1607 (2020).

[6] A. M. Ganose, J. Park, A. Faghaninia, R. Woods-Robinson, K. A. Persson, and A. Jain, Nat. Commun. **12**, 2222 (2021).

[7] V. Gantmakher and I. Levinson, *Carrier scattering in metals and semiconductors*, Modern Problems in Condensed Matter Sciences (Elsevier Science, 1987).

[8] F. Vallée, F. Ganikhanov, and F. Bogani, Phys. Rev. B **56**, 13141 (1997).

[9] K. Seeger, *Semiconductor physics : an introduction*, 9th ed, Advanced texts in physics ; (Springer, Berlin, Germany, 2004).

[10] B. A. Sanborn, Phys. Rev. B **51**, 14256 (1995).

[11] G. E. Stillman, C. M. Wolfe, and J. O. Dimmock, J. Phys. Chem. Solids **31**, 1199 (1970).

[12] M. Hase, S.-i. Nakashima, K. Mizoguchi, H. Harima, and K. Sakai, Phys. Rev. B **60**, 16526 (1999).